

PROCEEDINGS

OF 6TH INTERNATIONAL CONFERENCE ON
COMMUNICATIONS, ELECTROMAGNETICS AND MEDICAL
APPLICATIONS (CEMA'11)

Organized by:



FACULTY OF TELECOMMUNICATIONS
TECHNICAL UNIVERSITY OF SOFIA, BULGARIA



NATIONAL TECHNICAL UNIVERSITY OF ATHENS, GREECE,
SCHOOL OF ELECTRICAL AND COMPUTER ENGINEERING

NATIONAL TECHNICAL
UNIVERSITY OF ATHENS,
GREECE



SCHOOL OF ELECTRICAL
AND COMPUTER
ENGINEERING

Sofia, Bulgaria
6th - 8th October, 2011

KING

Edited by Prof. Dr. Eng. **Dimiter Tz. Dimitrov**

All rights reserved. This book, or parts there of, may not be reproduced in any form or by any means, electronic or mechanical, including photocopying or any information storage and the retrieval system now known or to be invented without written permission from the Publisher.

ISSN: 1314-2100

Printed in Bulgaria
KING 2001, Sofia



D. Dimitrov

Dear Colleagues,

It's my privilege to thank you all for your contributions submitted at 6th regular International Conference on 'Communication, Electromagnetic and Medical Applications' CEMA'11. This is one conference which should help future collaboration between engineering, especially communication technologies and medicine. This is an important scientific event not only in Balkan region, but in Europe, also. The International Conference on Communication, Electromagnetism and Medical Application CEMA'11 is dedicated to all essential aspects of the development of global information and communication technologies and their impact for medicine. The objective of Conference is to bring together lecturers, researchers and practitioners from different countries, working on the field of communication, electromagnetism and medical applications, computer simulation of electromagnetic field, in order to exchange information and bring new contribution to this important field of engineering design and application in medicine. The Conference will bring you the latest ideas and development of the tools for the above mentioned scientific areas directly from their inventors. The objective of the Conference is also to bring together the academic community, researchers and practitioners working in the field of Communication, Electromagnetic and Medical Applications, not only from all over Europe, but also from America and Asia, in order to exchange information and present new scientific and technical contributions. Many well known scientists took part in conference preparation as members of International Scientific Committee or/and as reviewers of submitted paper. I would like to thank you all for their efforts, for their suggestions and advices.

On behalf of the International Scientific Committee, I would like to wish you successful presentations of your papers, successful discussions and new collaborations for your future scientific investigations. Engineering and medicine should provide high level of live for all people.

Dimiter Tz. Dimitrov
Conference Chairman

INTERNATIONAL SCIENTIFIC COMMITTEE

Honorary Chairman:

Prof. N. UZUNOGLU, National Technical University of Athens, Greece

Chairman:

D. TZ. DIMITROV, Technical University of Sofia, Bulgaria

Vice Chairmen:

P. FRANGOS, National Technical University of Athens, Greece

Members:

N. AMPILOVA,	University of Perersburg, Russia
A. BEKJARSKY,	Technical University of Sofia, Bulgaria
B. DEKERIS,	Kaunas University of Technology, Litvania
V. DEMIREV,	Technical University of Sofia, Bulgaria
N. DIB,	Jordan University of Science and Technology, Jordan
M. DONTSCHEWA,	University of Applied Sciences, Dornbirn, Austria
V. DUMBRAVA,	Kaunas University of Technology, Litvania
D. EIDUKAS,	Kaunas University of Technology, Litvania
E. GAGO-RIBAS,	University of Oviedo, Spain
N. ESCUDEIRO,	Instituto Superior Técnico, Porto, Portugal
G. GOUSSETIS,	Heriot - Watt University, United Kingdom
A. GRIGORIEV,	St. Petersburg University, Russia.
S. GUERGOV,	Technical University of Sofia, Bulgaria
S. Ver HOEYE,	University of Oviedo, Spain
M. HOFMANN,	University of Ulm, Germany
V. HRISTOV,	University of Blagoevgrad, Bulgaria
I. ILIEV,	Technical University of Sofia, Bulgaria
L. JORDANOVA,	Technical University of Sofia, Bulgaria
R. KRIVICKAS,	Kaunas University of Technology, Litvania
A. LAZAROV,	Bourgas Free University, Bulgaria
G. MALLET,	University "Sophia Antipolis", Nice, France
G. MATSOPOULOS,	National Technical University of Athens, Greece
M. MARINKEV,	Medical University of Plovdiv, Bulgaria
M. MARTINS,	Instituto Superior Técnico, Lisboa, Portugal
M. MORALES-GONZALES,	University of Valladolid, Spain
K. NIKITA,	National Technical University of Athens, Greece
M. NIKOLOVA,	High Naval School, Varna, Bulgaria
J. PETROVSKA,	Medical University of Sofia, Bulgaria
F. PRATO,	University of Western Ontario, Canada
H. ROTH,	University of Siegen, Germany
S. SAUTBEKOV,	Euroasian University, Astana, Kazakhstan
A. SAVOV,	Medical University of Sofia, Bulgaria
S. SAVOV,	Technical University of Varna, Bulgaria
H-P. SCHADE,	Technical University of Ilmenau, Germany
L. SONG,	Technical University of Harbin, China
L. SVILAINIS,	Kaunas University of Technology, Lithuania
A. USHEVA,	University of Boston, USA

REVIEWERS

Q. BALZANO,	University of Maryland, USA
H. BERG,	Technical University of Jena, Germany
E. BOEMO,	Technical University of Madrid, Spain
M. DONTSCHEWA,	University of Applied Sciences, Dornbirn, Austria
D. DIMITROV,	Technical University of Sofia, Bulgaria
M. HOFMANN,	University of Ulm, Germany
F. KLETT,	Franhofer Institute, Ilmenau, Germany
G. MALLET,	University "Sophia Antipolis", Nice, France
M. MARINKEV,	Medical University of Plovdiv, Bulgaria
M. MARTINS,	Instituto Superior Técnico, Lisboa, Portugal
M. MORALES-GONZALES,	University of Valladolid, Spain
J. PETROVSKA,	Medical University of Sofia, Bulgaria
H. ROTH,	University of Siegen, Germany
A. SAVOV,	Medical University of Sofia, Bulgaria
H-P. SCHADE,	Technical University of Ilmenau, Germany
L. SONG,	Technical University of Harbin, China
A. USHEVA,	University of Boston, USA
S. Ver HOEYE,	University of Oviedo, Spain

Sponsors: GLOBUL, INTRACOM

REGISTRATION

October, 06th, 09h – 16h

Conference registration desk:

International Meeting Centre of Technical University – Sofia

CONFERENCE PROGRAM

International Meeting Centre of Technical University-Sofia

06th October, 2011

Opening ceremony

09h - 09h30

INVITED LECTURE

09h30- 10h15

George Mitrin, GLOBUL, Bulgaria, Electromagnetic Field Exposure and Mobile Telephony

Coffe-break

10h15-10h45

SCIENTIFIC PROGRAM

FIRST SESSION

10h45 -12h

Chairman: Prof. V. Demirev, Technical University of Sofia, Bulgaria

1. *E. Kallitsis, A. Karakasiliotis and P. Frangos, National Technical University of Athens, Greece, **Combination of range profile alignment technique with autofocusing post - processing algorithm for ISAR image optimization***
2. *Seil Sautbekov*, Gulnar Alkina* and Panayiotis Frangos**, *Eurasian National University, Astana, Kazakshtan, **National Technical University of Athens, Greece, **Unsymmetrical Electromagnetic Wave Diffraction by a Long Pipe***
3. *Maria P. Barbarosou* and Nicholas G. Maratos**, *Hellenic Air-Force Academy, Department of Aeronautical Sciences, Division of Electronics and Communication Engineering Dekelia Air Force Base, Greece, **National Technical University of Athens, School of Electrical and Computer Engineering, Athens, Greece, **A Nonfeasible Quadratic Approximation Recurrent Neural Network for Equality Constrained Optimization Problems***
4. *Veselin Demirev, Radio Communications and Video Technologies Department, TU-Sofia, **SCP Rake Receiver - The Possible Solution of N-LOS HAPS and WIMAX mm-Wave Networks***
5. *Veselin Demirev, Radio Communications and Video Technologies Department, TU-Sofia, **A New Approach for PN-codes Generation and Synchronization in CW Mobile Multistatic Radar Systems***

Lunch

12h-13h

SECOND SESSION

13h -14h30

Chairman: Prof. P. Frangos, National Technical University of Athens, Greece

1. *Atanas D. Dimitrov*, Faculty of Telecommunication, Technical University of Sofia, Bulgaria, **Algorithms for management and control of system for therapy by "random" running low frequency magnetic field**
2. *Atanas D. Dimitrov*, Faculty of Telecommunication, Technical University of Sofia, Bulgaria, **Method for design of system for therapy using "random" running low frequency magnetic field**
3. *Antoniya Petrova Petrova*, Faculty of Telecommunication, Technical University of Sofia, Bulgaria, **Influence and image of the microwave electromagnetic field in the living tissues in the human body**
4. *Antoniya Petrova Petrova*, Faculty of Telecommunication, Technical University of Sofia, Bulgaria, **Influence and image of the UHF electromagnetic field in the living tissues in the human body**
5. *Mihail Plamenov Tonev*, Faculty of Telecommunication, Technical University of Sofia, Bulgaria, **Low phase noise Ku band push - push oscillator**
6. *Dimitar Tz. Dimitrov, Sasho Guergov*, Technical University of Sofia, Bulgaria, **System for Simultaneously Therapy by Running Low Frequency Magnetic Field and ac-upressure**

Coffe-break

14h30-15h

THIRD SESSION

15h-16h30h

Chairman: Prof. D. Dimitrov, Technical University of Sofia, Bulgaria

1. *Brunonas Dekeris, Lina Narbutaitė, Rasa Brūzgienė*, Department of Telecommunication, Kaunas University of Technology, Lithuania, **Channel Zapping Time Analysis of IPTV over WiMax Access Network**
2. *L. Svilainis, R. Jurkonis, D. Kybartas, A. Chaziachmetovas*, Kaunas University of Technology, Kaunas, Lithuania, **The investigation of filters for real-time data acquisition**
3. *Deyan M. Milev*, Faculty of Telecommunications, Technical University of Sofia, Bulgaria, **Design and Signal Processing of a ECG Recorder**
4. *Deyan M. Milev*, Faculty of Telecommunications, Technical University of Sofia, Bulgaria, **Portable Equipments for Remote Monitoring of Heart Activity in Telemedicine**

5. *Valentin Hristov**, *Boris Tudjarov***, *Department of Computer Systems and Technology at South West University – Blagoevgrad, Bulgaria, **Department of Design Fundamentals, Technical University – Sofia, Bulgaria, **Using Genetic Algorithm for Routing**
6. *Samuel Nowakowski*, *Nathalie Bernard-Issenmann*, PRES de l'Université de Lorraine, Nutice, France, *Hamed YAHOU*, Université Claude Bernard Lyon, France, **ELLEIEC project a comparative evaluation of teaching practices in Europa – recommendations and best practices**

07th October, 2011

FOUR SESSION

09h30-11h,

Chairman: Prof. V. Georgieva, Technical University of Sofia, Bulgaria

1. *Vladimir H. Kanchev*, *Ivo R. Draganov*, *Antoaneta A. Popova*, Radiocommunications and Videotechnologies Department, Technical University – Sofia, Bulgaria, **Segmentation of Neuro MR Images through Semi-Supervised Learning**
2. *Dobri Dobrev*, *Lidia Jordanova*, Faculty of Telecommunications, Technical University of Sofia, Bulgaria, **Algorithm for Coaxial Part's Design of Cable Multimedia Network**
3. *Lidia Jordanova*, *Dobri Dobrev*, *Tsveta Dimitrova*, Faculty of Telecommunications, Technical University of Sofia, Bulgaria, **Broadcast Signal Processing in the Headend of a Cable Multimedia System**
4. *Veska M. Georgieva*, *Agata H. Manolova*, Faculty of Telecommunications, Technical University of Sofia, Bulgaria, **Edge Detection in Sequences of CT Images**
5. *N. B. Ampilova*, *I. P. Soloviev*, Comp. Sci. Dept, Math. & Mech. Faculty, St. Petersburg State University St. Petersburg, Russia, *E. Y. Gurevich*, Sofia & Jacobs Foundation, St. Petersburg, Russia, **Application of Modified Fractal Signature & Regny Spectrum Methods to the Analysis of Biomedical Preparations Images**
6. *Alexander Bekiarski*, *Snejana Pleshkova-Bekiarska*, *Svetlin Antonov*, Technical University – Sofia, Bulgaria, **Real Time Processing and Database of Medical Thermal Images**

CLOSING SESSION

11h-11h30

Lunch

11h30-12h30

SOCIAL PROGRAM

Banquet

October, 06th, 19h30

Trip

to Plovdiv - old town

October 08th

CONTACT US:

GENERAL INFORMATION AND SUBMISSION OF CONTRIBUTIONS

Prof. Dr. D. Dimitrov

Faculty of Telecommunications

Technical University of Sofia

8, Kliment Ohridsky str.

1756 Sofia, Bulgaria

Phone/Fax: ++359 2 9652278

E-mail: dcd@tu-sofia.bg

Prof. Dr. P. Frangos

National Technical University of Athens

School of Electrical and Computer Engineering

9, Iroon Polytechniou Str.,

157 73 Zografou, Athens, Greece

Phone: 00 30 210 772 3694

Fax: 00 30 210 772 2281

E-mail: pfrangos@central.ntua.gr

TABLE OF CONTENTS

COMBINATION OF RANGE PROFILE ALIGNMENT TECHNIQUE WITH AUTOFOCUSING POST - PROCESSING ALGORITHM FOR ISAR IMAGE OPTIMIZATION	1
<i>E. Kallitsis, A. Karakasiliotis, P. Frangos</i>	
UNSYMMETRICAL ELECTROMAGNETIC WAVE DIFFRACTION BY A LONG PIPE	8
<i>Seil Sautbekov, Gulnar Alkina, Panayiotis Frangos</i>	
A NONFEASIBLE QUADRATIC APPROXIMATION RECURRENT NEURAL NETWORK FOR EQUALITY CONSTRAINED OPTIMIZATION PROBLEMS	13
<i>Maria P. Barbarosou, Nicholas G. Maratos</i>	
SCP RAKE RECEIVER - THE POSSIBLE SOLUTION OF N-LOS HAPS AND WIMAX MM-WAVE NETWORKS	18
<i>Veselin Demirev</i>	
A NEW APPROACH FOR PN-CODES GENERATION AND SYNCHRONIZATION IN CW MOBILE MULTISTATIC RADAR SYSTEMS	22
<i>Veselin Demirev</i>	
ALGORITHMS FOR MANAGEMENT AND CONTROL OF SYSTEM FOR THERAPY BY "RANDOM" RUNNING LOW FREQUENCY MAGNETIC FIELD	26
<i>Atanas D. Dimitrov</i>	
METHOD FOR DESIGN OF SYSTEM FOR THERAPY USING "RANDOM" RUNNING LOW FREQUENCY MAGNETIC FIELD	31
<i>Atanas D. Dimitrov</i>	
INFLUENCE AND IMAGE OF THE MICROWAVE ELECTROMAGNETIC FIELD IN THE LIVING TISSUES IN THE HUMAN BODY	35
<i>Antoniya Petrova Petrova</i>	
INFLUENCE AND IMAGE OF THE UHF ELECTROMAGNETIC FIELD IN THE LIVING TISSUES IN THE HUMAN BODY	39
<i>Antoniya Petrova Petrova</i>	
LOW PHASE NOISE KU BAND PUSH - PUSH OSCILLATOR	43
<i>Mihail Plamenov Tonev</i>	
SYSTEM FOR SIMULTANEOUSLY THERAPY BY RUNNING LOW FREQUENCY MAGNETIC FIELD AND ACUPRESSURE	48
<i>Dimiter Tz. Dimitrov, Sasho Guergov</i>	
CHANNEL ZAPPING TIME ANALYSIS OF IPTV OVER WIMAX ACCESS NETWORK	52
<i>Brunonas Dekeris, Lina Narbutaitė, Rasa Brūzgienė</i>	
THE INVESTIGATION OF FILTERS FOR REAL-TIME DATA ACQUISITION	57
<i>L. Svilainis, R. Jurkonis, D. Kybartas, A. Chaziachmetovas</i>	

DESIGN AND SIGNAL PROCESSING OF A ECG RECORDER	61
<i>Deyan M. Milev</i>	
PORTABLE EQUIPMENTS FOR REMOTE MONITORING OF HEART ACTIVITY IN TELEMEDICINE.....	65
<i>Deyan M. Milev</i>	
USING GENETIC ALGORITHM FOR ROUTING.....	70
<i>Valentin Hristov, Boris Tudjarov</i>	
ELLEIEC PROJECT A COMPARATIVE EVALUATION OF TEACHING PRACTICES IN EUROPA - RECOMMENDATIONS AND BEST PRACTICES.....	74
<i>Samuel Nowakowski, Nathalie Bernard-Issenmann</i>	
SEGMENTATION OF NEURO MR IMAGES THROUGH SEMI-SUPERVISED LEARNING.....	79
<i>Vladimir H. Kanchev, Ivo R. Draganov, Antoaneta A. Popova</i>	
ALGORITHM FOR COAXIAL PART'S DESIGN OF CABLE MULTIMEDIA NETWORK	84
<i>Dobri Dobrev, Lidia Jordanova</i>	
BROADCAST SIGNAL PROCESSING IN THE HEADEND OF A CABLE MULTIMEDIA SYSTEM	88
<i>Lidia Jordanova, Dobri Dobrev, Tsveta Dimitrova</i>	
EDGE DETECTION IN SEQUENCES OF CT IMAGES	92
<i>Veska M. Georgieva, Agata H. Manolova</i>	
APPLICATION OF MODIFIED FRACTAL SIGNATURE & REGNY SPECTRUM METHODS TO THE ANALYSIS OF BIOMEDICAL PREPARATIONS IMAGES	96
<i>N. B. Ampilova, I. P. Soloviev, E. Y. Gurevich</i>	
REAL TIME PROCESSING AND DATABASE OF MEDICAL THERMAL IMAGES	101
<i>Alexander Bekiarski, Snejana Pleshkova-Bekiarska, Svetlin Antonov</i>	

AUTHOR INDEX

ALKINA, G.	8	JORDANOVA, L.	84, 88
AMPILOVA, N.	96	JURKONIS, R.	57
ANTONOV, S.	101	KALLITSIS, E.	1
BARBAROSOU, M.	13	KANCHEV, V.	79
BEKIARSKI, A.	101	KARAKASILIOTIS, A.	1
BERNARD-ISSENMANN, N.	74	KYBARTAS, D.	57
BRŪZGIENĖ, R.	52	MANOLOVA, A.	92
CHAZIACHMETOVAS, A.	57	MARATOS, N.	13
DEKERIS, B.	52	MILEV, D.	61, 65
DEMIREV, V.	18, 22	NARBUTAITĖ, L.	52
DIMITROV, A.	26, 31	NOWAKOWSKI, S.	74
DIMITROV, D.	48	PETROVA, A.	35, 39
DIMITROVA, TS.	88	PLESHKOVA-BEKIARSKA, S.	101
DOBREV, D.	84, 88	POPOVA, A.	79
DRAGANOV, I.	79	SAUTBEKOV, S.	8
FRANGOS, P.	1, 8	SOLOVIEV, I.	96
GEORGIEVA, V.	92	SVILAINIS, L.	57
GUERGOV, S.	48	TONEV, M.	43
GUREVICH, E.	96	TUDJAROV, B.	70
HRISTOV, V.	70		

COMBINATION OF RANGE PROFILE ALIGNMENT TECHNIQUE WITH AUTOFOCUSING POST – PROCESSING ALGORITHM FOR ISAR IMAGE OPTIMIZATION

E. Kallitsis, A. Karakasiliotis and P. Frangos

National Technical University of Athens

9, Iroon Polytechniou Str., GR 157 73, Zografou, Athens, Greece

Tel: +30 210 772 3694, Fax: +30 210 772 2281, E-Mail: ekalorama@gmail.com, anastasiskarak@yahoo.gr, pfrangos@central.ntua.gr

Abstract

Autofocus is a technique for improving inverse synthetic aperture radar (ISAR) imaging.

In this paper, an autofocusing method is developed for high-resolution stepped-frequency ISAR. Non-uniform rotational motion is compensated through the proposed combination of a conventional coarse range alignment technique and a recently introduced post-processing methodology. In this way, the computational cost of polar reformatting process can be circumvented. The proposed CPI-split autofocusing process results in well focused ISAR images for high angular acceleration periods. Emphasis is placed on further reduction of the computational cost and the storage requirements by applying this post-processing methodology on the range profile history data.

Furthermore, ISAR images entropy dependencies are examined through various simulation results, leading to an acceptable range of entropy values for the autofocusing process.

1. Introduction

Inverse synthetic aperture radar (ISAR) is a kind of a microwave imaging system that exploits signal processing techniques to provide 2-D imaging results for a non-cooperative moving target and can be used for both military and civilian purposes. High bandwidth pulses are transmitted, target echoes at different aspect angles are received and are processed coherently to form the target image. One of the fundamental steps of the ISAR technique is the image focusing or motion compensation [1-8].

In real-world ISAR imaging scenarios, the target being imaged is often engaged in complicated maneuvers and the motion of the target can be divided into translational and rotational motion. The rotational motion contributes to imaging, whereas the translational motion introduces unwanted phase distortion, which is dependent on the target motion parameters [2, 3]. Uniform rotation is necessary to

attain efficient cross-range resolution, while non-uniform rotation may significantly degrade the acquired ISAR image quality. Polar reformatting [1] is a multi-step interpolation process to compensate for rotational motion impairment, with considerable computational complexity. It is based on rotational motion parameters, which are unknown for non-cooperative radar targets.

In the context of this paper, a range profile alignment technique is combined with an autofocusing post-processing algorithm for ISAR image optimization. Scatterers' migration through resolution cells (MTRC) due to non-uniform rotation [1] can be corrected by the proposed methodology, and ISAR image quality can be improved before further target classification or identification procedures are applied.

Usually, autofocusing is based upon an image entropy minimization criterion [3, 5], which is also adopted in the present study. Alternatively, autofocusing can be achieved via image contrast maximization [6]. In this paper, a conventional coarse range alignment technique, which is based on cross-correlation, is first applied on raw radar data. Following the rotational range migration (RRM) correction, the recently proposed CPI-split autofocusing method [9] is initiated on aligned range profile history data. Small, rapidly maneuvering air targets are the typical ISAR imaging scenario we examine.

Based on an acceptable range of image entropy values, the proposed autofocusing algorithm neglects range profiles leading to poor quality ISAR images. Numerical results validate the image focusing capability of the proposed method. In order to quantify the ISAR image entropy variation with respect to signal-to-noise ratio, aspect angle and target angular acceleration, a thorough statistical

analysis is performed based on various Monte-Carlo trials.

In Section 2, we briefly describe the basic points of the proposed autofocusing method, and in Section 3 we present simulation results for a typical ISAR imaging scenario of a fighter aircraft. Finally, useful conclusions are drawn for future research on ISAR image autofocus.

2. Proposed autofocusing algorithm

The conventional range-Doppler technique [1, 2] for ISAR image generation is adopted in the present study. In case of uniform target rotation, polar reformatting process [1] is usually employed to counteract the distortion induced by target rotation (range and cross-range migration) [10]. This process can also be applied to compensate non-uniform rotational motion, but it requires the knowledge of specific kinematic parameters of the target (iterative search for angular velocity and acceleration) and computationally intensive interpolation procedures.

In our study, we assume that the target size does not exceed the practical limit of blur radius [1]. Thus, polar reformatting can be avoided for the case of uniform rotation. In case of non-uniform target rotation (constant angular acceleration), we propose a novel, heuristic autofocusing algorithm to compensate for the ISAR image blurring. The entropy H of the power normalized ISAR image is calculated [8], and, if it exceeds a certain threshold H_{thr} , a post-processing methodology is followed to substitute the received signal part that is affected by the target angular acceleration. Range tracking is also performed through cross-correlation of range profiles with a reference average range profile for the first CPI of the examined ISAR data. Due to RRM restriction in relative aspect angle difference between two range profiles ($\Delta\theta_{RRM} = \frac{\Delta r_s}{T_D}$, where Δr_s is the range resolution and T_D is the target extent) [11], we select to group range profiles (CPI partition) and compute an average range profile for each CPI part, which is cross-correlated with the reference one to derive the required alignment as an integer number of range cells.

The diagram of Fig. 1 depicts the post-processing methodology of the proposed CPI-split autofocusing method [9]. It is based on the partition and the con-

catenation of the range profile data matrices of two consecutive CPIs.

Naming the CPI during which accelerated rotational motion is exhibited as “unfocused CPI”, two different range profile data segments are formed. Concatenated parts of the unfocused CPI and the CPI preceding it (“previous CPI” in Fig. 1) form “segment 1”. Similarly, “segment 2” is formed by concatenating parts of the unfocused CPI and the CPI following it (“next CPI” in Fig. 1).

The CPI-split autofocusing method consists of a variable number of stages (N_{stages}), associated with the split depth as a fraction of CPI. In view of hardware implementation cost reduction, the CPI divisor is chosen to be a power-of-two number, increasing by a factor of two from stage to stage. By applying the proposed method on the range profile data, we save the first Fourier transform in conventional range-Doppler imaging and the computational complexity is significantly reduced.

In Fig. 1, the partition and concatenation methodology of the 3rd stage ($\frac{CPI}{8}$) of CPI-split algorithm is graphically depicted. The main concept is the same for all stages of the algorithm ($\frac{CPI}{2}$, $\frac{CPI}{4}$, etc.). The vertical axis of Fig. 1 includes the burst index and the horizontal axis includes the range cell index. Blue and red, numbered ellipsoids indicate respectively the possible data combinations of segment 1 and segment 2. The term combination refers to the concatenation of data parts of two consecutive CPIs. In general, the two data parts to be combined have different sizes in terms of number of bursts, with the exception of $\frac{CPI}{2}$ -stage. Dashed ellipsoids denote those data combinations that are already examined in previous CPI-split stages, which are excluded for an efficient algorithm implementation. The number of possible combinations per segment for the i -th CPI-split stage is

$$N_{i, comb} = 2^{i-1} \quad (i = 1, \dots, N_{stages}) \quad (1)$$

In our simulations, we set N_{stages} to 4, resulting in a total number of 30 examined data combinations. For each data combination, an ISAR image is formed through two-dimensional Fourier transform and its respective entropy value is computed [8]. At each CPI-split stage, we can either pick the ISAR image with the minimum entropy value or the first ISAR image resulting in an entropy value within an

acceptable range. By setting an appropriate range of acceptable entropy values, the algorithm can be stopped at an early CPI-split stage, saving computational time while still satisfying ISAR image focus criteria.

In order to determine the appropriate values for the entropy threshold H_{thr} , as well as the lower (H_{low}) and upper (H_{upp}) bounds for the acceptable entropy range, we perform various Monte-Carlo simulations to quantify the entropy variation with respect to signal-to-noise ratio (SNR), aspect angle and angular acceleration.

In Fig. 2, the probability distribution function (PDF) of the image entropy is plotted for both uniform and non-uniform rotation, for SNR equal to 15dB. The angular sector examined is approximately 18.3° , corresponding to 10 CPIs. For the non-uniform rotation case, angular acceleration is set to 0.64 rad/sec^2 . These PDF graphs result from 100 Monte-Carlo trials. The first graph provides us with the acceptable entropy bounds, H_{low} and H_{upp} , while the second graph gives us the appropriate entropy threshold H_{thr} .

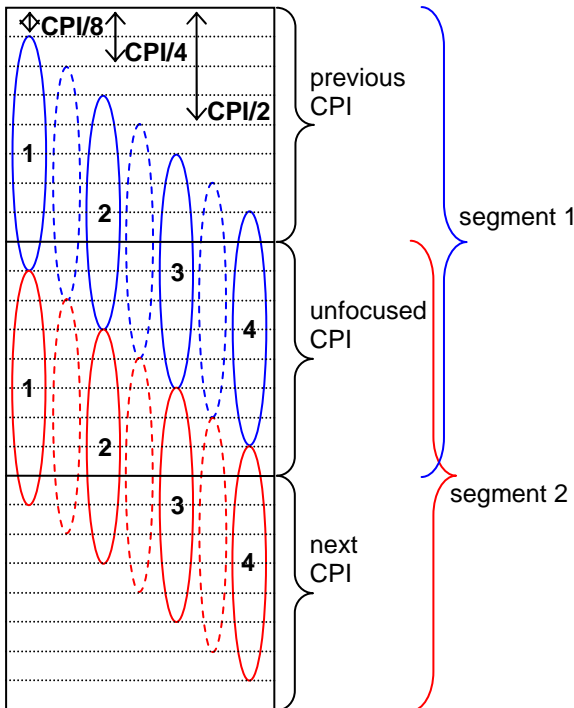


Fig. 1. Post-processing methodology of the proposed autofocus algorithm: $CPI/8$ - stage

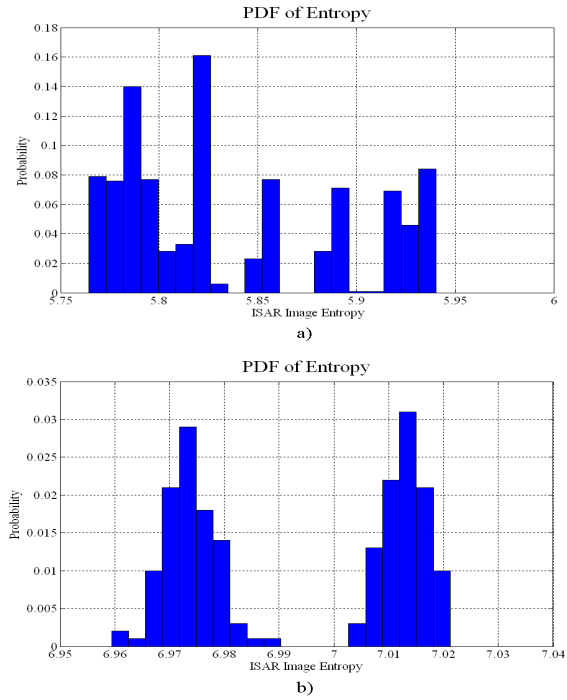


Fig. 2. Probability distribution functions of ISAR image entropy, for SNR=15dB: a – uniform rotation; b – non-uniform rotation

3. Numerical results

The simulated target geometry is shown in Fig. 3. It is a point scatterer model of a Mirage 2000C aircraft, consisting of 208 scatterers, with length of 14.5m and wingspan 9.0m. Radar and target motion parameters for our ISAR numerical simulations are included in Table 1.

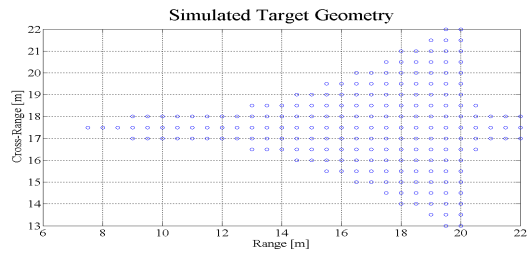


Fig. 3. Geometry of simulated Mirage 2000C target

Table 1. ISAR simulation parameters

Parameter	Value [units]
initial carrier frequency, f_0	10 [GHz]
range resolution, Δr_s	0.46875 [m]
cross-range resolution, Δr_c	0.47244 [m]
radar bandwidth, B	320 [MHz]
number of frequencies, M	64
frequency step, Δf	5 [MHz]
pulse repetition frequency, PRF	15 [KHz]
burst duration, T_b	4.266 [msec]
coherent processing interval, CPI	0.546 [sec]
number of bursts, N	128

number of CPIs, N_{CPI}	10
angular velocity, ω	0.0586 [rad/sec]
angular acceleration, γ	0.64 [rad/sec ²]

Backscattered radar data $x(m, n)$ are simulated through the following formula [3]

$$x(m, n) = \sum_{k=1}^d s_k \exp \left[-j \frac{4\pi}{c} f_m (x_k \cos \theta_n - y_k \sin \theta_n) \right] + u(m, n) \quad (2)$$

here d – the number of scatterers; s_k – the scattering intensity of k -th point scatterer; (x_k, y_k) – the Cartesian coordinates of k -th point scatterer, with respect to the radar position; m – the stepped frequency index ($m=1, \dots, M$); n – the burst index ($n=1, \dots, N \cdot N_{CPI}$) for a number of simulated CPIs (N_{CPI}); N – the number of bursts during one CPI; $u(m, n)$ – the two-dimensional additive white Gaussian noise component.

The aspect angle θ_n of the target at slow-time instant t_n is simulated as

$$\theta_n = \begin{cases} \theta_0 + \omega t_n + \frac{1}{2} \gamma (t_n - t_{start})^2, & \text{angular acceleration period(s)} \\ \theta_0 + \omega t_n, & \text{otherwise} \end{cases} \quad (3)$$

here θ_0 – the initial aspect angle of the target, assumed to be at a distance of 10 Km; ω – the angular velocity; γ – the angular acceleration; t_{start} – the time instant at which an angular acceleration period begins.

In our numerical simulations, N_{CPI} raw data matrices are formed through Eq. (2), assuming uniform rotation, except for particular angular acceleration periods (4th and 8th CPI). Angular acceleration is induced over the specific CPIs through Eq. (3), affecting the respective raw data (rapid angular maneuvers).

The simulated rotational motion profile is shown in Fig. 4, zoomed in the region of the 4th CPI, whose start and end time instants are noted by the blue vertical lines. Time is indexed in units of burst duration (slow-time). Angular variation between uniform and non-uniform rotation periods is smoothed by applying a moving average filter of size $\frac{N}{8}$. The same profile is also simulated for the 8th CPI.

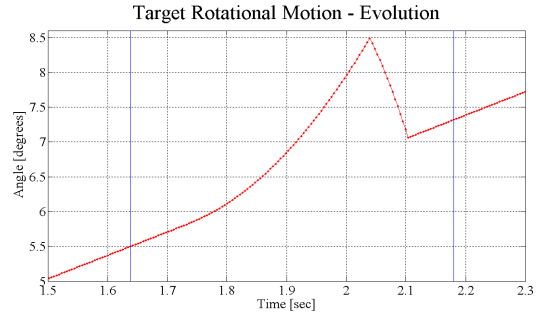


Fig. 4. Simulated rotational motion profile (4th CPI region)

In our simulation scenario, the ISAR images for 10 CPIs are reconstructed through range-Doppler technique, and the entropy values of the power normalized images are computed [8]. For each CPI with image entropy greater than a certain threshold ($H > H_{thr}$), the proposed CPI-split autofocus algorithm is employed, resulting in a focused image with the minimum entropy over a number of possible data combinations.

ISAR image entropy variation with respect to SNR and γ is characterized via 100 Monte-Carlo simulations, carried out for both uniform and non-uniform rotation. Numerical results for entropy variation are shown in Fig. 5. The angular sector scanned is approximately 18.3° , with θ_0 set to 0° . For uniform rotation (angular velocity as in Table 1), strong dependence on SNR is observed (for both mean value and standard deviation of image entropy), while the effect of CPI index variation is more obvious for high SNR levels. For non-uniform rotation, angular acceleration γ is varied in the range $[-0.64, 0.64]$ rad/sec², for SNR equal to 15dB and for two specific CPI indices (angular acceleration periods).

The lower and upper bounds for the acceptable entropy range (as a stop condition for the proposed autofocus methodology) can be determined by a statistical analysis of Monte-Carlo simulation results. For constant angular velocity, we define the ISAR image entropy function with respect to CPI index (n_{CPI}), SNR and γ , as $H(n_{CPI}, SNR, \gamma)$. The entropy bounds that guarantee ISAR image focus are calculated by

$$H_{low} = \min_{n_{CPI}} \left\{ \min_{SNR} \left\{ H(n_{CPI}, SNR, \gamma = 0) \right\} \right\} - 2 \cdot \overline{\sigma_H} \quad (4)$$

$$H_{upp} = \max_{n_{CPI}} \left\{ \max_{SNR} \left\{ H(n_{CPI}, SNR, \gamma = 0) \right\} \right\} + 2 \cdot \overline{\sigma_H} \quad (5)$$

here $\min_{n_{CPI}}\{x\}$ – the minimum value of x over CPI index; $\min_{SNR}\{x\}$ – the minimum value of x , over all Monte-Carlo trials, for a particular SNR; $\overline{\sigma_H}$ – the mean value of the standard deviation of image entropy, over CPI index, for $\gamma=0$; $2 \cdot \overline{\sigma_H}$ – the selected safety margin for the two entropy bounds.

The entropy threshold H_{thr} can be arbitrarily chosen in the range

$$H_{upp} < H_{thr} \leq \min_{n_{CPI}} \left\{ \min_{SNR} \left[H(n_{CPI}, SNR, \gamma) \right] \right\} - 2 \cdot \overline{\sigma_{H,\gamma}} \quad (6)$$

here $\overline{\sigma_{H,\gamma}}$ – the mean value of the standard deviation of image entropy, over CPI index, for the simulated value of γ .

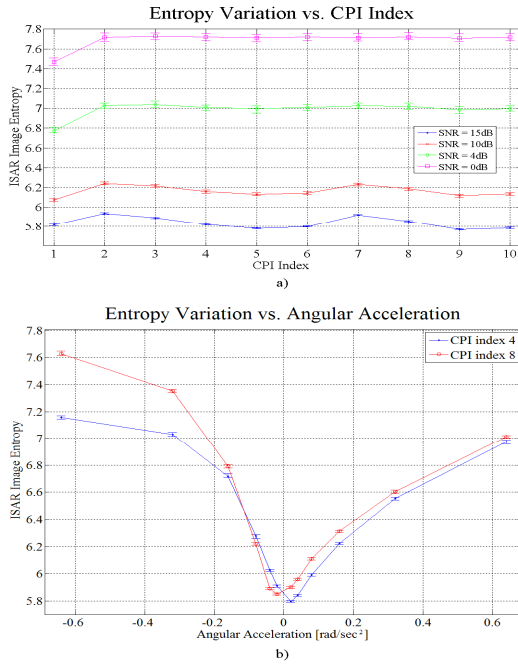


Fig. 5. ISAR image entropy: a – uniform rotation, variation over SNR and CPI index; b – non-uniform rotation, variation over γ , for specific CPIs and SNR=15dB

In Table 2, the selected values of entropy bounds and entropy threshold are cited.

Table 2. Selected entropy bounds and entropy threshold

Algorithm Parameter	Value
lower entropy bound, H_{low}	5.7586
upper entropy bound, H_{upp}	5.9460
entropy threshold, H_{thr}	6.0000

In Fig. 6(a) the average range profile for the 1st CPI is shown. It is used as the reference profile for the cross-correlation based range alignment procedure. Similar average range profiles are computed for each CPI part. In our scenario, $\Delta\theta_{RRM}$ is approximately 1.88° , leading to averaging over the whole CPI in case of uniform rotation and over $CPI/2$ in case of rotational acceleration. In Fig. 6(b) the range profile history for the 8th CPI, after range alignment application, is shown. In Fig. 7, reconstructed ISAR images are presented for SNR equal to 15dB and γ set to 0.64 rad/sec^2 for the 8th CPI. A set of images is included: previous CPI, unfocused CPI, next CPI and unfocused CPI after the application of CPI-split auto-focusing algorithm. We can easily notice that the proposed autofocusing process eliminates the significant ISAR image smearing (Fig. 7, b).

The entropy values for the obtained ISAR images for both 4th and 8th CPI are included in Table 3. Focus improvement is also validated through these results. It is remarkable that the algorithm reaches the optimum combination (minimum entropy) at different CPI-split stages for each unfocused CPI, due to aspect angle variation of image quality.

Table 3. Entropy values for presented ISAR images

ISAR Image Case	Entropy	Minimum Entropy Combination
3 rd CPI	5.8814	
4 th CPI, Unfocused	6.9807	
5 th CPI	5.7726	
4 th CPI, Focused	5.7696	stage 2, segment 1, comb. 1
7 th CPI	5.9072	
8 th CPI, Unfocused	7.0197	
9 th CPI	5.7563	
8 th CPI, Focused	5.7621	stage 4, segment 2, comb. 8

Conclusions

In this paper, an ISAR autofocusing method is developed for small, rapidly maneuvering air targets. Accelerated rotational motion is compensated through the combination of a conventional range alignment technique and the proposed autofocusing algorithm. In this way, the computational complexity of the polar reformatting process can be avoided. Based on ISAR image entropy minimization criterion, the proposed algorithm neglects data leading to ISAR images of poor quality and uses only data

leading to ISAR images of superior quality. Simulation results verify the adaptiveness of the autofocus procedure to different ISAR imaging conditions. Moreover, the ISAR image entropy variation with respect to aspect angle, signal-to-noise ratio

and target rotation parameters is quantified. This is considered to be the first step towards the automation of the proposed autofocus algorithm, for application to real field data.

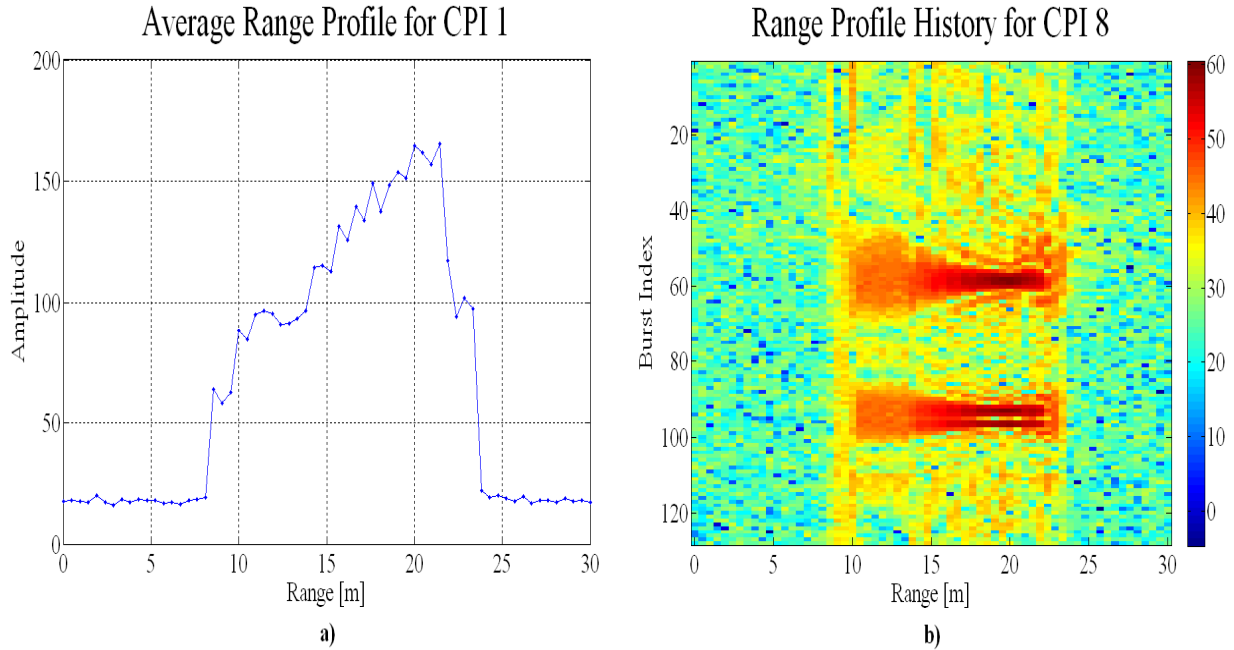


Fig. 6. a – Average range profile for 1st CPI (reference range profile for cross-correlation based range alignment); b – Range profile history for 8th CPI, after range alignment

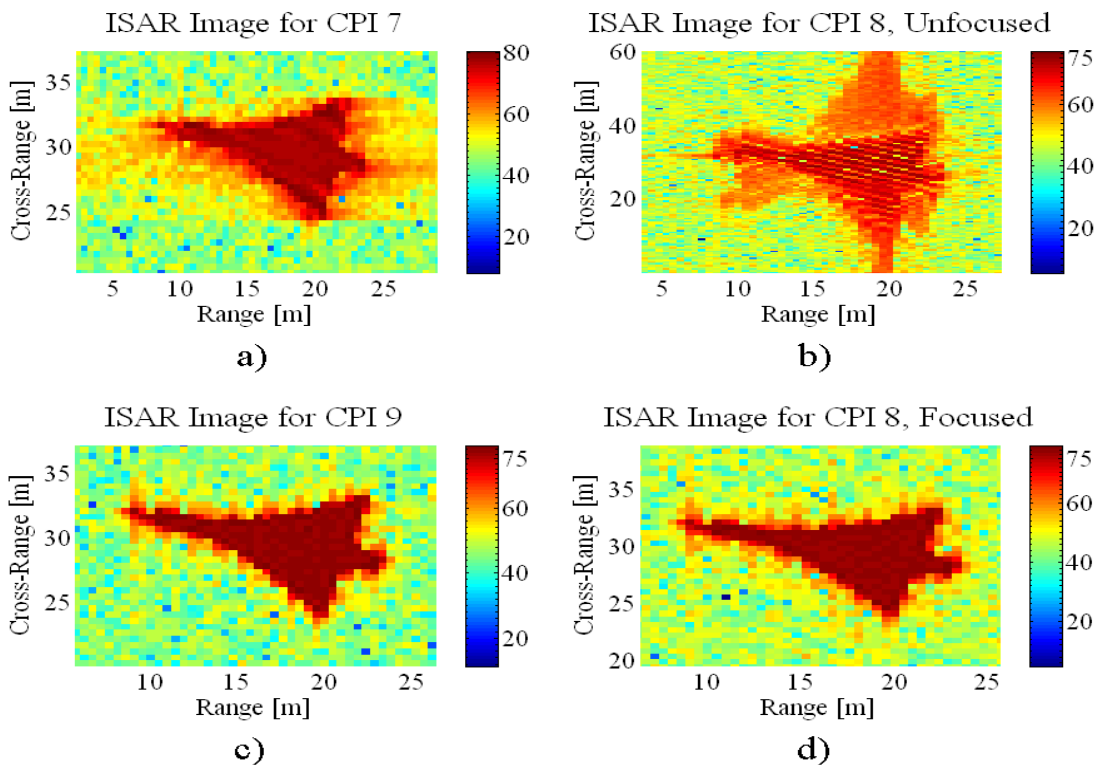


Fig. 7. Reconstructed ISAR images: a – 7th CPI (previous CPI); b – 8th CPI (unfocused CPI); c – 9th CPI (next CPI); d – 8th CPI, after CPI-split autofocusing

References

- [1] D. Wehner, *High-Resolution Radar*, Artech House, 2nd edition, 1995.
- [2] V. Chen, and H. Ling, *Time-Frequency Transforms for Radar Imaging and Signal Analysis*, Artech House, 2002.
- [3] Li Xi, Liu Guosui, and Jin Lin Ni, "Autofocusing of ISAR Images Based on Entropy Minimization", *IEEE Trans. Aerospace Electron. Systems*, Vol. 35, No. 4, Oct. 1999, pp. 1240-1252.
- [4] T. Thayaparan, L. Stankovic, C. Wernic, and M. Dakovic, "Real-time motion compensation, image formation and image enhancement of moving targets in ISAR and SAR using S-method based approach", *IET Signal Processing*, Vol. 2, No. 3, Sept. 2008, pp. 247-264.
- [5] A. Lazarov, and C. Minchev, "ISAR Signal Modeling and Image Reconstruction with Entropy Minimization Autofocusing", *Proc. DASC*, Portland, USA, Oct. 2006, pp. 3E5-1-3E5-11.
- [6] M. Martorella, F. Berizzi, and B. Haywood, "Contrast maximization based technique for 2-D ISAR autofocusing", *IEE Proc. Radar Sonar Navig.*, 2005, Vol. 152, No. 4, Aug. 2005, pp. 253-262.
- [7] Yu Jizhou, and Jiao Yun, "Research on Motion Compensation Algorithm for Stepped Frequency ISAR Synthetic Aperture Radar", *APSAR 2009*, Oct. 2009, pp. 626-629.
- [8] A. Karakasiliotis, A. Lazarov, P. Frangos, G. Boultadakis, and G. Kalognomos, "Two-dimensional ISAR model and image reconstruction with stepped frequency-modulated signal", *IET Signal Processing*, Vol. 2, No. 3, Sept. 2008, pp. 277-290.
- [9] E. Kallitsis, A. Karakasiliotis, G. Boultadakis, and P. Frangos, "A Fully Automatic Autofocusing Algorithm for Post-processing ISAR Imaging based on Image Entropy Minimization", *Electronics and Electrical Engineering Journal*, Vol. 110, No. 4, April 2011, pp. 125-130.
- [10] S. Wong, E. Riseborough, and G. Duff, "A Numerical Model of ISAR Distortion and an Efficient Procedure for Restoring Distorted ISAR Images", *Proc. RTO SET Symposium on Target Identification and Recognition Using RF Systems*, Oslo, Norway, Oct. 2004, pp. P2-1-P2-16.
- [11] R. van der Heiden, *Aircraft Recognition with Radar Range Profiles*, PhD Thesis, Univ. Amsterdam, Oct. 1998, p. 47.

UNSYMMETRICAL ELECTROMAGNETIC WAVE DIFFRACTION BY A LONG PIPE

*Seil Sautbekov**, *Gulnar Alkina** and *Panayiotis Frangos†*

Preferred Conference Session: Scattering of Electromagnetic Waves

Abstract

Diffraction of an unsymmetrical electromagnetic wave by a long pipe coaxially oriented inside an infinite waveguide is considered. The corresponding boundary value problem is reduced to a system of singular integral equations concerning the Fourier component of the surface current density. The exact solution of the above system of equations is constructed by the Wiener-Hopf-Fok method in a class of analytical functions and it is defined in the form of sum of partial waves.

1. Introduction

Unsymmetrical E_{nm} (electrical or TM) and H_{nm} (magnetic or TE) waves ($m = 1, 2, 3, \dots$) differ from symmetrical waves ($m = 0$) that the diffraction field of unsymmetrical waves is characterized by two scalar functions which correspond to a longitudinal component of electric and magnetic Hertz's vectors according to the following equations [1]:

$$\Pi_z^e = \sin(m\varphi + \varphi_0)\Pi(r, z), \quad \Pi_z^m = \cos(m\varphi + \varphi_0)\tilde{\Pi}(r, z).$$

The presence of the two Hertz potentials complicates the derivation of the boundary value problem by Wiener-Hopf-Fok method [2, 3]. However the exact solution of this problem can be obtained by some generalization of the corresponding axially symmetrical problem.

Electromagnetic fields are expressed in terms of the functions Π and $\tilde{\Pi}$ as follows:

$$\begin{aligned} E_r &= \sin(m\varphi + \varphi_0) \left(\frac{\partial^2}{\partial r \partial z} \Pi - i \frac{mk}{r} W \tilde{\Pi} \right), \\ E_\varphi &= \cos(m\varphi + \varphi_0) \left(\frac{m}{r} \frac{\partial}{\partial z} \Pi - ikW \frac{\partial}{\partial r} \tilde{\Pi} \right), \\ E_z &= \sin(m\varphi + \varphi_0) \left(\frac{\partial^2}{\partial z^2} + k^2 \right) \Pi, \\ H_r &= \cos(m\varphi + \varphi_0) \left(\frac{\partial^2}{\partial r \partial z} \tilde{\Pi} - i \frac{mk}{r} W^{-1} \Pi \right), \\ H_\varphi &= -\sin(m\varphi + \varphi_0) \left(\frac{m}{r} \frac{\partial}{\partial z} \tilde{\Pi} - ikW^{-1} \frac{\partial}{\partial r} \Pi \right), \end{aligned}$$

* Eurasian National University 5, Munaitpassov Str., Astana, Kazakshtan. e-mail: sautbek@mail.ru, gulnar.alkina@mail.ru.

† National Technical University of Athens, 9, Iroon Polytechniou Str., GR 157 73, Zografou, Athens, Greece.
e-mail: pfrangos@central.ntua.gr.

$$H_z = \cos(m\varphi + \varphi_0) \left(\frac{\partial^2}{\partial z^2} + k^2 \right) \tilde{\Pi}, \quad W = \sqrt{\frac{\mu}{\varepsilon}}, \quad k = \frac{\omega}{c}.$$

The constant angle φ_0 is determined by polarization of the wave impinging on the end of the circular waveguide.

Note that electromagnetic field of E_{mn} waves is defined by electric Hertz function Π from the abovementioned formulas, and electromagnetic field of waves H_{mn} by magnetic Hertz function $\tilde{\Pi}$.

Thus it is necessary to consider jointly unsymmetrical waves E_{m1}, E_{m2}, \dots and H_{m1}, H_{m2}, \dots for the given value m ($m=1, 2, 3 \dots$), as they are transformed each other at reflection from the end of the waveguide.

2. Statement of the problem

Let two waves are incident from the right to the left at the end of the long pipe with infinitely thin wall of radius a_i located coaxially in the basic waveguide of radius a : one is unsymmetrical TM-wave with amplitude A and wave number h and the other is unsymmetrical TE-wave with amplitude B and wave number \tilde{h} (fig. 1).

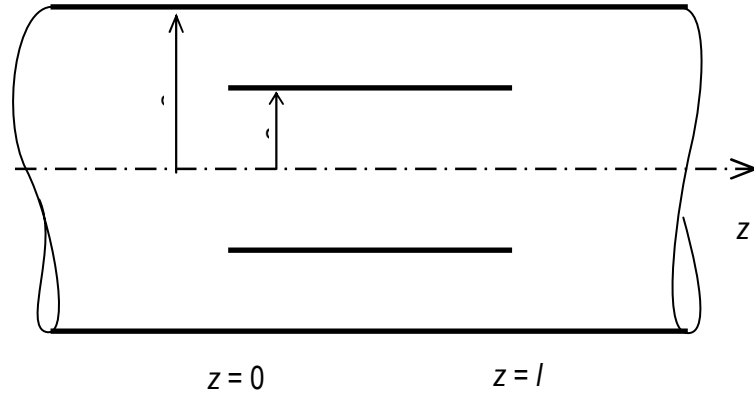


Fig. 1

The problem solution should satisfy the following boundary conditions:

$$E_z = E_\varphi = 0 \text{ at } r = a, \quad -\infty < z < \infty; \quad r = a_i, \quad 0 \leq z \leq l, \quad (1)$$

$$J_\varphi = H_z(a_i - 0, \varphi, z) - H_z(a_i + 0, \varphi, z) = 0 \text{ at } z < 0, \quad z > l, \quad (2)$$

$$J_z = H_\varphi(a_i + 0, \varphi, z) - H_\varphi(a_i - 0, \varphi, z) = 0 \text{ at } z \leq 0, \quad z \geq l, \quad (3)$$

where J_φ, J_z are azimuthally and longitudinal components of the surface current density.

The electrical and magnetic Hertz functions Π and $\tilde{\Pi}$ should be the solutions of the equation:

$$\frac{1}{r} \frac{\partial}{\partial r} \left(r \frac{\partial}{\partial r} \Pi \right) + \frac{\partial^2}{\partial z^2} \Pi + \left(k^2 - \frac{m^2}{r^2} \right) \Pi = 0. \quad (4)$$

3. Solution of the problem

We are looking for Hertz functions according to equation (4) in the following form [1]:

$$\Pi = -i \frac{\pi a_1}{2k} W \int_C \exp(iwz) L(r, w) F(w) dw, \quad (5)$$

$$\tilde{\Pi} = \frac{\pi a_1}{2} \int_C \exp(iwz) L(r, w) \frac{F(w)}{v} dw, \quad (6)$$

where $v = \sqrt{k^2 - w^2}$,

$$L(r, w) = \frac{1}{J_m(va)} \begin{cases} J_m(vr)(a_1, a), & r \leq a_1 \\ J_m(va_1)(r, a), & r \geq a_1 \end{cases},$$

$$L(r, w) = \frac{1}{J'_m(va)} \begin{cases} J_m(vr)(a'_1, a'), & r \leq a_1 \\ J'_m(va_1)(r, a'), & r \geq a_1 \end{cases},$$

$$(r, a) = J_m(vr) N_m(va) - J_m(va) N_m(vr),$$

$$(r, a') = J_m(vr) N'_m(va) - J'_m(va) N_m(vr),$$

$$(r', a') = J'_m(vr) N'_m(va) - J'_m(va) N'_m(vr),$$

$J_m(x)$ is the Bessel function, $N_m(x)$ is the Neumann function, C is the integration contour in the complex plane w lying along the real axis and consisting of an infinitely narrow loop enveloping a point h and \tilde{h} from below, F and \tilde{F} are the decision functions.

The boundary value problem is reduced with the help of the boundary conditions (1) – (3) to the system of the following functional integral equations:

$$\int_C \exp(iwz) \left(i \frac{mw}{k^2 a_1} LF(w) + LF(w) \right) dw = 0 \quad \text{at } 0 \leq z \leq l, \quad (7)$$

$$\int_C \exp(iwz) v^2 LF(w) dw = 0 \quad \text{at } 0 \leq z \leq l, \quad (8)$$

$$\int_C \exp(iwz) F(w) dw = 0 \quad \text{at } z < 0, \quad z > l \quad (9)$$

$$\int_C \exp(iwz) \left(F(w) + i \frac{mw}{a_1 v^2} F(w) \right) dw = 0 \quad \text{at } z \leq 0, \quad z \geq l, \quad (10)$$

where the following notation is introduced : $L \equiv L(a_1, w)$, $L' \equiv L(a'_1, w)$.

Taking into account that the edges of the pipe are secondary sources of waves, the Fourier-component of the current density is constructed by Wiener-Hopf-Fok method as a sum from two analytical sources in the form of natural space harmonics forward and backward:

$$F(w) = \frac{1}{(k-w)L_-} \left(C_1^+(w) + \frac{C_1}{w+k} \right) + \frac{\exp(-iwl)}{(k+w)L_+} \left(C_2^-(w) + \frac{C_2}{w-k} + \frac{D_2}{w+h} \right), \quad (11)$$

$$F(w) = \frac{1}{L_-} \left(\frac{B_1}{w+k} + \frac{A_1}{w-k} + E_1^+(w) \right) + \frac{\exp(-iwl)}{L_+} \left(\frac{B_2}{w+k} + \frac{A_2}{w-k} + E_2^-(w) + \frac{F_2}{w+\tilde{h}} \right), \quad (12)$$

where $C_1, C_2, D_2, A_1, A_2, B_1, B_2, F_2$ are constants, $C_1^+(w), E_1^+(w)$ are analytical functions on the upper complex w plane, $C_2^-(w), E_2^-(w)$ are analytical functions on the lower complex plane.

As the integral along an infinitely narrow loop of the contour C corresponds to amplitude of the incident wave, it is easy to calculate the values of the following constants:

$$D_2 = A \frac{k}{\pi^2 a_1} \frac{L_-(a_1, h)}{(k+h)} \exp(-ihl) \frac{J_m(va)}{(a_1, a)} \Big|_{v=\sqrt{k^2-h^2}}, \quad (13)$$

$$F_2 = -i \frac{B}{\pi^2 a_1} L_-(a_1, \tilde{h}) \exp(-i\tilde{h}l) \frac{J'_m(va)}{(a'_1, a')} \Big|_{v=\sqrt{k^2-\tilde{h}^2}}. \quad (14)$$

Similarly we have

$$B_1 = -B_2 \frac{L_+(a_1, k)}{L_-(a_1, k)} \exp(ikl),$$

$$A_2 = -A_1 \frac{L_+(a_1, k)}{L_-(a_1, k)} \exp(ikl).$$

By substituting expressions (11), (12) into the system of the integral equations (7) - (10) and closing the integration contour C in the upper half-plane or in the lower half-plane along the infinite semicircle according to Jordan's lemma, it is easy to obtain the system of the linear algebraic and functional equations, as following:

$$\begin{aligned} & \frac{C_1}{2k L_+(a_1, k)} + \frac{1}{L_-(a_1, k)} \left(C_2^-(-k) - \frac{C_2}{2k} + \frac{D_2}{h-k} \right) \exp(ikl) = \\ & = \frac{im}{2a_1} \left[\frac{1}{L_+(a_1, k)} \left(E_1^+(-k) - \frac{A_1}{2k} \right) + \frac{1}{L_-(a_1, k)} \left(E_2^-(-k) - \frac{A_2}{2k} + \frac{F_2}{\tilde{h}-k} \right) \exp(ikl) \right], \end{aligned} \quad (15)$$

$$\begin{aligned} & \frac{1}{L_-(a_1, k)} \left(\frac{C_1}{2k} + C_1^+(k) \right) + \frac{C_2}{2k L_+(a_1, k)} \exp(-ikl) = \\ & = \frac{im}{2a_1} \left[\frac{1}{L_-(a_1, k)} \left(E_1^+(k) + \frac{B_1}{2k} \right) + \frac{1}{L_+(a_1, k)} \left(E_2^-(k) + \frac{B_2}{2k} + \frac{F_2}{\tilde{h}+k} \right) \exp(-ikl) \right]. \end{aligned} \quad (16)$$

$$\begin{aligned} & \left(\frac{im}{a_1 k} \frac{L_-(a_1, k)}{2k} C_2 + L_-(a_1, k) A_2 \right) \exp(-ikl) + L_+(a_1, k) A_1 = \\ & = \frac{im}{a_1 k} L_+(a_1, k) \left(\frac{C_1}{2k} + C_1^+(k) \right), \end{aligned} \quad (17)$$

$$\begin{aligned} \frac{im}{a_1 k} \left(L_-(a_1, k) \frac{C_1}{2k} + L_+(a_1, k) \left(\frac{C_2}{2k} - C_2^-(-k) + \frac{D_2}{k-h} \right) \exp(ikl) \right) = \\ = L_-(a_1, k) B_1 + L_+(a_1, k) B_2 \exp(ikl). \end{aligned} \quad (18)$$

$$C_1^+(w) = - \sum_{n=1}^{\infty} \frac{\exp(iw_n l)}{w + w_n} \frac{L_+(a_1, w_n)}{L_-^*(a_1, w_n)} \frac{(k + w_n)}{(k - w_n)} \left(C_2^-(-w_n) - \frac{C_2}{k + w_n} + \frac{D_2}{h - w_n} \right), \quad (19)$$

$$C_2^-(w) = - \sum_{n=1}^{\infty} \frac{\exp(iw_n l)}{w - w_n} \frac{L_+(a_1, w_n)}{L_-^*(a_1, w_n)} \frac{(k + w_n)}{(k - w_n)} \left(C_1^+(w_n) + \frac{C_1}{k + w_n} \right), \quad (20)$$

where w_n are the zeros of L_- ($n = 1, 2, \dots$),

$$L_-^*(a_1, w_n) = \lim_{w \rightarrow w_n} (w - w_n)^{-1} L_-(a_1, w).$$

It is necessary to note, reasonably, the convergence of the infinite series, on account of exponential convergence, and in consideration of all traveling spatial harmonics and of some damped harmonics with imaginary wave numbers. Thus, the boundary value problem was reduced to the solution of a finite system of linear algebraic equations.

References

- [1] L. A. Weinstein, *The Theory of Diffraction and the Factorization Method*, Golem Press, Boulder, Colorado, 1969.
- [2] V. G. Daniele and G. Lombardi, Wiener-Hopf Solution for Impenetrable Wedges at Skew Incidence, *IEEE Trans. Antennas and Propagation*, Vol. 54, 9, 2472 - 2485 (2006).
- [3] B. Noble, *Methods based on the Wiener-Hopf technique*, 2nd ed., New York, Chelsea, 1988.

A NONFEASIBLE QUADRATIC APPROXIMATION RECURRENT NEURAL NETWORK FOR EQUALITY CONSTRAINED OPTIMIZATION PROBLEMS

Maria P. Barbarosou* and Nicholas G. Maratos**

*Hellenic Air-Force Academy, Department of Aeronautical Sciences,
Division of Electronics and Communication Engineering
Dekelia Air Force Base, GR 1010, Greece,
E-mail: mbarbar@teipir.gr.

**National Technical University of Athens, School of Electrical and Computer Engineering,
9 Iroon Polytechniou St., GR 15773, Athens, Greece,
E-mail: maratos@ece.ntua.gr.

Abstract

Convex optimization techniques are widely used in the design and analysis of communication systems and signal processing algorithms. In this paper a novel recurrent neural network is presented for solving nonlinear strongly convex equality constrained optimization problems. The proposed neural network is based on recursive quadratic programming for nonlinear optimization, in conjunction with homotopy method for solving nonlinear algebraic equations. It constructs generally a non-feasible trajectory which satisfies the constraints as $t \rightarrow \infty$. The boundedness of solutions and the global convergence to the optimal point of the problem are proven. The correctness and the performance of the proposed neural network are evaluated by simulation results on illustrative numerical examples.

1. Introduction

The use of convex optimization is ubiquitous in communications and signal processing. Many problems in these fields can be converted into convex optimization problems, which greatly facilitate their analysis and numerical solutions [1]-[2].

Consider the following equality constrained optimization problem:

$$(P) \quad \min \{f(x), A^T x - b = 0\} \quad (1)$$

where $f: \mathbb{R}^n \rightarrow \mathbb{R}$, A an $n \times m$ matrix with $m < n$ and b an m vector. We make the following assumption, standard for quadratic approximation programming:

Assumption: (a) The function f is strongly convex and twice continuously differentiable in \mathbb{R}^n . (b) The matrix A has full rank.

Since Tank and Hopfield's pioneering work [3]-[5] on linear programming neural network and ana-

logue circuits, the recurrent neural network approach for solving nonlinear programming has received a great of attention in the last two decades, see [6]-[13] and the references therein. Different approaches towards designing such networks have been developed. Some neural networks employed penalty functions [3]-[7], or the logarithmic barrier function [8], while others [9]-[10] make direct use of the Lagrangian function. In [11] a neural network for solving linear projection equations is described. More recently, neural networks based on gradient projection method for nonlinear programming are designed [12]-[13].

The proposed neural network does not make use of a penalty function or of a projection equation. It solves the problem directly, based on a combination of the recursive quadratic programming [14] and the continuous Newton-Raphson method [14] for solving the constraint equations.

The remainder of the paper is organized as follows. The new neural network description is presented in Section II. In Section III we prove the global convergence to the optimal point of (P). Illustrative examples are given in Section IV. Finally Section V concludes the paper.

2. Derivation of the proposed neural network

Let $L(x, \lambda) = f(x) + \lambda^T (A^T x - b)$ be the Lagrangian function for problem (P), where $\lambda \in \mathbb{R}^m$ is the vector of Lagrangian multipliers.

Since J is strongly convex, It is well known [14] that if the optimal point of (P) exists, then it is unique, and also there exist vector λ^* such that:

$$\nabla L(x^*, \lambda^*) = 0 \quad \text{and} \quad A^T x^* - b = 0, \quad \text{where}$$

$$\nabla L(x, \lambda) = \nabla f(x) + \lambda^T (A^T x - b).$$

In the first instance, we consider the following system of implicit ordinary differential equations:

$$\dot{x}(t) = -\rho e^{-\rho t} \nabla L(x(t), \lambda(t)) \quad (2.1)$$

$$A^T x(t) - b = e^{-\rho t} (A^T x_0 - b) \quad (2.2)$$

where $(x(t), \lambda(t))$ the solution of system (2) with initial point $(x_0, \lambda_0) = (x(0), \lambda(0))$ and ρ positive constant. Obviously, the norms of $\nabla L(x, \lambda)$ and the equality constraints are decreasing along the solution of system (2). Differentiation of (2) with respect to t gives:

$$\frac{\partial^2 L(x, \lambda)}{\partial^2 x} \dot{x} + \frac{\partial^2 L(x, \lambda)}{\partial \lambda \partial x} \dot{\lambda} = -\rho e^{-\rho t} \nabla L(x, \lambda)$$

$$A^T \dot{x} = -\rho e^{-\rho t} (A^T x - b)$$

where \dot{x} stand for \dot{x} and $\dot{\lambda}$ respectively.

Since $\frac{\partial^2 L(x, \lambda)}{\partial^2 x} = \frac{\partial^2 f(x)}{\partial^2 x}$ the above

system in matrix form is written as:

$$\begin{bmatrix} \frac{\partial^2 f(x)}{\partial^2 x} & A \\ A^T & 0 \end{bmatrix} \begin{bmatrix} \dot{x} \\ \dot{\lambda} \end{bmatrix} = -\rho \begin{bmatrix} \nabla L(x, \lambda) \\ A^T x - b \end{bmatrix} \quad (3)$$

The system (3) is linear with respect of the vector $\begin{bmatrix} \dot{x} \\ \dot{\lambda} \end{bmatrix}$. We solve the system via QR decomposition of the matrix A [15]. Namely, A is decomposed as:

$$A = Q \begin{bmatrix} R \\ 0 \end{bmatrix} = [Q_1 \ Q_2] \begin{bmatrix} R \\ 0 \end{bmatrix} = Q_1 R$$

where Q is an n -unitary matrix, R is an $m \times m$ upper triangular matrix. The matrices Q_1 and Q_2 consist of the first m and the last $n-m$ columns of Q , respectively. Under the *Assumption*, the matrix

$$\begin{bmatrix} \frac{\partial^2 f(x)}{\partial^2 x} & A \\ A^T & 0 \end{bmatrix}$$

is invertible. So the system (3) can be

solved for $\begin{bmatrix} \dot{x} \\ \dot{\lambda} \end{bmatrix}$ yielding:

$$\dot{x} =$$

$$-\rho [M(x) \nabla f(x) + N(x) (A^T x - b)] \quad (4.1)$$

$$\dot{\lambda} =$$

$$-\rho [\lambda + N(x)^T \nabla f(x) + O(x) (A^T x - b)] \quad (4.2)$$

where:

$$M(x) = Q_2^T \left(Q_2^T \frac{\partial^2 f(x)}{\partial^2 x} Q_2 \right)^{-1},$$

$$N(x) = \left(I_n - M(x) \frac{\partial^2 f(x)}{\partial^2 x} \right) Q_1 (R^T),$$

$$O(x) = -R^{-1} Q_1^T \frac{\partial^2 f(x)}{\partial^2 x} N,$$

In the following proposition a Lyapunov function for dynamical system (4) is given.

Proposition: Let the *Assumption* hold, then the function $V : \mathbb{R}^{n+m} \rightarrow \mathbb{R}$ be defined as:

$$V(x, \lambda) = \frac{1}{2} (\|\nabla L(x, \lambda)\|^2 + \|A^T x - b\|^2)$$

is decreasing along the solution of (4) and approaches zero as time tends to infinity, where $\|\cdot\|$ is the Euclidean norm.

Proof: Finding the directional derivative of $V(x, \lambda)$ in the direction of the solution of (4) we obtain

$$\frac{dV(x, \lambda)}{dt} = \nabla_x V(x, \lambda) \dot{x} + \nabla_\lambda V(x, \lambda) \dot{\lambda} =$$

$$\begin{bmatrix} \nabla L(x, \lambda) \\ A^T x - b \end{bmatrix}^T \begin{bmatrix} \frac{\partial^2 f(x)}{\partial^2 x} & A \\ A^T & 0 \end{bmatrix} \begin{bmatrix} \dot{x} \\ \dot{\lambda} \end{bmatrix}$$

where ∇_x and ∇_λ denote the gradients with respect to x and λ , respectively.

Since the systems (3) and (4) are equivalent, from (3) we have

$$\frac{dV(x, \lambda)}{dt} =$$

$$-2\rho (\|\nabla L(x, \lambda)\|^2 + \|A^T x - b\|^2) < 0$$

which means that

$$\frac{dV(x, \lambda)}{dt} = -\rho V(x, \lambda) \quad (5)$$

From (5) it follows that the function $V(x, \lambda)$ is decreasing exponentially along the solution of (4). This proves the assertions of the proposition.

The dynamics of the proposed neural network are defined in explicit form, by the system of differential equations (4.1). This is an autonomous dynamical system for x , since the multipliers λ on its right hand side has been eliminated. A block dia-

gram realization of our neural network is given in Fig.1.

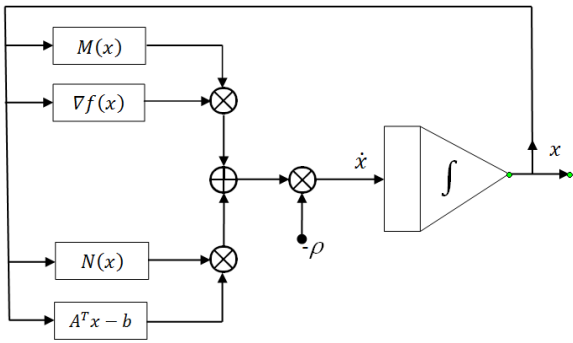


Figure 1. Block diagram realization of the proposed neural network

3. Global convergence

The solution of a dynamical system is said to be globally convergent to a point x^* if for any initial point $x_0 \in F$ $\lim_{t \rightarrow \infty} \{x(t)\} = x^*$. This result can be derived [16] by the boundedness of the solution x , and the existence of a Lyapunov function with zero gradient at x^* .

Theorem: Let the Assumption hold, and let x^* be the unique minimize of problem (P). Then the solution of (4.1) starting from any initial point, is bounded, extends to infinite time and converges to x^* , i.e.

$$\lim_{t \rightarrow \infty} \{x(t)\} = x^*$$

Proof: The following relationships are used throughout this proof

$$Q_1 Q_1^T + Q_2 Q_2^T = I_m, Q_1 R = A, Q_1^T Q_2 = 0$$

$$Q_1^T Q_1 = I_m, A^T x^* - b = 0$$

We shall first show that the solution x of (4.1) is bounded. It holds that

$$\dot{x} - x^* = (Q_1 Q_1^T + Q_2 Q_2^T)(x - x^*) \quad (6)$$

Premultiplication (4.1) by $(x - x^*)^T Q_1$ after simple algebra, we get

$$\frac{d\|Q_1^T(x - x^*)\|^2}{dt^2} = -2\rho\|Q_1^T(x - x^*)\|^2 \quad (7)$$

This simply states that $\|Q_1^T(x - x^*)\|^2$ hence $\|A^T x - b\|^2$ are bounded along the solution of (4.1). From this result and Proposition we have that $\|\nabla L(x, \lambda)\|^2$ is also bounded along the solution of

(4). Since $\|Q_2^T \nabla f(x)\| = \|Q_2^T \nabla L(x, \lambda)\|$ it follows that $\|Q_2^T \nabla f(x)\|^2$ is also bounded. Premultiplication (4.1) by $(x - x^*)^T Q_2$ after simple algebra, we get

$$\begin{aligned} \frac{d\|Q_2^T(x - x^*)\|^2}{dt^2} = & -2\rho(x - x^*)^T Q_2 Q_2^T M(x) \nabla f(x) \\ & + 2\rho(x - x^*)^T Q_2 Q_2^T M(x) \frac{\partial^2 f(x)}{\partial^2 x} (x - x^*) \\ & - 2\rho(x - x^*)^T Q_2 Q_2^T M(x) \frac{\partial^2 f(x)}{\partial^2 x} Q_2^T Q_2 (x - x^*) \end{aligned}$$

At this point we use the strongly convexity of the objective function, so it holds that [14]

$$\exists m > 0 : \frac{\partial^2 f(y)}{\partial^2 y} > m\|y\|^2, \forall y \in R^n$$

From the above property and the boundedness of

$\|Q_2^T \nabla f(x)$ and $\|Q_1^T(x - x^*)\|^2$, it follows that for some finite $\alpha, \beta, \gamma > 0$ it holds that

$$\begin{aligned} \frac{d\|Q_2^T(x - x^*)\|^2}{dt^2} \leq & -\alpha\|Q_2^T(x - x^*)\|^2 + \beta\|Q_2^T(x - x^*)\| + \gamma \end{aligned}$$

This result means that when $\|Q_2^T(x - x^*)\|^2$ touches a finite upper bound, it will start to decrease along the solution of (4.1), therefore

$\|Q_2^T(x - x^*)\|^2$ is bounded. Thus from (6) the solution of (4.1) is bounded, hence it extends to infinite time [16]. Since x is bounded, It can be proved easily from (4.2) that λ is also bounded.

Let the set D be defined as:

$$D = \left\{ (x, \lambda) \in R^{n+m} : \frac{dV(x, \lambda)}{dt} = 0 \right\}$$

where $V(x, \lambda)$ is the function of Proposition 1. Then from (5) we have

$$D = \{(x, \lambda) \in R^{n+m} : \|\nabla L(x, \lambda)\| = 0 \text{ and } \|A^T x - b\| = 0\}$$

hence because of the Assumption $D = \{x^*, \dots\}$. Since $(x(t), \lambda(t))$ is bounded and satisfies Proposition, from LaSalle's Theorem [16] it follows that $(x(t), \lambda(t)) \rightarrow D = \{x^*, \dots\}$ as $t \rightarrow \infty$. This completes the proof.

4. Numerical Examples

The performance of our neural network is evaluated by using MATLAB for several test problems. In this section two illustrative examples are given. Example 1 has quadratic objective function and satisfies both parts of Assumption. To demonstrate the effectiveness of our neural network in more general optimization problems, we choose Example 2, whose objective function is a Gaussian as shown in Fig. 2, that is pseudoconvex. So, Example 2 satisfies only the part (b) of Assumption.

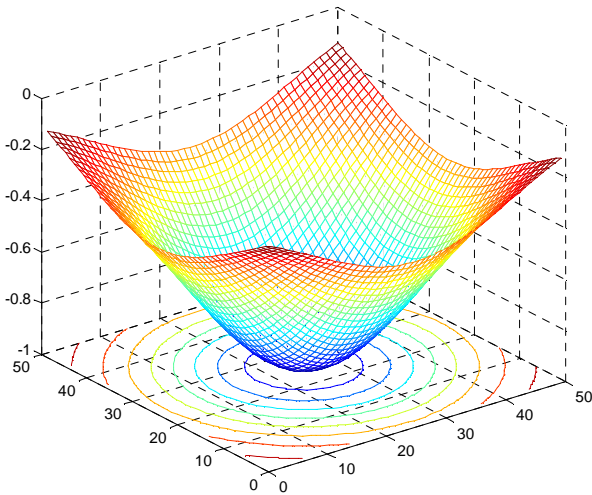


Figure 2. The 2D Gaussian function of Example 2

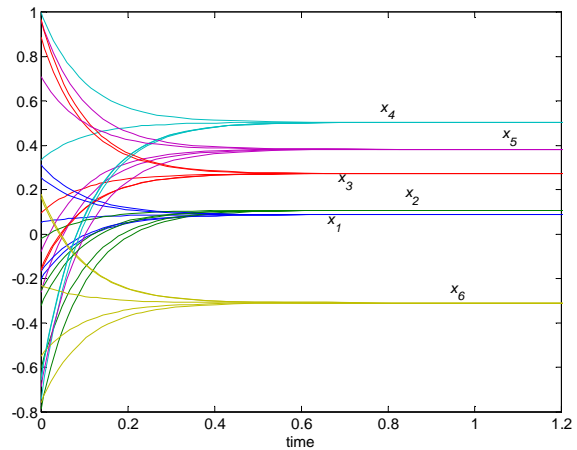
Example 1: Consider the following strongly convex problem [6], with $n =$ and $m =$:

$$\min_{x \in \mathbb{R}^6} \{ \|x\|^2 : A^T x - b = 0 \}$$

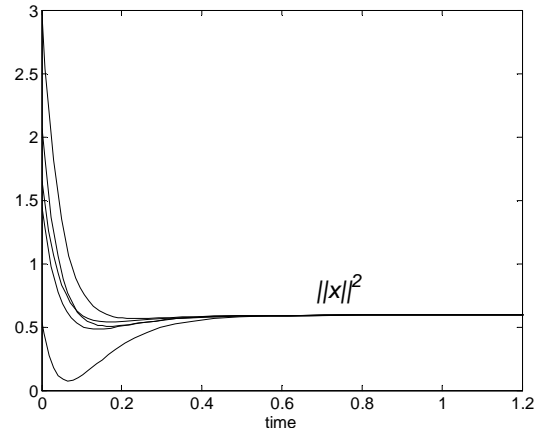
where $b^T = [2 \quad -1 \quad -$ and

$$A^T = \begin{bmatrix} 2 & -1 & 4 & 0 & 3 & 3 \\ 5 & 1 & -3 & 1 & 2 & 0 \\ 1 & -2 & 1 & -5 & -1 & 4 \end{bmatrix}$$

This problem has a unique global minimizer at x^* [0.08824674 0.010828343 0.27326648 0.50466163 0.38281032 -0.30970696], written to eighth decimal place. The trajectories x obtained by the proposed neural network with $\rho =$, starting from five random non-feasible initial points in $(-1 \ 1)$, are shown in Fig.2a. Fig.2b shows the convergence of the cost function for each case. At the end of the simulation, all trajectories reach with final error $e = \|x(t) - x^*$ of order 10^{-6} .



(a)



(b)

Figure 3. Example 1: (a) Trajectories x of the proposed neural network for 5 random initial points and (b) the corresponding cost functions, vs time

Example 2: Consider the following pseudoconvex optimization problem [9], with $n =$ and $m =$:

$$\min_{x \in \mathbb{R}^2} \{ e^{-(x_1^2 + x_2^2)} : A^T x - b = 0 \}$$

where $A = \begin{bmatrix} 0.7 \\ 0.5 \end{bmatrix}$ and $b = 0.8$.

This problem has a unique global minimizer at x^* [0.62745172 0.500937796], written to eighth decimal place. Fig. 3a shows the trajectories of the proposed neural network with $\rho =$, starting from fifteen non-feasible initial points, random generated from the uniform distribution over $(0,1)$. Fig.3b shows the convergence of the cost function for each case. At the end of the simulation, all trajectories reach with final error $e = \|x(t) - x^*$ of order 10^{-6} .

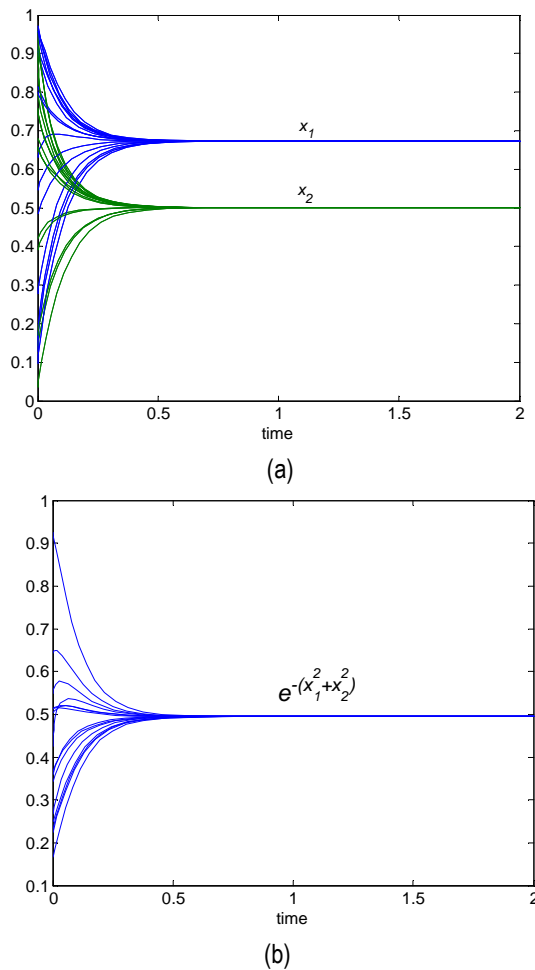


Figure 4. Example 2: (a) Trajectories of the proposed neural network for 15 random initial points and (b) the corresponding cost functions, vs time.

5. Conclusions

In this paper a recurrent neural network for strongly convex constrained optimization problem is presented, based on quadratic approximation method for nonlinear programming. If initial point is non-feasible, the proposed neural network defines a non-feasible trajectory which satisfies the constraints as $t \rightarrow \infty$. Global convergence is proven. Simulation on illustrative numerical examples substantiates the effectiveness and the correctness of the proposed neural network.

References

- [1] Z. Luo and W. Yu, "An introduction to convex optimization for communications and signal processing", *IEEE on Selected Areas in communications*, vol.24, pp. 1426-1438.
- [2] Z. Q. Luo, "Applications of convex optimization in signal processing and digital communication", *Math Program.*, 2003, pp. 177-207.
- [3] D.W. Tank and J.J. Hopfield, "Simple neural optimization networks: an A/D converter, signal decision circuit, and a linear programming circuit", *IEEE Trans. Circuits and Systems*, vol. 33, 1986, pp. 533-541.
- [4] L.O. Chua and G.-N. Lin, "Nonlinear programming without computation", *IEEE Trans. Circuits and Systems*, vol. 31, 1984, pp. 182-188.
- [5] M. Kennedy and L.O. Chua, "Unifying the Tank and Hopfield linear programming circuit and the canonical nonlinear programming circuit of Chua and Lin", *IEEE Trans. Circuits and Syst.*, vol. 34, 1986, pp. 210-214.
- [6] W. E. Lillo S. Hui and S. H. Zak, "Neural Networks for constrained optimization problems", *Int. J. of Circuit Th. And Appl.*, vol. 21, 2000, pp. 385-399.
- [7] A. Cichocki and R. Unbehauen, *Neural Networks for Optimization and Signal Processing*, John Wiley & Sons, 1993.
- [8] P.T. Krasopoulos and N.G. Maratos, "A neural network for convex optimization", in *Proc. ISCAS 2006*, pp.747-750.
- [9] S. Zhang and A.G. Constandinides, "Lagrange programming neural networks", *IEEE Trans. Circuits System II*, vol. 39, 1992, pp.441-452.
- [10] S. Zhang, X. Zhu and L.-H. Zou, "Second-order neural nets for constrained optimization", *IEEE Trans. Neural Networks*, vol. 3, 1992, pp. 1021-1024.
- [11] Y. Xia H. Leuhg and J. Wang, "A projection neural network and its application to constrained optimization problems", *IEEE Trans. Circuits and Systems*, vol. 13, 2002, pp. 337-350.
- [12] M. Barbarosou and N.G. Maratos, "A non -feasible gradient projection recurrent neural network for equality constrained optimization", in *Proc. IJCNN 2004*, pp.2251-2256.
- [13] M. Barbarosou and N.G. Maratos, "A non -feasible gradient projection recurrent neural network for equality constrained optimization problems", *IEEE Trans. Neural Networks*, vol 19, 2008, pp. 1665-1677.
- [14] D. Bertsekas, *Nonlinear Programming*, Athena Scientific, 1995.
- [15] G. Colub and C. Van Loan, *Matrix Computations*, Johns Hopkins University, 1996.
- [16] N. Rouche, P. Hebets, and M. Laloy, *Stability Theory by Liapunov's Direct Method*, Springer-Verlag, New York, 1977.

SCP RAKE RECEIVER – THE POSSIBLE SOLUTION OF N-LOS HAPS AND WIMAX MM-WAVE NETWORKS

Veselin Demirev

Radio Communications and Video Technologies Department, TU-Sofia, Kl. Ohridski blv. № 8, 1756-Sofia,
e-mail: demirev_v@tu-sofia.bg

Abstract

A new wireless technology, named SCP-RPSC, was proposed by the author several years ago to solve the antenna problems of mm-wave HAPS and WIMAX. The proposals deal with LOS mm wave propagation environment, which is accepted by the communication community as the only way to communicate in these frequency bands. However, in high building city environment most of the terminal links will be shadowed, which will need more and more new base stations. A possible solution is the NLOS mm-wave systems, working properly in high building city environment. The possibilities of SCP technology to create simultaneous several narrow virtual antenna beams could be a good solution of the problem, leading to effective use of the reflected beams by gathering the signals in phase at baseband.

To realize this idea in HAPS – WIMAX down links, the Rake-receiver principles are proposed in the report to recover the pilot signals of the different multipath components. After that, by means of several signal recovery correlators, according to the basic SCP technology signal processing, several virtual high gain antenna beams, directed towards the different reflecting points, are created. In such way the reflected signals will be received with high antenna gain and will be better isolated each other. The received in such way different multipath signals should be delayed in proper way and summed in phase at baseband.

The procedure for the HAPS-WIMAX up-links, using RPSC approach, will be similar to the previous case. The Rake receiver for the different pilots multipath components will be situated at the base station site and the signal processing will be similar too.

Block-schemes of a SCP-RPSC HAPS or WIMAX system, based on the described above principles of operation, are given in the report. A description of the multipath propagation phenomena, typical for high buildings city propagation, is given too.

1. Introduction

A new wireless technology, named SCP-RPSC (Spatial Correlation Processing – Random Phase Spread Coding), was proposed by the author several years ago to solve the antenna problems of mm-wave HAPS (High Altitude Platform Systems) [1,2] and WIMAX (World Interoperability for Micro-

wave Access) [3,4]. The proposals deal with LOS (Line Of Sight) mm-wave propagation environment, which is accepted by the communication community as the only way to communicate in these frequency bands. Possible applications of SCP-RPSC technology in HAPS LOS terminals are shown in fig. 1, in HAPS LOS base stations – in fig. 2, in HAPS feeder lines and inter HAP links – in fig. 3.

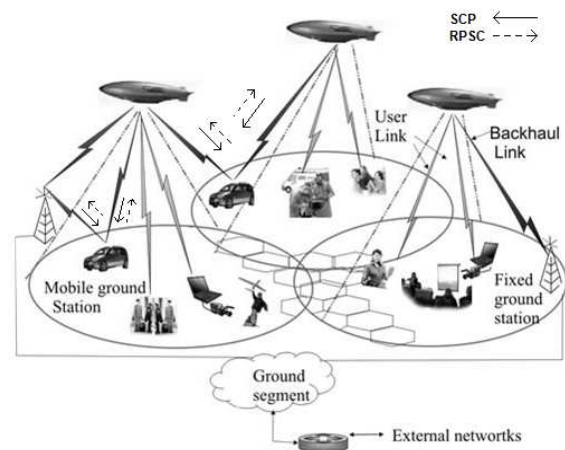


Figure 1. Possible applications of SCP-RPSC technology in HAPS LOS terminals

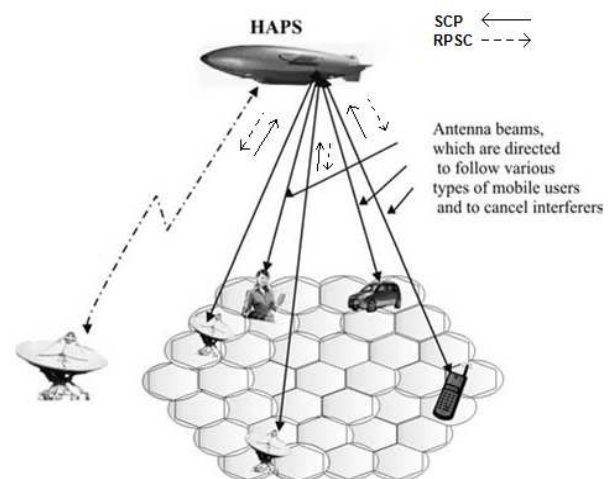


Figure 2. Possible applications of SCP-RPSC technology in HAPS LOS base stations

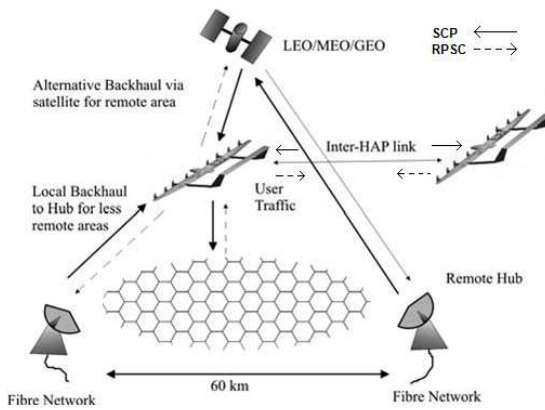


Figure 3. Possible applications of SCP-RPSC technology in HAPS feeder lines and inter HAP links

2. NLOS mm-wave HAPS and WIMAX systems

In high building city environment most of the terminal links will be shadowed, leading to necessity of more and more new earth and HAPS mounted base stations. Careful studies of the propagation phenomena at various operating frequencies for the case of HAPS based scenario, are given in [5,6]. In [5] the authors conclude, that LOS can be only guaranteed for large reception angles under the HAPS base station and the multipath effects will dominate in the most of the serviced area. Bearing in mind the roughness of the building walls, according to the Rayleigh criterion, the authors stated, that a typical wall may have reflection coefficient up to 98 % if the whole of the main beam is incident on the wall. According to the published data, for frequencies in the Ka-band the critical height is fairly small (0,2 cm), but for the IMT-2000, this critical height can be as much as 3,5 cm.

One of the best advantages of the famous CDMA technology is the ability to separate the different multipath components according to their time of arrival by means of multi-channel Rake receiver. CDMA is particular suitable for mobile low and medium speed wireless communications, but for broadband communications it is obviously unusable. A competing technology for this particular case was proposed by the author of this report, named RPSC-MA (Random Phase Spread Coding Multiple Access) [7].

For the reasons, mentioned above, the possibilities to create HAPS and WIMAX links in NLOS environment with SCP technology are of great impor-

tance. Another intuitive possible advantage, which should be studied in the future by the radio propagation community, is that the Rayleigh limitations could not be valid for the proposed system, because of the specific random phase spreading in the receiving SCP antenna array.

3. SCP technology in NLOS HAPS and WIMAX down links

One of the main advantages of SCP technology is the possibility to create simultaneous several narrow virtual antenna beams, represented by the SCCF (Spatial Cross-Correlation Functions). In satellite communications it gives the ability to the ground terminal for satellite space diversity and soft handover between different satellites. In our case the goal is the effective use of the reflected from the different buildings beams, gathering the energy of the multipath signals in phase at baseband (similar to the CDMA) – fig. 4.

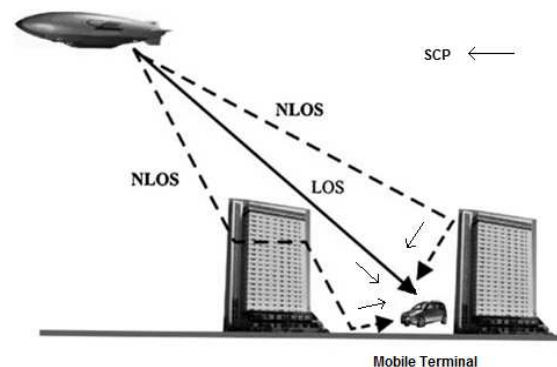


Figure 4. Possible applications of SCP-RPSC technology in HAPS mixed LOS and NLOS propagation environment

A block-scheme of a SCP Rake receiver for HAPS mixed LOS and NLOS propagation environment is shown in fig.5. Here a typical SCP receiver is used, but at low IF (Intermediate Frequency) several Rake channels are created. Each of them consists of pilot recovery unit and signal recovery unit. The pilot recovery units are fed by the used PN-code, properly time shifted according to the time offset of the different reflected signals. Each recovered pilot signal is sum of several thousands random phased signals (equal to the number of the antenna array elements). According to the CLT (Central Limit Theorem) such sum has Gaussian random distribution. In the signal recovery units the corresponding recovered pilots correlate with the spread in the same manner information signals, coming from the

nas not only in LOS conditions, but in NLOS environment too. As a result high capacity reliable broadband wireless networks will appear soon on the market, solving the communication problems of the big cities in 21-st century.

References

- [1] V. Demirev, M. Hicolova, "Application of the SCP-RPSC technology in broadband High Altitude Platform Systems", *Telecom,06*, Varna, 2006 (in Bulgarian).
- [2] V. Demirev, "The basic characteristics of the SCP-RPSC HAPS systems", *Telecom,10*, Sofia, Bulgaria, 2010 (in Bulgarian).
- [3] V. Demirev, "Application of SCP-RPSC Technology in Microwave Wi-Max Systems", *Telecom,07*, Varna, Bulgaria, 2007 (in Bulgarian).
- [4] V. Demirev, "SCP-RPSC WI-MAX systems – the new approach for the next generation microwave access strategies", *Caspian Telecoms,08*, Istanbul, Turkey, 2008.
- [5] A. Aragon-Zavala, J. Cuevas-Ruiz, J. Delgado-Penin, *High-Altitude Platforms for Wireless Communications*, Wiley, 2008.
- [6] D. Grace, M. Mohorcic, *Broadband Communications via High Altitude Platforms*, Wiley, 2011.
- [7] V. Demirev, "Random Phase Spread Coding Multiple Access - the New competitor of CDMA in the broadband wireless networks", *Journal of Applied Electromagnetism*, vol.13, Number 1(June 2011), pp. 26-32, Athens, Greece, 2011.
- [8] V. Demirev, A. Efremov, "Some Important Parameters of the SCP Technology", Proceedings of XXXX International Conference on Information, Communication and Energy Systems and Technologies ICEST'05, pp.516-518, Nis, Serbia and Montenegro, 2005.

A NEW APPROACH FOR PN-CODES GENERATION AND SYNCHRONIZATION IN CW MOBILE MULTISTATIC RADAR SYSTEMS

Veselin Demirev

Radio Communications and Video Technologies Department, TU-Sofia, Kl. Ohridski blv. № 8, 1756-Sofia,
e-mail: demirev_v@tu-sofia.bg

Abstract

Bistatic radars and multistatic radars are often designed for operation on high altitude platforms such as satellites and airplanes. In these cases problems with pseudo-noise code generation, synchronization and isolation appear when continuous wave – phase modulation is used. This mode of operation gives the opportunity for coherent signal processing, precise distance and 3-D coordinates measurements, as well as targets resolution by means of their Doppler spectra.

The goal of this report is to propose a new approach for pseudo-noise code generation and synchronization, suitable for mobile multistatic radar networks.

The proposed new principle uses several space distributed sources of radio-signals, phase modulated by appropriate pseudo-noise codes. A particular radar transmitter site receives these signals by means of the well known CDMA technology. For this purpose the same codes are generated and synchronized in the site receiver. The **mod2 sum** of these codes creates a new code, which we named Unique pseudo-noise code. It is used for spreading of the transmitted radar signal.

The basic SC-CDMA geometry of a particular mobile multistatic radar system, as well as mathematical description of the proposed method of code generation and synchronization are given in the report. A proposal for a real system, using the satellites of the global positioning system GPS as sources of the pseudo-noise signals, is given too.

1. Introduction

Bistatic radars and Multistatic Radar Networks (MRN) are subject to problems and special requirements that are either not encountered or encountered in less serious form by monostatic radars [1]. In general, the implementation of a MRN is more easily accomplished when the positions of all transmitting and receiving elements are fixed with respect to each other, for example when located on the ground. Because of the Line Of Sight (LOS) restrictions, they are often designed for op-

eration on high altitude platforms such as satellites and airplanes. Another particular application of satellite based global MRN is the protection of the Earth surface from meteors and asteroids. In these cases problems with Pseudo-Noise (PN)-code generation, synchronization and isolation appear when Continuous Wave - Phase Modulation (CW-PM) mode of operation is used. On the other hand CW-PM gives the opportunity for coherent signal processing, precise distance and 3-D coordinates measurements, as well as targets resolution by means of their Doppler spectra.

In fig. 1 the geometry associated with bistatic radars [2] is shown. It could be base configuration for a more sophisticated MRN. A synchronization link between the transmitter and receiver is necessary in order to maximize the receiver's knowledge of the transmitted signal so that it can extract maximum target information. The synchronization link may provide the receiver with the following information:

- The transmitted frequency in order to compute the Doppler shift;
- The transmit time or phase reference in order to measure the total scattered path $R_t + R_r$.

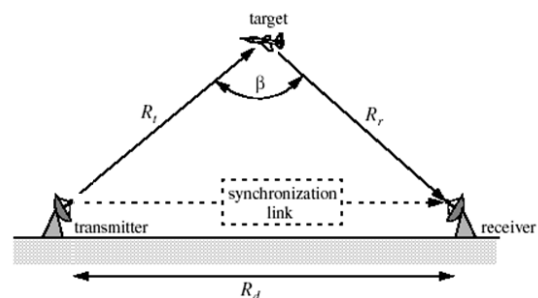


Figure 1. The basic bistatic radar geometry

Frequency and phase reference synchronization can be maintained through line-of-sight communications between the transmitter and receiver.

The goal of this report to propose a new approach for PN-code generation and synchronization in order to solve some of the problems of the future sophisticated fixed and mobile MRN,s. Similar approach was proposed by the author several years ago for a new s.c. Space Correlated (SC) CDMA method of access, used in satellite and terrestrial cellular networks for global mobile communications [3, 4].

2. SC-CDMA approach

The proposed SC-CDMA principle uses several space distributed sources of radio-signals, positioned at points O_1 and O_2 – fig. 2. The signals are phase modulated by appropriate PN-codes $C_1(t)$ and $C_2(t)$. The Mobile Stations (MS) receive these signals by means of the well known CDMA technology. For this purpose the same PN-codes are generated and synchronized in the MS receiver. The **mod2 sum** of these codes creates a new code, which we named U (Unique)-PN code. This code is used for spreading the transmitted by the MS information. Similar approach is used for generation of the Base Station (BS) U-PN codes.

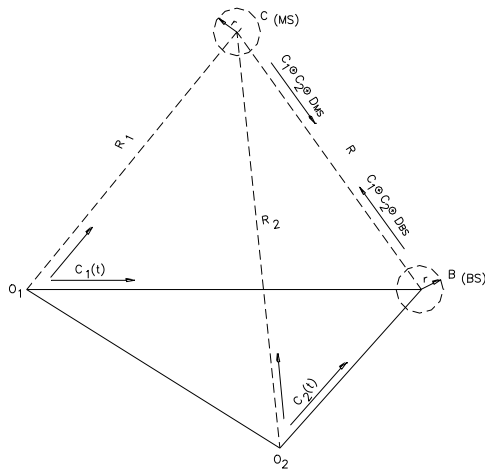


Figure 2. The basic SC-CDMA bistatic radar geometry

3. SC-MRN: the new approach to synthesize radar MRN-codes

The possible implementations of SC-CDMA approach in a bistatic radar geometry is shown in fig.3. BPSK modulated by PN-codes radiosignals are transmitted from the points O_1 and O_2 (both of them with known coordinates in a 2D coordinate

system). These signals are received in the transmitter site and in the receiver site of a bistatic radar system, where the used PN-sequences $C_1(t)$ and $C_2(t)$ are recovered with their phases and used as follows:

- **Transmitter site:**

$C_1(t)$ and $C_2(t)$ are **mod2sum** and the resulting U-PN code (eq.1) is used for BPSK modulation of the transmitted radio-signals. The phases of the received PN-codes are determined by the transmitter position. These coordinates are sent to the receiver with appropriate radio-communication link.

$$U - PN_{transmitter}(t) = C_1(\Omega_c t + \frac{2\pi}{\lambda_c} R_1) \oplus \oplus C_2(\Omega_c t + \frac{2\pi}{\lambda_c} R_2) \tag{1}$$

where λ_c is the wavelength and Ω_c is the angle frequency of the used PN-code.

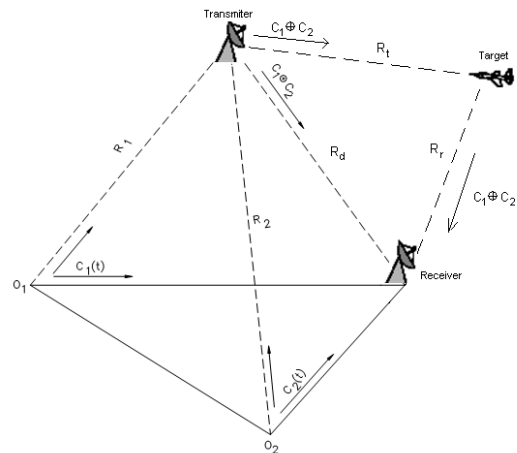


Figure 3. The basic SC-MRN geometry

- **Receiver site:**

The phases of the received PN-codes are determined by the receiver position in the same 2D-coordinate system. Receiver processor computes the distances R_1, R_2, R_d in order to recovery the transmitted U-PN code in the receiver with phase, given with eq. 2. The recovered U-PN code is used for acquisition and tracking of the synchronization link and with introducing the suitable time delay – for measuring the distance $R_t + R_r$ by means of eq.3.

$$U - PN_{receiver}^{synchronization}(t) = C_1 \left[\Omega_c t + \frac{2\pi}{\lambda_c} (R_1 + R_d) \oplus \right] \quad (2)$$

$$\oplus C_2 \left[\Omega_c t + \frac{2\pi}{\lambda_c} (R_2 + R_d) \right]$$

$$U - PN_{receiver}^{target-reflected}(t) = C_1 \left[\Omega_c t + \frac{2\pi}{\lambda_c} (R_1 + R_t + R_r) \oplus \right] \quad (3)$$

$$\oplus C_2 \left[\Omega_c t + \frac{2\pi}{\lambda_c} (R_2 + R_t + R_r) \right]$$

4. Matrix presentation of SC-MRN codes

Bearing in mind the equations (1-3) it is possible to represent the U-PN codes phases of a SC-MRN, based on N primary sources, in matrix form as follows:

- **U-PN code** in the transmitter site:

$$[U - PN_{transmitter}] = \begin{bmatrix} \frac{2\pi}{\lambda_c} \times R_1 \\ \frac{2\pi}{\lambda_c} \times R_2 \\ \dots \\ \frac{2\pi}{\lambda_c} \times R_n \end{bmatrix} \quad (4)$$

- **U-PN code** of the synchronization link in the receiver site :

$$[U - PN_{receiver}^{synchronization}] = \begin{bmatrix} \frac{2\pi}{\lambda_c} \times (R_1 + R_d) \\ \frac{2\pi}{\lambda_c} \times (R_2 + R_d) \\ \dots \\ \frac{2\pi}{\lambda_c} \times (R_N + R_d) \end{bmatrix} \quad (5)$$

- **U-PN code** of the target reflected wave in the receiver site :

$$[U - PN_{receiver}^{target-reflected}] = \begin{bmatrix} \frac{2\pi}{\lambda_c} \times (R_1 + R_t + R_r) \\ \frac{2\pi}{\lambda_c} \times (R_2 + R_t + R_r) \\ \dots \\ \frac{2\pi}{\lambda_c} \times (R_N + R_t + R_r) \end{bmatrix} \quad (6)$$

4. SC-MRN based on global navigation system GPS

An attractive application of the SC-CDMA technology is the use of the satellites of the global positioning system GPS as sources of the PN-modulated signals. In this particular case the U-PN code is **mod2 sum** of the recovered in the transmitter site GPS receiver C/A codes of the visible satellites. Because of the very fast relative satellite motion the created in this case U-PN code changes very fast – it looks like a pure random signal. U-PN code acquisition and tracking is based on the exchanged between transmitter site and receiver site information about their positions in ECEF geographic coordinate system, used by GPS.

5. Conclusions

A new approach for pseudo-noise code generation and synchronization, suitable for mobile multistatic radar networks, is proposed in the report.

The basic SC-CDMA geometry of a particular mobile multistatic radar system, as well as mathematical description of the proposed method of code generation and synchronization are explained in details. A proposal for a real system, using the satellites of the global positioning system GPS as sources of the pseudo-noise signals, is given too.

The implementation of the proposed new SC-MRN approach for PN – code generation and synchronization will give new chance of the future sophisticated mobile defense radar systems.

References

- [1] N. J. Willis, *Bistatic Radar*. Artech House, Boston, 1991.
- [2] B. Mahafza, "*Radar Systems Analysis and Design using MATLAB*", HAPMAN& HALL/CRC, 2000.
- [3] V. Demirev, "Space Correlated (SC) CDMA - New Way for Effective Radiofrequency Spectrum Utilisation of Mobile Communications", in *Proc. Telecom, 99*, Varna, 1999 (in bulgarian).
- [4] V. Demirev, T. Tchanev, "EMI A&B - SC CDMA Radiointerface for Mobile Communications", in *Proc. Telecom, 99*, Varna, 1999 (in bulgarian).

ALGORITHMS FOR MANAGEMENT AND CONTROL OF SYSTEM FOR THERAPY BY „RANDOM” RUNNING LOW FREQUENCY MAGNETIC FIELD

Atanas Dimitrov Dimitrov

Technical University of Sofia, Bulgaria,
Faculty of Telecommunication, TU-Sofia, “Kl.Ohridsky” str. 8, 1000 Sofia, Bulgaria,
E-mail: atanas.dimitrov@best.eu.org

Abstract

It is well known that current systems for physical therapy most often are with microprocessor control. The new systems for therapy by “running” low frequency magnetic field are no exception. The big advantage of the microprocessor is that it provides a realization of multiple logic blocks, without using additional external components. Realization of the same number of blocks by using discrete elements increases instability and failure in the operation process of the apparatus. Also, the complexity, volume and price of the device would increase a lot. The article deals with specific algorithms for the management and control of operating modes of the magnet system with low-frequency magnetic field.

1. Introduction

As control unit of system for magneto-therapy by a “running” low frequency magnetic field can be implemented microcomputer PIC18F452 connected to external passive components of the system. The basic task of the control unit is management of action mode of blocks connected to it, namely:

- Block external control Unit;
- Unit for output signal commutation;
- Unit for amplitude control;
- Generating unit

The main program is an endless cycle. Its purpose is to monitor whether there is an attempt to influence and change the status of the processor by the user. Block diagram of the initialization and main subprogram is shown Fig. 1. With each initial application of voltage to the microprocessor following subroutines are called.

- 1. Reset the timer counting down the time to generate a periodic pulse train
- 2. Read inputs
- 3. Starting

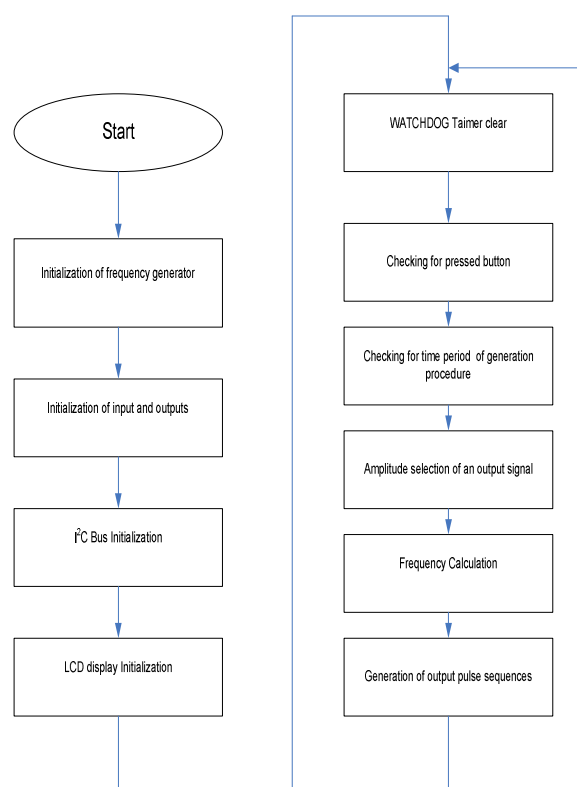


Fig. 1. Block diagram of the initialization and main subprogram

When supply voltage is applied to the microcomputer initialization function is proceed. The aim is to set the starting conditions to be taken into consideration in implementing the main subprogram. Proper operation of the device requires to define Input/Output ports in accordance with the principle scheme of the apparatus. To ensure control of the operation by the user are provided for 4 buttons. Their defining feature requires 4 pins in the microprocessor program as inputs.

2. Basic algorithms

On each cycle of the main subprogram four inputs of the microprocessor are checked. Logic program can be divided into 5 main units. External control unit consists of four irretentive buttons submitting input to four input terminals defined by the microprocessor. Each button has a defined function in execution of the main program.

Pressing a button means logical 0 for the processor and subprogram is called

Unit for commutation of the output consists of five outputs of the microprocessor.

Block switching voltage output consists of six outputs. They are used for determination of the amplitudes of output signals.

Monitoring of output parameters of system and providing feedback from the user is done through visualization unit. It provides appropriate information, which is displayed on the LCD display as understandable text to the user.

The generation unit is implemented by configuring Taimer0 the micro-processor to generate a certain frequency at a specific point in time.

After successful initialization of the microcontroller LCD display shows a message to indicate that the microprocessor is in waiting mode. If button's state change has occurred a subprogram is called. Algorithm for button checking is shown in Figure 2. In order to eliminate mechanical noises buttons have to be rechecked after short period of time.

Button names depend from their functionality. Their names are:

(Start, Enter) -start the procedure for generation series of periodic impulses; confirmation of the choice of the parameters set by the user; continuation of the current procedure.

(Stop, Set) – call the program menu; checking the set of parameters of microprocessor; suspension procedure for generating pulse sequences; induce a pause in the procedure.

(Up) – increasing values of different signal when entering the program menu;switching from automatic to manual mode frequency change;increasing frequency in manual mode;preview imprint.

(Down) – reducing the values of various signal's parameters of entry to the program menu; switching from automatic to manual mode frequency change; reducing the frequency in manual mode; preview imprint.

The function of button **(Start/Enter)** in primary placing on the device can be described by the algorithm shown in Fig. 3. The button serves to start the sub-routine for generating pulses at certain intervals. Pressing the button a message appears on the display, which shows the user that the application is accepted by the microprocessor and will execute the selected subprogram. It is called as soon as they found a change of state of the signal.

This is done to avoid repeatedly calling the subrou-tine in the case when the user holds too long pressed a button.

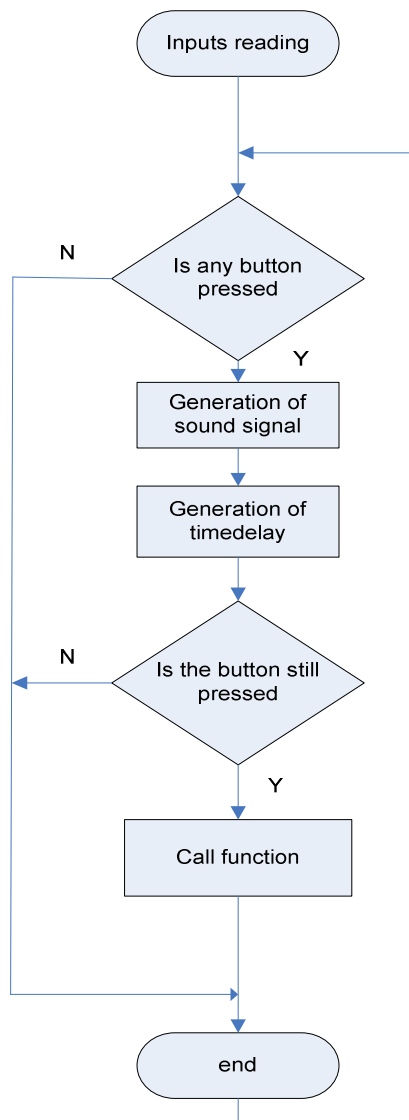


Fig. 2. Algorithm for button checking

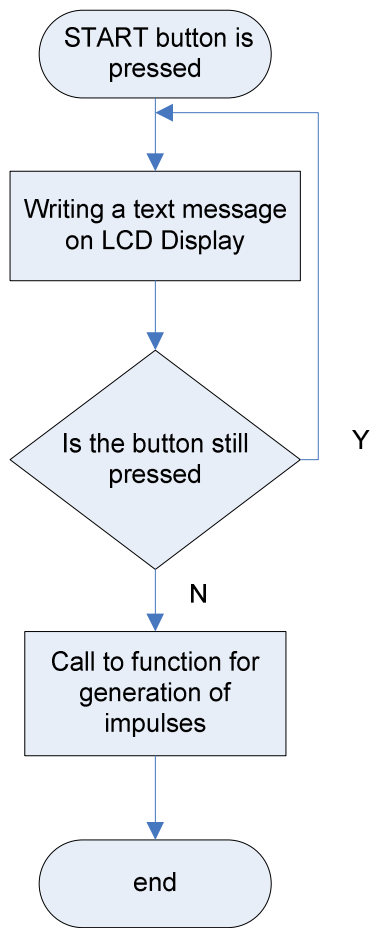


Fig. 3. Algorithm of work of the button Start / Enter

Button (Stop/Set) is set to enter the menu and to view parameters set of generated output signals of the microprocessor. Pressing it microprocessor go in a cycle that consistently reviewed and adjusted as necessary parameters of the generated signals and modes of the generator. Its function can be described by a functional algorithm shown in fig.4. Pressing the SET button first displays the current setting of a parameter of the output signal. In the case that the user wishes to change it can enter into a separate submenu and make the desired correction. To save changes it is necessary to press again the button SET.

Pressing the SET button will show the next value of the parameter signals and will give the possibility for changing. From the menu it is possible to go only when consistently review all the possible parameters for the output device signals. After first pressing of SET the first parameter of the output signals is called. This is the maximum operating frequency of the signals. At this point, the microprocessor monitors which button is selected by the user. Pressing the START button call a function for setting the operating maximal frequency.

If now the SET button pressed again is displayed information about the next parameter signals. This is the duty cycle of the generated pulses. The next parameter that has the potential to change duration set to generate periodic pulse train output of the device. The next parameter that has the potential to change duration set to generate periodic pulse sequence at the output of system. The last parameter determines amplitude and operation mode. The change of the amplitude of the output signal can be set thanks to service subprogram.

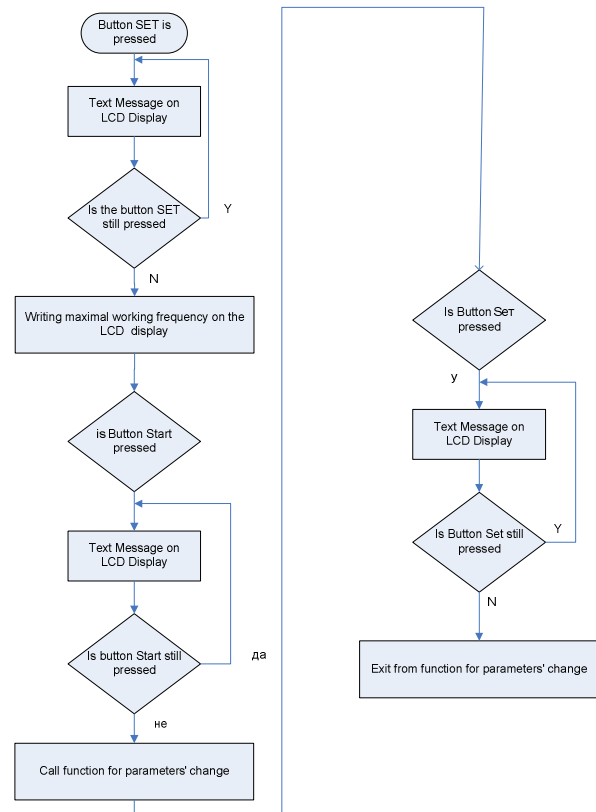


Fig. 4. Algorithm of the functions are a button Stop / Set

This amplitude can be changed automatically during the process of therapy or to be fixed precisely. The sequence of the crawl parameters in implementing software menu is shown in Fig. 5.

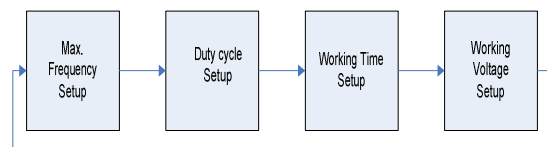


Fig. 5. Algorithm for sequence of parameters setup

Buttons up/down is used only to increase or decrease the values of selected parameter to change the camera output signals. Algorithm of the action buttons UP/Down is shown on Figure 6.

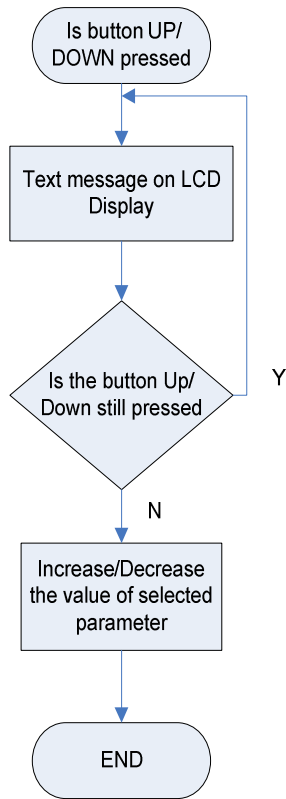


Fig. 6. Algorithm of the action buttons UP / Down

The main subroutine is divided into several sub-divided according to their purpose. By Sub Setup () is implemented for menu browsing and setup parameters of the output signals of the system.

Algorithm of work on the main subprogram is shown in Fig. 7. To achieve feedback from the user and easy monitoring of the operating mode of the microprocessor function is done using an infinite loop.

Therefore the microprocessor always waits intervention by the user before an operation. In primary set automatic mode switching for the amplitude of the output signals of each device to switch from maximum to minimum frequency is automatically switched the amplitude of the output.

Switching amplitude as a function of time is shown fig. 8. Manually change the frequency can be done by pressing the Up or Down buttons. The time remaining until the end of the procedure is kept in memory of the processor and then return back in the automatic mode continues to check the time remaining. In manual mode the user can increase the frequency of pulses generated by pressing Up, a Down button to reduce it. Switching back in the automatic mode is performed after pressing Start.

The procedure for generating pulses continues until the time specified by the user time to generate or not a button is pressed Stop.

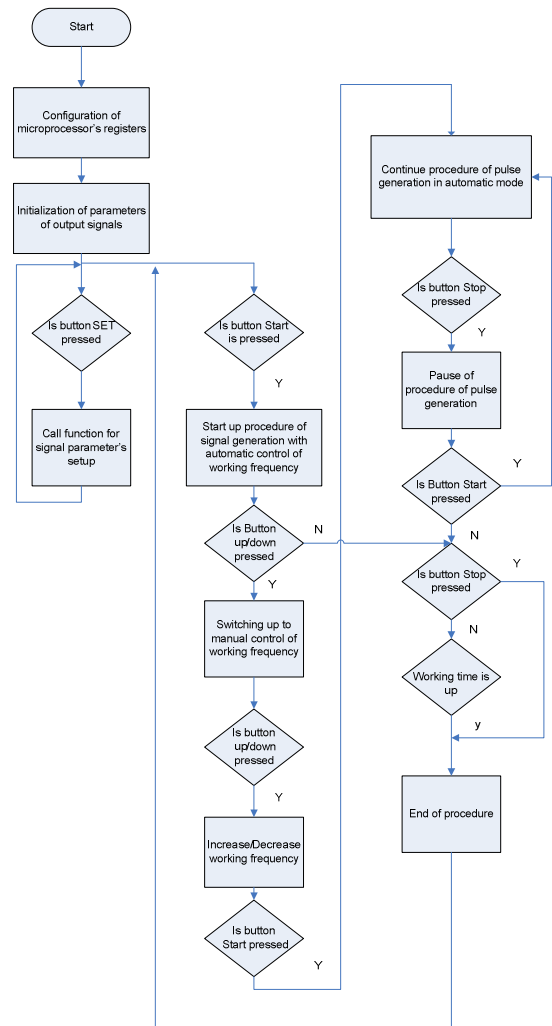


Fig. 7. Algorithm of work on the main subprogram

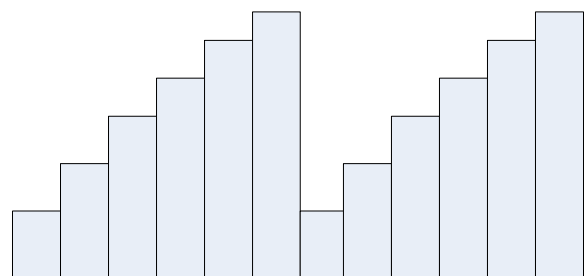


Fig. 8. Switching amplitude as a function of time

Registering Stop button pressed puts the CPU in the Pause mode. This situation generates an audible signal and the microprocessor expected after pressing the start button or stop. The values of the current frequency modes remaining and time saved. Pressing the start button to continue the program execution the place where he stopped, and when pressing the procedure is terminated.

The process of generation of pulse sequences with automatic changing of frequency is shown fig. 9.

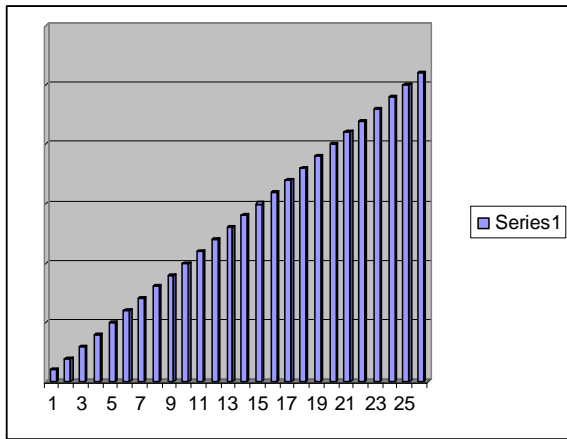


Fig. 9. Process of generation of pulse sequences with automatic changing of frequency

The display shows the raw data for signals that will start to generate. Write out information about the operating voltage, duty cycle of the output magnetic signals generated current frequency and timing of generation of pulse sequences. After initialization process starts the process of generating pulses from the microprocessor. When the highest frequency is reached, it is automatically switches back to the lowest. Any such transition is related to increased unit with a variable voltage to determine what is fed to the outputs of the device. After reaching the maximum frequency used for all terminals controlling the output voltage is reset. Termination of the procedure for generating pulses occurs when it detects a double interference by the user or if the time set for the procedure of generations has elapsed. To inform the user that the procedure generated pulses ended short message is displayed on the display. CPU returns to waiting mode output, which monitors the re-intervention by the user.

Algorithm on fig. 10 shows the process of generating a certain periodical time series of rectangular pulses automatically changing frequency and amplitude modulation of automatic.

3. Conclusion

The main goal of this paper is to present a basic algorithms for management and control of system for therapy by "running" low frequency magnetic field. These algorithms provided a high level of flexibility not only for above mentioned system for magneto-therapy, but for other different microprocessor systems for physiotherapy. The changing of different modes of therapy is very friendly. Nevertheless the system can provide many modes of

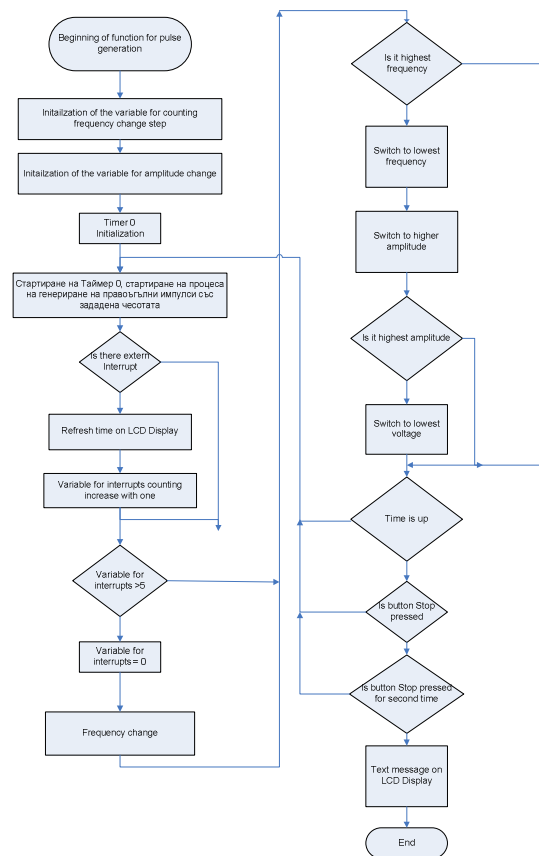


Fig. 10. Algorithm of process of generating a certain periodical time series of rectangular impulses

therapy. Some of them can be very complicated. In fact the number of modes of therapy provided by this kind of system is not limited. The assurance of described system, which is provided by algorithms for CPU is another very important advantage.

References

- [1] SIEMENS Medical Engineering Group, "Units for Physical Therapy And Diagnosis". p.230, 2002
- [2] W. Y. Riadh, "Electromagnetic Fields and Radiation (Human Bioeffects and Safety)", Marcel Dekker Inc. Canada, 2001, ISBN 0-8247-0877-3.
- [3] Д. Димитров, Медицински системи за въздействие на електромагнитно поле върху човека, учебник, издателство на ТУ-София, 2007
- [4] V. Mihaylov, Kalin L. Dimitrov, Dimitar C. Dimitrov, Research on the influence of permanent magnetic field during live tissue laser treatment, 3rd International Conference "Communication, Electromagnetism and Medical Application, Athens, Greece, November 6-8, 2008, p.12-156
- [5] Д. Димитров, Комуникационни системи в медицината, учебник, издателство на ТУ-София, 2005

METHOD FOR DESIGN OF SYSTEM FOR THERAPY USING „RANDOM” RUNNING LOW FREQUENCY MAGNETIC FIELD

Atanas Dimitrov Dimitrov

Technical University of Sofia, Bulgaria,
Faculty of Telecommunication, TU-Sofia, “Kl. Ohridsky” str. 8, 1000 Sofia, Bulgaria
E-mail: atanas.dimitrov@best.eu.org

Abstract

The systems for magnetotherapy, which use “running” low frequency magnetic field, are new generation of systems for magneto therapy. It is well known that familiarization of patients with parameters of external influence is a big disadvantage of systems for physiotherapy. This problem can be avoided with systems for low frequency magnetic field by moving the magnetic field around the human body. The possibility for simultaneously influence of “running” low frequency magnetic field on different part of the human body is one additional advantage of systems for magneto therapy. The basic requirements and method for design of above mentioned system for magneto therapy is described in the paper.

1. Introduction

The main component of the systems for magneto therapy using low frequency magnetic field is digital controlled generator for rectangular electrical impulses with special parameters.

The use of digital elements with programmable logic offers greater flexibility, economy and more functions in one system. The data which pass through various digital modules can be saved in memory, subject to various digital processing, and also can be displayed on digital display. In the design of pulse generators can be used and one-chip microcomputers, characterized by low consumption and a limited number of external components. Programmable logic of one-chip generators is a great advantage over the basic generators. Any functional change can be implemented easily without any hardware changes (making a new board, adding/replacing components).

2. Theoretical solution of the system for magneto therapy by therapy “running magnetic field”

The system for low frequency magneto therapy with the “running wave”, the subject of this paper is achieved through a successful combination of analog and digital elements. Digital control of the system is implemented thanks programmable microcontroller.

The output impulses from the microcontroller are close to perfect rectangular signals with extremely short falling and rising edges. This allows easy and extremely precise control of analog components connected to the microcontroller, and accurate control of output signals for the system. The block diagram of the system for magneto therapy by a “running” low frequency magnetic field is shown in Figure 1.

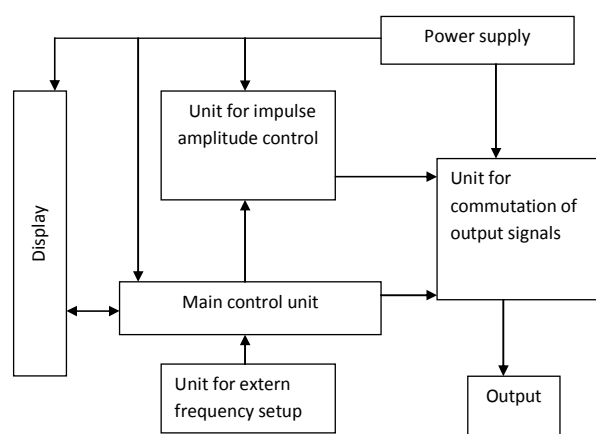


Fig. 1. Block-diagram of systems for magneto therapy with “running” magnetic field

There are seven functional blocks. Principle of operation of each of them will be discussed in details below. Working modes of therapy system can be described as follows: The output of the Main control

unit generates series of rectangular digital impulses to the Unit for commutation of the output signals. Amplitude of the output signals of the systems is determined by the Unit for amplitude control. External user control of the working frequency is possible thanks to Unit for external frequency control. There are also liquid crystal displays for visualization of the parameters of output pulses for the system in real time.

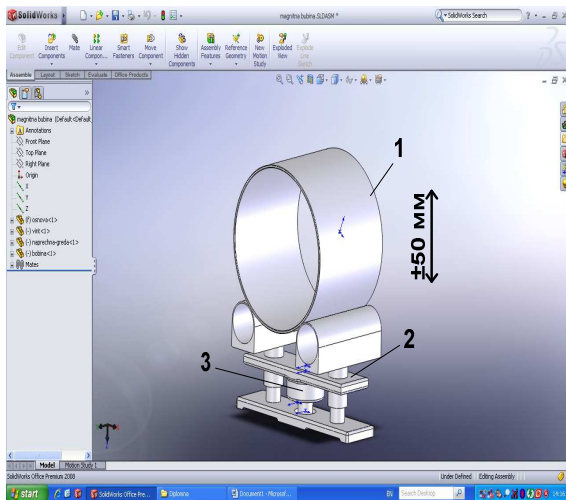


Fig. 2. Apparatus for magneto therapy with one girdle coil

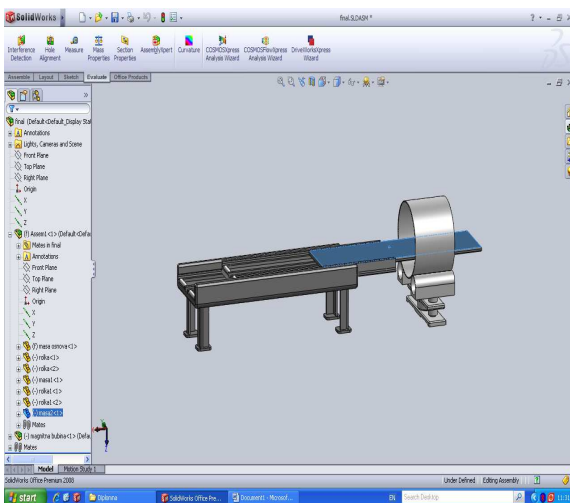


Fig. 3. Apparatus for magneto therapy with one girdle coil put on bed

This system can be build as apparatus for magneto therapy which outputs are connected with one girdle coil (Fig. 2). The girdle coil can be put on the bed for magneto therapy (Fig. 3)

3. Basic components of system for magneto therapy by "running magnetic field"

Main Control unit:

The main control unit is the most important part of the system and has to and control the working modes and to analyze signals form the "Unit for amplitude control block", "Unit for commutation output signals", "Unit for extern frequency setup". This block is responsible for: the time for generating periodic pulses, the maximum operating frequency, amplitude and rate of filling of the system output signals. The change the operating mode of this module is possible by detecting the signals coming from "Unit for external frequency setup".

The main control unit is based on programmable microprocessor, with uploaded suitable firmware on it.

Real-time monitoring of the status of the different working modes of the system is possible thanks to installed digital liquid crystal display.

Created software for the processor allows generation of different time delays, syntheses of impulses with different frequencies control and analyses of different input/output signals. Mainly system processor use one byte instructions performed by a single instruction cycle. Exceptions are cases where there is a condition for branching in the program or the changes of the program counter. In this situation, execution takes two instruction cycles, the second run by NOP /no operation/. Two-byte instructions are performed in two cycles; one cycle consists of four periods of the oscillator. Time for one command at frequency of 20MHz clock generator is equal to 0.2us. In case of branching in the program or when the program counter is changed as a result of the instructions, the time needed for implementation will be 0.4us. Therefore making delays of 1 ms is necessary to make 5000 cycles in the microprocessor. The frequency of pulses at the terminals of microcomputer specified and outputs can be easily changed by appropriate subroutine. Manually changing the frequency via external buttons is also possible.

Providing this type of user control requires constant monitoring of button status.

One algorithm for implementation of this functional is shown on fig. 4.

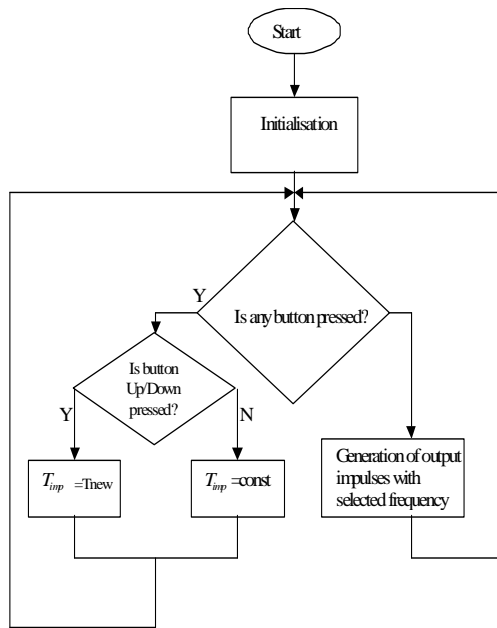


Fig. 4. Algorithm for button's monitoring

The unit generates series of impulses when upload certain values to internal timer and counts up the amount of timer's overflows. Time-delays that occurs as a result of counting corresponds to the period of desirable pulse frequency. In the begging of instructions counting all outputs are cleared.

An example functional diagram of pulse generator realized with single-chip microcomputer is shown on Fig. 5.

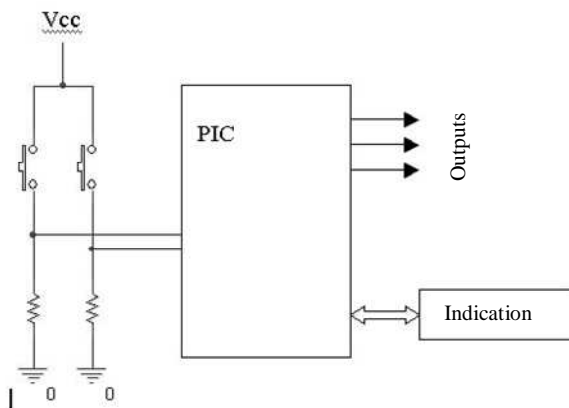


Fig. 5. An example functional diagram of pulse generator realized with single-chip

With two buttons, the user can adjust the working frequency of the device.

The outputs of the microcomputer are connected to the other functional units to provide control over the different working voltages and systems outputs.

This is necessary because the outputs of the circuit can not provide the required output power. Real time feedback to the user is possible thanks to liquid

crystal (LCD) which is also connected to the microprocessor. Thus it is possible to monitor the current frequency and amplitude of the output device.

Unit for external frequency control

This block allows to the user to select appropriate working frequency. By pressing the buttons and text messages on the LCD display the frequency can be easily selected from the user.

Block switching output

This unit carried out and successively shift the generated impulse to one of the device's output. Switching signal as a "running wave" is done automatically using appropriate software solution. Principle of action can be explained by the fact that continuous time monitor which output is a logical unit. When an output is high level, all others are low. For the realization of a series of impulses running "running wave" the duty cycle of pulses depends inversely on the number of outputs.

Unit for amplitude control

Thanks to this unit it is possible to perform manipulation of amplitude output signal of the device. The unit provides precise control of amplitude of output signal for the system.

Output unit

The unit represents the synthesized output interface system. It consists of appropriately selected connector box mounted to the apparatus. It provides smooth and reliable interface between the device and external to the system inductive load.

Liquid-crystal display

It allows monitoring of pulse parameters and system feedback. Visualization of the computer is deliberately avoided, because in this case functions will be limited in the absence of a computer connected to projection device. Seven segment displays is a good choice because of the need to use a large number of terminals to display a symbol. The ability to simultaneously monitor multiple parameters using a small number of connection wires and low power consumption makes LCD-display as the most appropriate choice for system parameters visualizations.

Power supply Unit

The power supply consists of a special transformer for medical equipment and a group of voltage straightening, maximum filtration and stabilization of

the interference with the mains voltage. The main task of the unit is to ensure proper working voltage to all electronic components of the system. Input/output signals used for communication between management and individual blocks are:

- Power supply should work with the input output voltage $\sim 220\text{V}/50\text{ Hz}$. Voltages of secondary windings usually must be 60, 80, 110 V AC.
- The output of power supply usually must be stable voltages +12 and +5 V.

After identification of the signals is done processing and software programming decision-making.

Field"

- Communication between the liquid crystal display and microcomputer is done by data bus. It consists of a 4-bit data channel signal and 2 service configuration.

4. A real system for magneto-therapy with "running magnetic field"

System therapy "running magnetic field" is synthesized by the successful combination of analog and digital components and appropriate software. The successful combination of analog power components with micro-electronic integrated circuits offers a modern and easy way to precisely control, monitor and generate low-frequency analog signals with high power. Main advantage of using such a combination consists of low power consumption and relatively simple hardware solution. Similar systems with traveling wave therapy in the manner described can be easily implemented in portable cases. That is makes the system convenient and easy to use.

A real system for magneto therapy for "running magnetic field" can be seen on Fig. 6. The outputs of apparatus for magneto therapy are connected with five independent coils.

The output impulses of the independents coils can be seen on Fig. 7.

5. Conclusion

1. A method and basic requirements for design of systems for magneto therapy by running low frequency magnetic field are described in the paper.
2. A real system for magneto therapy by running low frequency magnetic field is done, also.



Fig. 6. System for magneto-therapy with "running magnetic field"

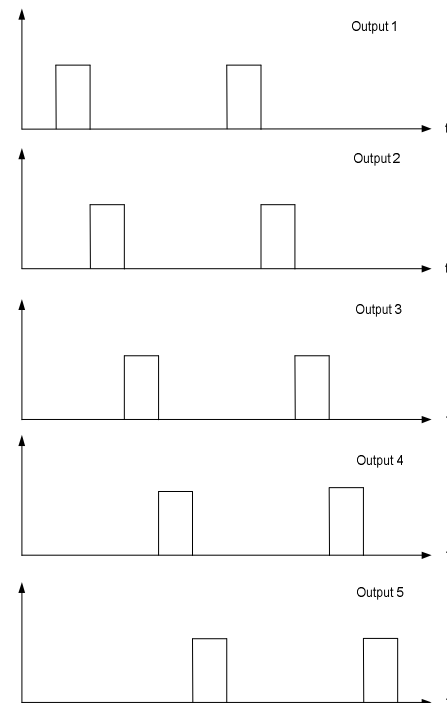


Fig. 7. Output impulses of the independents coils

References

- [1] "Електротехника и Електроника", списание на съюза по електроника, електротехника и съобщения, София, януари/февруари 2002.
- [2] К. Конов, М. Димитрова, А. Попов, Импулсни схеми, Техника, 1984.
- [3] Microchip Datasheet PIC18F452
- [4] Philips Datasheet PCF8583
- [5] SHENZHEN JINGHUA DISPLAYS CO., LTD., LCD AC162A
- [6] Н. Стефанов, Токоизправители и стабилизатори, София, Техника, 1981.
- [7] Fairchild Semiconductor Corporation, Datasheet MJE340.

INFLUENCE AND IMAGE OF THE MICROWAVE ELECTROMAGNETIC FIELD IN THE LIVING TISSUES IN THE HUMAN BODY

Antoniya Petrova Petrova

Technical University of Sofia, Bulgaria
Faculty of Telecommunication, TU-Sofia, "Kl. Ohridsky" str. 8, 1000 Sofia, Bulgaria
E-mail: tony.petrova@gmail.com

Abstract

Effects of electromagnetic fields on living cells depend on the frequency. The purpose of this article is to show the influence of the microwaves and in particular the wave of the decimetre range beyond the human. The performed studies showed that more effective treatment we have, when the frequencies are very high in the range of 2-3 GHz. These frequencies and wavelengths are the most efficient and allowing for much deeper action and better controllability of intensity of the warming. Electromagnetic waves of this range are well defined optical properties and can guide and reflect. Studies were made with dipole antennas with hemispherical or semi-cylindrical reflectors of different sizes and in various locations. The achieved results are applied to observed the penetration of microwave electromagnetic fields in our body and its positive impact on the treatment of certain diseases.

1. Introduction

In microwave therapy, the patient is set in electromagnetic fields with frequencies a few GHz, which means that the wavelength is from 10 to 70 cm. The energy of microwaves, absorbed from the body tissues, is converted into heat, significantly more effective than the energy of longer wavelengths.

During the action of the variable electric field on the dielectric, the sign of polarization and orientation of the dipole, changing with the frequency of change of the sign on the field. At the high frequencies of electrical field, the polarizing molecules fail completely to change their spatial orientation and occur vibrations of the dipoles around neutral position. This process is associated with generate the heat.

2. Theoretical solution

At the frequencies above 500 kHz, the irritation of the current became so weak, that the patient can't feel anything. The electromagnetic oscillations with high frequencies are used for heating of living tissue

by converting the electromagnetic energy of high frequency current or high frequency field in the heat. In these high frequencies, the currents even up to several amps do not cause irritation. Characteristic is that the heat is produced inside the body itself, where the applied energy is converted into thermal energy (heat endogenous), but the distribution of energy in the various methods is not uniform. By increasing the frequency of the alternating current is reduced the time to move of ions in one direction, consequently fewer ions accumulate at the border semi-permeable cell membranes and reduces irritation. At frequencies above 500 kHz do not get enough concentration of ions to be induced excitation. Even at these frequencies, the ions vibrate around a midpoint. Since there is no irritant effect, the current can be increased until we get a heat. The quantity of heat released from various tissues is inversely proportional to the conductivity of tissues.

Furthermore, since there is no irritant, this allowed larger current densities under the electrodes, thus reduces the contact resistance between electrode and skin. Table 1 gives the specific resistance of the major tissues of the body at frequencies in the range of 2-3 GHz. [2]

Tissue	Frequency in range 2-3 GHz
Blood	0,65
Muscles	0,49
Internal Organs	0,4 - 0,8
Nerve Tissues	0,4 - 0,9
Fatty Tissues	8 -30

Table 1. Specific electrical resistance of the tissues in the human body

The heat q , release per unit time, per unit volume of homogeneous tissue for passing of high currents is:

$$q = k \frac{\Delta^2}{\sigma}$$

where: Δ – current density;
 k – coefficient of proportionality;
 σ – specific conductivity of the tissue through which currents passing.

The separated heat is determined by the geometrical parameters of the electrodes, how they were placed against the body, but the frequency, the electrical conductivity of tissues and their dielectric properties. Therefore, different tissues in specific for their frequencies will receive the maximum amount of heat.

The energy absorption of microwaves from the tissues of living tissues and converting it into heat shall result in energy losses in ion conduction and dielectric losses, associated with relaxation oscillations of the dipoles. The absorption of the ion conductivity does not depend on frequency in the range of microwaves.

The intensity of the microwaves as they pass through the environment, which absorbs reduces to an exponential law. The depth at which the intensity decreases called absorption half - width h . [1]

$$\frac{1}{2}J(0) = J(0)\exp(-\alpha h),$$

Where:

$J(0)$ – the intensity of surface ($x = 0$).
 α – absorption coefficient.

Absorption half - width is determined by the expression:

$$h = \frac{\ln 2}{\alpha}$$

We estimated that if we have wavelength 12 cm, absorption half – width will be 0,9 cm.

Upon irradiation of homogeneous tissues, the heat is distributed in depth by an exponential law. When they are exposed to microwave, the layers of different tissues obtained reflection from boundary surfaces, when the permittivity of the layers is different. This phenomenon changed the distribution of energy absorbed and deep heating of tissues. On the boundary surfaces between the layers of the different tissues, temperature peaks are obtained.

3. Basic components of the microwave therapy and irradiation of the different reflectors

The impact of the microwaves of a human's body can be achieved through dipole antennas with hemispherical or semi-cylindrical reflectors. They can be seen on Figure 1.



Figure 1. Different reflectors

Reflectors are placed directly on the area, which has to be heated, or at some distance from it. Reflectors can be closer or further away, so they can adjust their distance to the skin, which must be 2-10 cm.

Figure 2 shows the microwave apparatus and its application (Figure 3).



Figure 2. Device for microwave therapy



Figure 3. Applied to the patient

4. Microwave therapies and the positive influence of them

One of the main and not quite resolved issues, in microwave therapy is the determination of energy, which is absorbed by the object. It was made a lot of researches, which showing that ultra-high frequency waves with a wavelength of 69 cm, i.e. the frequency is 433,92 MHz, are the most perspective. These waves have similar physiological action with the other high frequencies currents, but they penetrate to greater depths. The differences relate to absorption of electromagnetic energy and its distribution in different tissues. They have the least thermal effect of fat tissues, but their energy is distributed more evenly in tissues. Recently, ultra-high frequency waves have a good therapeutic effect in: transient disorders of cerebral circulation, stroke, vascular incidents in the central nervous system, chronic arterial insufficiency of lower extremities. Improves microcirculation, rheological properties of blood, detection of shunting, increased cell permeability. The conclusion is that the ultra-high frequency waves have a beneficial effect on the functional status of heart. Improves tissue oxygen saturation and metabolic processes in cells.

In medicine is mainly used microwaves with wavelength 12.2 cm, 12.4 cm and 12.6 cm which are on the border with UHF. In practice, apparatus are used primarily, generating capacity to 200 W at 2450 MHz operating frequency, i.e. the wavelength is 12.2 cm.

The duration of procedures depends on the dosage, but they are weak - 0,36 W/cm², average - 0,56 W/cm² and strong - 1,5 W/cm². The duration of the procedures is from 5 to 10-20 min. In acute and sub-acute inflammatory processes are used weak

doses. These doses are recommended and low exposure areas vascularised or near such (ovaries, eyes). Irrespective of different coefficients of reflection of the individual tissues, centimeter waves are absorbed significantly (40-75%). They are penetrated to a depth of 5-6 cm. The next Figure 4 shows the distribution of heat in the UHF and microwaves in various tissues.

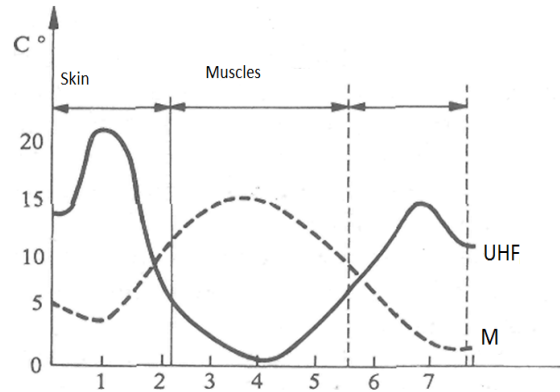


Figure 4. The difference between UHF and microwaves

The different design of reflectors for directing of the microwaves amended distribution of heat. Figure 5 shows the distribution of heat, perpendicular to the axis of irradiation with hemispherical (Figure 5a) and semi-cylindrical reflector (Figure 5b).

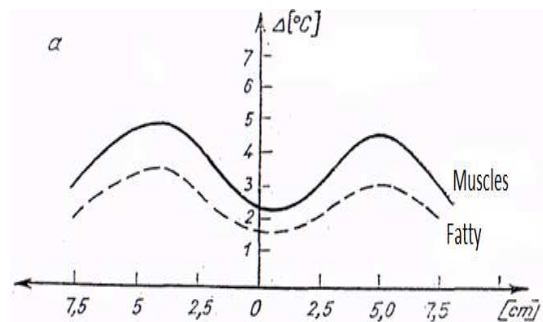


Figure 5a. Irradiation with hemispherical reflector

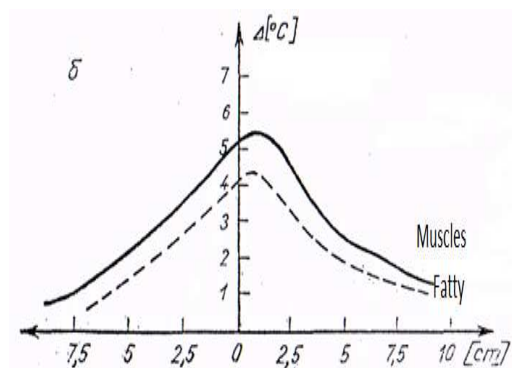


Figure 5b. Irradiation with semi-cylindrical reflector

Figure 6 is shown schematically, the extent of absorption of electromagnetic energy of the electromagnetic energy in our body depth with different methods of high-heat treatment. Observe that the capacitor field, where the wavelength is 11,12 cm (Figure 6a) heating occurs deeper underlying tissues. In inductive heating electrode receives the muscles (Figure 6b). The same distribution is observed and with longer decimeter waves, where the wavelength is 69 cm, it can be seen in the Figure 6d. The scope of ultra-high frequency waves, the longer waves have greater depth effect of the shorter (Figure 6c). In ultra-high frequency waves through the radiator, representing a symmetric vibrator and reflector, achieves much higher warming of the deeper tissues (Figure 6e). [5]

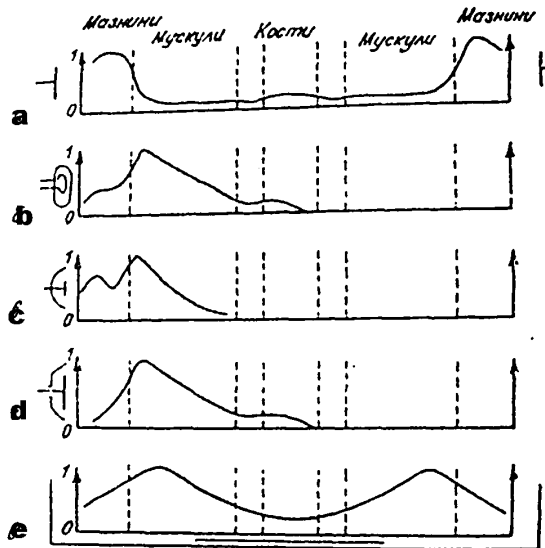


Figure 6. The extent of absorption of electromagnetic energy of the electromagnetic energy in our body depth with different methods of high-heat treatment.

Skin and subcutis absorbs less microwave energy, allowing to penetrate without much loss to the muscles and the blood tissue, unlike the electromagnetic waves used in the UHF field. Microwaves at low doses appear to be particularly beneficial on vascular permeability in inflammation and allergic conditions. They also raise redox processes in the tissues. In small doses increases the protein content and phosphorylase activity in skeletal muscle.

5. Conclusion

1. Describes the change of the field from the location and the different size of reflector and heat generation in the body.

2. Positive effect of the microwave therapies in our bodies

References

- [1] D. Dimitrov, Medical systems influence of electromagnetic fields on human, education book, TU-Sofia, 2007
- [2] W. Y. Riadh, "Electromagnetic Fields and Radiation (Human Bioeffects and Safety)", Marcel Dekker Inc. Canada, 2001, ISBN 0-8247-0877-3
- [3] Shoogo Ueno, Biological Effects Of Magnetic And Electromagnetic Fields (The Language Of Science)
- [4] Internet: <http://medeos.com>
- [5] Schwan, H. P., Interaction of Microwave and Radio Frequency Radiation with Biological Systems, IEEE Transactions on Microwave Theory and Techniques 10, 2001

INFLUENCE AND IMAGE OF THE UHF ELECTROMAGNETIC FIELD IN THE LIVING TISSUES IN THE HUMAN BODY

Antoniya Petrova

*Technical University of Sofia, Bulgaria
Faculty of Telecommunication, TU-Sofia, "Kl.Ohridsky" str. 8, 1000 Sofia, Bulgaria
E-mail: tony.petrova@gmail.com*

Abstract

The aim of this paper is to visualize the influence of ultra high frequency electric field and in particular the wave of meter range beyond the human. Effects of electromagnetic fields on living cells depend on the frequency. The researches and the results are made at frequencies in the range of 20-30 MHz, because in the therapy with ultra-high frequencies, these frequencies and wavelengths are the most efficient and allowing for much deeper action and better controllability of intensity of the warming. In this way, we are receiving more effective treatment beyond the patient. During the researches are used two different electrodes - capacitive and inductive, with different sizes, different placement of the electrodes and a visualization of the lines of force on the field to the placement and the size. The achieved results are applied to observed the penetration of high-frequency electromagnetic fields in our body and its positive impact on the treatment of certain diseases.

1. Introduction

In medicine, the therapy in this range is known as UHF-therapy. During the action of the variable electric field on the dielectric, the sign of polarization and orientation of the dipole, changing with the frequency of change of the sign on the field. At the high frequencies of electrical field, the polarizing molecules fail completely to change their spatial orientation and occur vibrations of the dipoles around neutral position. This process is associated with generate the heat.

2. Theoretical solution

At the frequencies above 500 kHz, the irritation of the current became so weak, that the patient can't feel anything. The electromagnetic oscillations with high frequencies are used for heating of living tissue by converting the electromagnetic energy of high frequency current or high frequency field in the heat. In these high frequencies, the currents even up to several amps do not cause irritation. Charac-

teristic is that the heat is produced inside the body itself, where the applied energy is converted into thermal energy (heat endogenous), but the distribution of energy in the various methods is not uniform. By increasing the frequency of the alternating current is reduced the time to move of ions in one direction, consequently fewer ions accumulate at the border semi-permeable cell membranes and reduce irritation. At frequencies above 500 kHz do not get enough concentration of ions to be induced excitation. Even at these frequencies, the ions vibrate around a midpoint. Since there is no irritant effect, the current can be increased until we get a heat. The quantity of heat released from various tissues is inversely proportional to the conductivity of tissues.

Physiological and therapeutic effects of ultra high currents differs substantially from that of low frequency currents, virtually absent the process of electrolysis and electrophoresis, and tissue penetration is bigger. Ultra high currents in living tissue has two components: current conduction (through the tissues and fluids of the body with good conductivity) and flow of the mixture (in tissue dielectrics). The formation is endogenous heat the most important role played the active resistance in current conduction. Active resistance of the body for high frequency current is significantly less than in the direct current. This is explained by the absence of currents caused by polarization phenomena as in the electrodes and the body. Furthermore, since there is no irritant, this allowed larger current densities under the electrodes, thus reduces the contact resistance between electrode and skin. Table 1 gives the specific resistance of the major tissues of the body at frequencies in the range of 20-30 MHz. [2]

Specific Electrical Resistance of the tissues [$\Omega.m$]	
<i>Tissue</i>	<i>Frequency in range 20-30 MHz</i>
Blood	1
Muscles	1,65
Internal Organs	2 - 3
Nerve Tissues	8 - 10
Fatty Tissues	20-50

Table 1. Specific electrical resistance of the tissues in the human body

The heat q , release per unit time, per unit volume of homogeneous tissue for passing of high currents is:

$$q = k \frac{\Delta^2}{\sigma}$$

where: Δ - current density;
 k - coefficient of proportionality;
 σ – specific conductivity of the tissue through which currents passing.

The separated heat is determined by the geometrical parameters of the electrodes, how they were placed against the body, but the frequency, the electrical conductivity of tissues and their dielectric properties. Therefore, different tissues in specific for their frequencies will receive the maximum amount of heat.

3. Basic components of the UHF therapy and the visualization of the UHF electromagnetic field

The impact of high-frequency electrical field on certain areas of a human's body can be achieved through condenser electrodes (Figure 1) or inductive electrodes (Figure 2).

Electrodes are placed directly on the area, which has to be heated, or at some distance from it. Electrodes can be closer or further away, so they can adjust their distance to the skin, which must be 2-10cm. To protect the skin from contact with the electrode and to provide the desired spacing to it, we have to put rubber insulated electrodes or glass. Some examples of the impact of different types of electrodes are shown in Figure 3.1, Figure 3.2, Figure 3.3. [1]

As we seen from the figures, depending on the location of the electrodes and their size, we can determine the distribution of field and the temperature change in the exposure range.

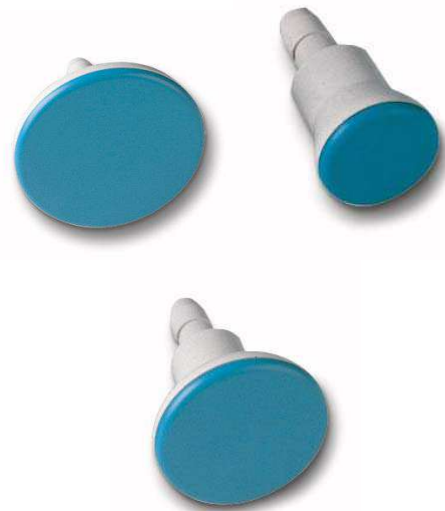


Figure 1. Condenser electrodes with different sizes



Figure 2. Coil field electrode with different size and type

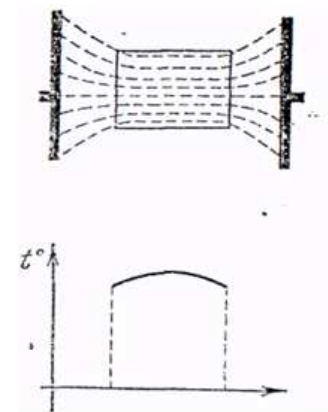


Figure 3.1. The impact of different types of electrodes

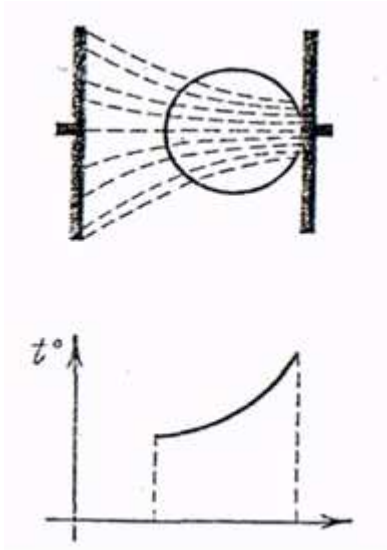


Figure 3.2. The impact of different types of electrodes

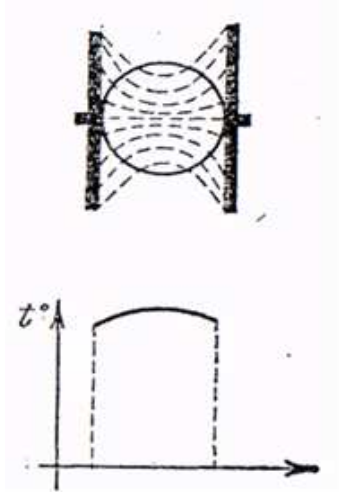


Figure 3.3. The impact of different types of electrodes

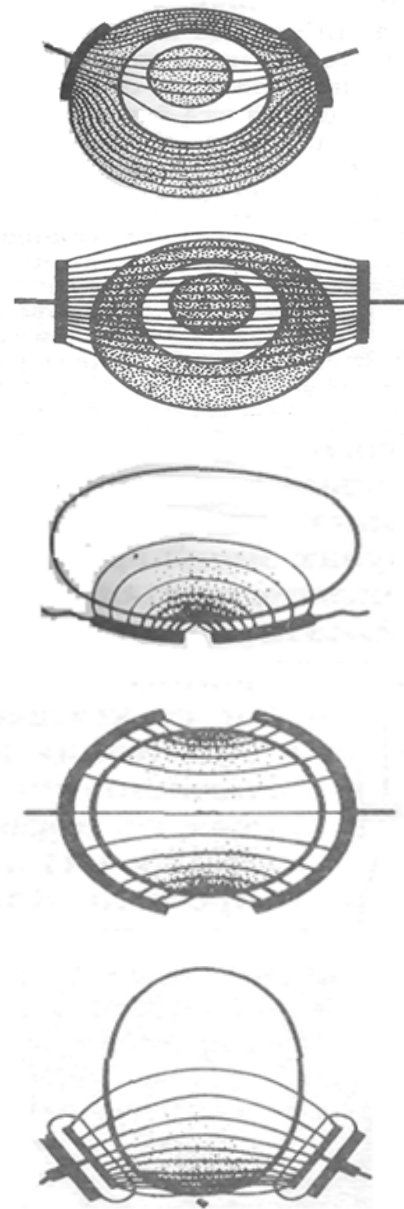


Figure 4. The lines of the force of the electric field at different mutual disposition of the electrodes

As already mentioned, the placement of the electrodes is really important because the field is changed, and also their magnitude. In Figure 4 can be seen the lines of the force of the electric field at different mutual disposition of the electrodes. [1]

Figure 5 shows an apparatus for UHF [4]. Their load varies widely, which modifies the parameters of the load (patient) circle. Moreover, during the treatment, the object that is subjected to impact, can easily shift. As a result, power supply of the object decreases. On the other hand, under different conditions of the sessions, more or less, the large part of the energy is dissipated, i.e. to achieve a therapeutic result, they need a different power sets.



Figure 5. Device for UHF therapy

4. Positive influence of UHF therapy on the human body

The power is allocated also on how the doses of the patient should be. The dosage is 4 steps in the intensity of thermal sensation. [3]

- Athermic doses – lowest thermal doses in which the patient has no subjective feeling.
- Oligothermal doses with a subtle sense of warmth.
- Thermal sensation with a pleasant warmth
- Hyper-intensive thermal with heat sensation.

These doses are equivalent to the objective intensity of the electric field. Athermic and oligothermal dosages are with power to the electric field 60-80W. In practice, they use mainly the first 2 levels of dosage. The principle is during acute, subacute processes are used the first 2 doses and during a chronic stage may be reached from oligothermal to thermal doses. The duration of the procedure varies from 5-15-20 minutes. During acute processes with short duration 5-8 minutes and has to increase the duration of chronic diseases. Low doses from 3-8 min average are used in children, depending of the age.

If the electrodes are inductive and the tissues are subjected to a magnetic field, they are induced eddy currents with the same frequency. Because the induced currents are mainly by tissue, containing more fluid, they are warmed more (muscles, internal organs). Endogenous heat formed in the tissues as a result of UHF currents, differs from exogenous heat introduced from the outside (visible, infrared): has greater penetrating power, not committed and not wear thermoregulatory mechanisms, not burden the cardiovascular and respiratory system, continues to be formed after the cessation of irradiation, radiation from the body becomes slower. Endogenous heat increases the molecular kinetic energy, increase metabolic processes within cells, accelerating chemical reactions at the molecular and sub molecular level, activated oxygen absorption and elimination of carbon dioxide. Apart from endogenous heat, the biological effect of UHF is carried out through their effect on an oscillating tissue molecules, on which influence it. UHF stimulates the function of endocrine glands. In the nervous system are leading the analgesic effects which binds both direct suppressive effect on the

receptors and afferent neurons, so and with hyperemia and anti-inflammatory effect of UHF. Urinary system does not respond in healthy subjects. Typical is a vasodilator effect on UHF on vessels of the kidneys in acute and chronic glomerulonephritis with a strong anti-inflammatory and diuretic effect. The cardiovascular system responds primarily when there are any diseases: in peripheral vascular disorder, progressing with spasm (Raynaud's disease). UHF leads to active hyperemia, for hypertension (I and II degree Lang) is observed a hypotensive effect of electrode placement in the renal-adrenal area.

5. Conclusion

1. Describes the change of the field from the location and the different size of electrodes, images to the field with lines of force, heat generation in the body.
2. Positive effect of the UHF therapy in our bodies

References

- [1] D. Dimitrov, Medical systems influence of electromagnetic fields on human, education book, TU-Sofia,2007
- [2] W. Y. Riadh, "Electromagnetic Fields and Radiation (Human Bioeffects and Safety)",Marcel Dekker Inc. Canada,2001,ISBN 0-8247-0877-3
- [3] Shoogo Ueno, Biological Effects Of Magnetic And Electromagnetic Fields (The Language Of Science)
- [4] Internet: <http://medeos.com>

LOW PHASE NOISE KU BAND PUSH – PUSH OSCILLATOR

Mihail Plamenov Tonev

Technical University of Sofia, Bulgaria)
Faculty of Telecommunication, TU-Sofia, “Kl. Ohridsky” str. 8, 1000 Sofia, Bulgaria
E-mail: mihail_tonev@abv.bg

Abstract

As commonly known, oscillators play very important role in all communication and test equipment. Most of modern communication systems are using different types of digital modulation techniques. That’s why Bit Error Rate is key parameter, used to evaluate quality of communication equipment. Improving of this parameter is related to using oscillators with low phase noise in transmitters and receivers. Design of low noise oscillators become a major task for engineers. With increasing frequency of generated signal this task is hardly desirable. In this paper is presented method for solving this problem. A Clapp Voltage Controlled Oscillator in push – push configuration using SiGe bipolar junction transistor is presented. The oscillator is used in Ku band and reaches phase noise performance down to -100dBc/Hz at 100 KHz offset and tuning range of 10%.

1. Introduction

The push – push principle is widely accepted as approach to realize low phase noise high frequency oscillators. To be reached good phase noise performance of oscillators is necessary to be used resonators with high Q factor. In microwave frequencies are widely used dielectric resonators. Oscillators realized with them have very good phase noise but are difficult for implementation. Oscillation frequency should be tuned manually using screw. Furthermore frequency stability over temperature changing is not sufficient for bulk of modern communication equipment. Decision of this problem is to be used frequency synthesizers. This leads to need of high frequency voltage controlled oscillators. For their realization are used varactor diodes as tuning elements. At high frequencies (X, KU, Ka band) varactor diodes have low Q factor. This is the main difficulty in design low phase noise VCO’s. Furthermore they have parasitic resonances, which sometimes make design of such oscillators impossible. These problems can be solved using push - push oscillator. The idea is to be designed two oscillators working at half of desired output frequency. After coupling them the output spectrum contain only even harmonics. Second harmonic can be used as output frequency.

2. Push – push oscillators

Simplified schematic of two coupled oscillators is shown in fig.1. Considering the transmission line acts as resonant circuit in addition to coupling network, and for simplification in the analysis, the loss associated with the transmission line is assumed as part of load admittances G_L . In fig.1 Y_{d1} and Y_{d2} represent equivalent admittance of two active devices and their loads, while Y_{C1} and Y_{C2} represent admittances seen by devices in mutually coupled oscillator circuit.

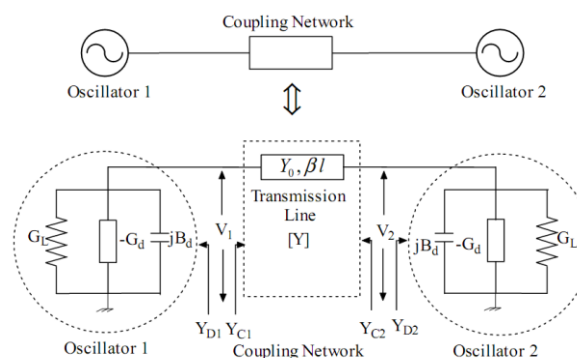


Fig. 1. Principle schematic of coupled oscillators

For coupling two oscillators phases of output signals must be synchronized. Phase synchronization is reached with transmission line with characteristic admittance Y_0 and electrical length βl . The electrical length of transmission line has to be chosen such that both oscillators are working individually and generate the same output frequency. For this reason active devices have to see the same impedance from the both sides of transmission line. This can be realized if electrical length is chosen to be half wavelength for fundamental frequency of oscillators. Figure 2 shows the push – push oscillator using half – wavelength microstrip resonator. For fundamental frequency f_0 this resonator has a null point at the centre of microstrip line, being a point of oscillator symmetry which is considered as virtual ground or short – circuited point. In this case, the

resonance voltage has maximum values at both ends of resonator with phase difference of 180deg and resonance voltage is zero at the centre of resonator. For desired second harmonic frequency $2f_0$ such point could be regarded as an open circuited point.

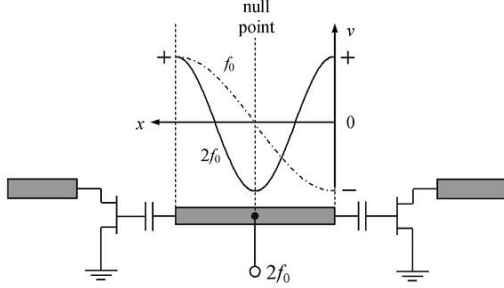


Fig. 2. Push – push microstrip oscillator configuration

For analysis purpose, transmission line is characterized as two port network with its terminal voltages represented by voltage phasor as $V_1 = |V_1|e^{j\varphi_1}$ and $V_2 = |V_2|e^{j\varphi_2}$ where $|V_1|$, $|V_2|$, φ_1 and φ_2 are magnitudes and phases of voltage phasors. Transmission line can be represented with its ABCD matrix:

$$(2.1) \quad ABCD = \begin{bmatrix} \cos \beta l & jZ_0 \sin \beta l \\ jZ_0 \sin \beta l & \cos \beta l \end{bmatrix},$$

where Z_0 , l and β are characteristic impedance, length and phase constant of transmission line. For purpose of this analysis is necessary to be calculated Y matrix of transmission line. Relationship between Y matrix and ABCD matrix is:

$$(2.2) \quad Y_{11} = \frac{D}{B}; \quad Y_{12} = \frac{BC - AD}{B};$$

$$Y_{21} = -\frac{1}{B}; \quad Y_{22} = \frac{A}{B}$$

From 2.1 and 2.2 Y matrix is given by:

$$(2.3) \quad Y_{TRL} = \begin{bmatrix} Y_{11} & Y_{12} \\ Y_{21} & Y_{22} \end{bmatrix} =$$

$$= \begin{bmatrix} -jY_0 \cot \beta l & jY_0 \frac{1}{\sin \beta l} \\ jY_0 \frac{1}{\sin \beta l} & -jY_0 \cot \beta l \end{bmatrix}$$

The circuit equation for Fig.1 at transmission line terminals can be expressed as

$$(2.4) \quad -Y_{D1}|V_1|e^{j\varphi_1} = Y_{11}|V_1|e^{j\varphi_1} + Y_{21}|V_2|e^{j\varphi_2}$$

$$(2.5) \quad -Y_{D2}|V_2|e^{j\varphi_2} = Y_{21}|V_1|e^{j\varphi_1} + Y_{22}|V_2|e^{j\varphi_2}$$

Equations 2.4 and 2.5 can be expressed in matrix form as:

$$(2.6) \quad \begin{bmatrix} -Y_{D1}V_1 \\ -Y_{D2}V_2 \end{bmatrix} = \begin{bmatrix} Y_{11} & Y_{12} \\ Y_{21} & Y_{22} \end{bmatrix} \begin{bmatrix} V_1 \\ V_2 \end{bmatrix}$$

For identical coupled oscillators:

$$(2.7) \quad V_1 = V_2 = V; \quad Y_{D1} = Y_{D2} = Y_D; \quad Y_{c1} = Y_{c2} = Y_c$$

From equations 2.4, 2.5 and 2.7

$$(2.8) \quad e^{\pm j(\varphi_1 - \varphi_2)} = e^{\pm j(\Delta\varphi)} = \frac{Y_D + Y_{11}}{-Y_{12}}$$

The admittance Y_D comprises of device admittance and load conductance as

$$(2.9) \quad Y_D = G_L - G_D + jB_D$$

The admittance Y_C is given from the transmission line equation as

$$(2.10) \quad Y_C = Y_0 \left[\frac{Y_D + jY_0 \tan(\beta l)}{Y_0 + jY_D \tan(\beta l)} \right] =$$

$$= Y_0 \left[\frac{Y_D + jY_0 \tan \Theta}{Y_0 + jY_D \tan \Theta} \right]$$

To be satisfied conditions for oscillation, the length of transmission line is selected such that real and imaginary part of admittance Y_C is given by:

$$(2.11) \quad \text{Re}[Y_C] = G_L - G_D$$

$$(2.12) \quad \text{Im}[Y_C] = -jB$$

From equations 2.9 and 2.10

$$(2.13) \quad \tan(\beta l) = \frac{2B_D Y_0}{B_D^2 - Y_0^2 + (G_L - G_D)^2}$$

During the process of starting up oscillations, the real part of admittance Y_D is more negative than

admittance of losses. As level of generated signal increases, the device gain drops until the losses are compensated. Under the steady state oscillation conditions, $G_L - G_D = 0$ and electrical length Θ of transmission line is given from equation 2.13 as

$$(2.14) \quad \tan(\beta l) = \frac{2B_D Y_0}{B_D^2 - Y_0^2} \Leftrightarrow$$

$$\Theta = \beta l = \tan^{-1} \left[\frac{2B_D Y_0}{B_D^2 - Y_0^2} \right]$$

To be determined Y matrix of transmission line is necessary to be defined $\cot(\beta l)$ and $\operatorname{cosec}(\beta l)$ functions.

$$(2.15) \quad \cot(\beta l) = \tan^{-1}(\beta l) = \frac{B_D^2 - Y_0^2}{2B_D Y_0}$$

$$(2.16) \quad \frac{\cos(\beta l)}{\sin(\beta l)} = \frac{B_D^2 - Y_0^2}{2B_D Y_0} \Leftrightarrow \frac{1 - \sin^2(\beta l)}{\sin^2(\beta l)} =$$

$$= \frac{B_D^4 - 2B_D^2 Y_0^2 + Y_0^4}{4B_D^2 Y_0^2} \Leftrightarrow$$

$$\Leftrightarrow \operatorname{cosec}(\beta l) = \frac{1}{\sin(\beta l)} = \frac{B_D^2 + Y_0^2}{2B_D Y_0}$$

The [Y] parameter of the transmission line can be rewritten from equations 2.3, 2.15 and 2.16 as

$$(2.17) \quad Y_{TRL} = \begin{bmatrix} Y_{11} & Y_{12} \\ Y_{21} & Y_{22} \end{bmatrix} =$$

$$= \begin{bmatrix} -j \frac{B_D^2 - Y_0^2}{2B_D} & j \frac{B_D^2 + Y_0^2}{2B_D} \\ j \frac{B_D^2 + Y_0^2}{2B_D} & -j \frac{B_D^2 - Y_0^2}{2B_D} \end{bmatrix}$$

Phase difference between generated signals from two coupled oscillators can be determined from equations 2.8 and 2.17 and is given as

$$(2.18) \quad e^{\pm j(\varphi_1 - \varphi_2)} = e^{\pm j(\Delta\varphi)} = \frac{Y_D + Y_{11}}{-Y_{12}} = \begin{bmatrix} Y_D - j \frac{B_D^2 - Y_0^2}{2B_D} \\ -j \frac{B_D^2 + Y_0^2}{2B_D} \end{bmatrix}$$

In steady state oscillator mode $Y_D = jB_D$

$$(2.19) \quad e^{\pm j(\Delta\varphi)} = \frac{\left[\frac{2jB_D^2 - jB_D^2 + Y_0^2}{2B_D} \right]}{\left[-j \frac{B_D^2 + Y_0^2}{2B_D} \right]} = -1$$

$$(2.20) \quad e^{\pm j(\Delta\varphi)} = -1 \Rightarrow \Delta\varphi = \varphi_1 - \varphi_2 = \pm 180^\circ$$

With equations 2.1 – 2.20 was mathematically proven that two coupled oscillators generate phase synchronized signals with the same frequency and phase difference 180. If these two signals are summed in phase, with appropriate power combiner, the output signal in summing port can be expressed as

$$(2.23) \quad V_{out}(t) = V_{out_1}(t) + V_{out_2}(t) =$$

$$= \sum_n A_n e^{jn(\omega_0 t)} + \sum_n A_n e^{jn(\omega_0(t - \Delta t))}$$

Where n is harmonic number.

Equation 2.23 can be rewritten as

$$(2.24) \quad V_{out}(t) = A_1 e^{j\omega_0 t} (1 + e^{j\omega_0 \Delta t}) +$$

$$A_2 e^{j2\omega_0 t} (1 + e^{j2\omega_0 \Delta t}) + A_3 e^{j3\omega_0 t} (1 + e^{j3\omega_0 \Delta t}) + \dots$$

From equation 2.20, generated signals have phase difference 180 so $\omega_0 \Delta t = \pi$

$$(2.25) \quad e^{-j\pi} = \cos(-\pi) + j \sin(-\pi) = -1$$

$$(2.26) \quad e^{-j2\pi} = \cos(-2\pi) + j \sin(-2\pi) = 1$$

From 2.24, 2.25 and 2.26 the output signal of push – push oscillator is determined as

$$(2.27) \quad V_{out}(t)_{push-push} = \sum_n^2 2A_2 e^{j2\omega_0 t} +$$

$$+ 2A_4 e^{j4\omega_0 t} + 2A_6 e^{j6\omega_0 t} + \dots$$

Equation 2.27 shows cancellation of all odd harmonics especially the fundamental signal, where odd harmonics are added constructively. The higher order harmonics (4ω , 6ω , 8ω are filtered out).

3. Applications of push – push concept

In general push – push concept offers several advantages over single ended design:

- Since the transistors are operated at half of desired output frequency, the usable frequency range of devices can be extended;
- Simultaneous generation of both fundamental and second harmonic is feasible. Feeding f_0 into a frequency divider instead of $2f_0$ lowers divider efforts.
- Phase noise is reduced because of synchronization effects.
- High immunity against load pull.
- Extension of tuning range.

4. Design push-push VCO

The following shows example for design of mutually synchronized coupled voltage controlled oscillators. Generated signal can be tuned in range from 10.4GHz to 11.4GHz ($2f_0$) in which two individual oscillators oscillates at range of 5.2GHz to 5.7GHz. Figure 3 shows the circuit diagram of push – push oscillator. The circuit is fabricated on 0.51mm Rogers substrate of dielectric constant 3.38 and loss tangent $2.7 \cdot 10^{-4}$. Active devices, used to generate negative resistance are SiGe BJT transistors BFP620, produced by Infineon. As tuning elements are used varactor diodes BB837 also produced by Infineon.

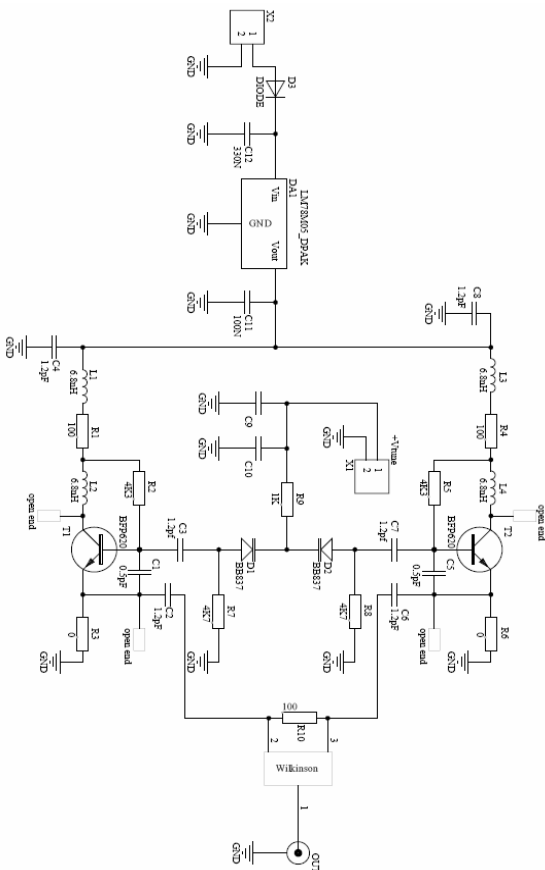


Fig. 3. Circuit diagram of push-push VCO

Figure 4 shows simulated (Ansoft Designer) base currents I_{b1} and I_{b2} which are phase shifted at 180 degree in mutually synchronized condition.

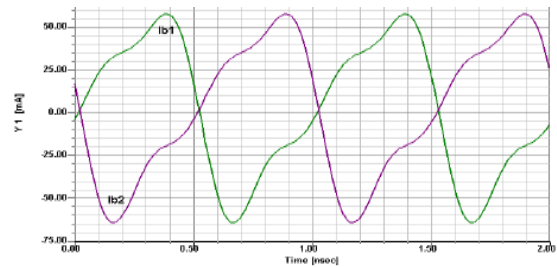


Fig. 4. Base currents of both transistors in push-push oscillator

The PCB layout of push – push oscillator is shown in fig.5. Outputs from both oscillators are summed by using Wilkinson combiner, designed for $2f_0$ frequency.

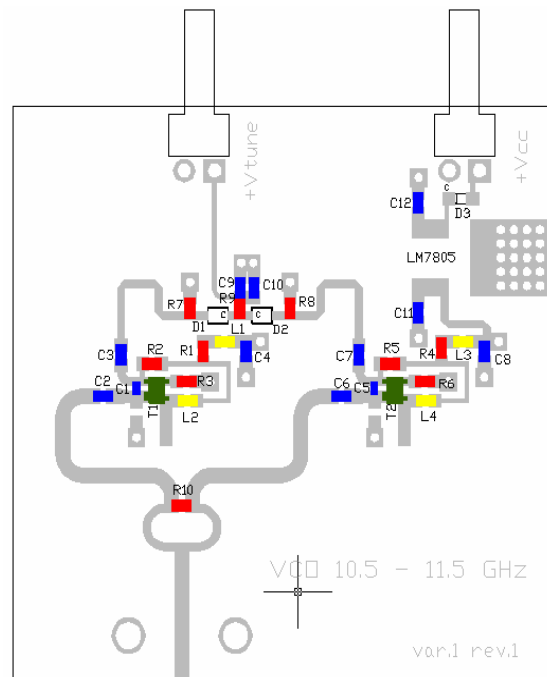


Fig. 5. PCB layout of push – push VCO

Measured results of oscillator parameters are presented graphically in figures 6, 7 and 8. Output spectrum is shown in fig.6. Suppression of first harmonic is about 25dB below second harmonic. This is due to non-ideal symmetry of the circuit. Two transistors with absolutely the same parameters are almost impossible to be found. First harmonic suppression can be improved by using active biasing of transistors.

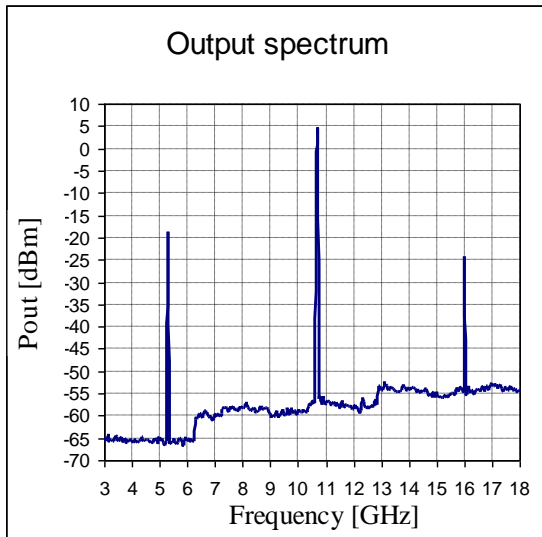


Fig. 6. Measured output spectrum of push – push oscillator

Figure 7 shows measured tuning range of designed voltage controlled oscillator.

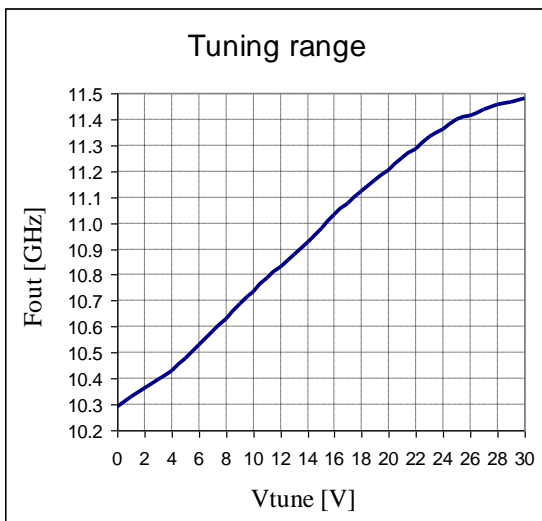


Fig. 7. Measured tuning range of designed VCO

Results from phase noise measurement at second harmonic of push – push oscillator are depicted in Fig.8. Measurements were performed for shorted tuning input and with 9V tuning voltage applied on it. It can be seen that, with shorted tuning input is retched about 3dB better phase noise than with applied 9V tuning voltage. This can be explained with noise added from voltage source at input of VCO.

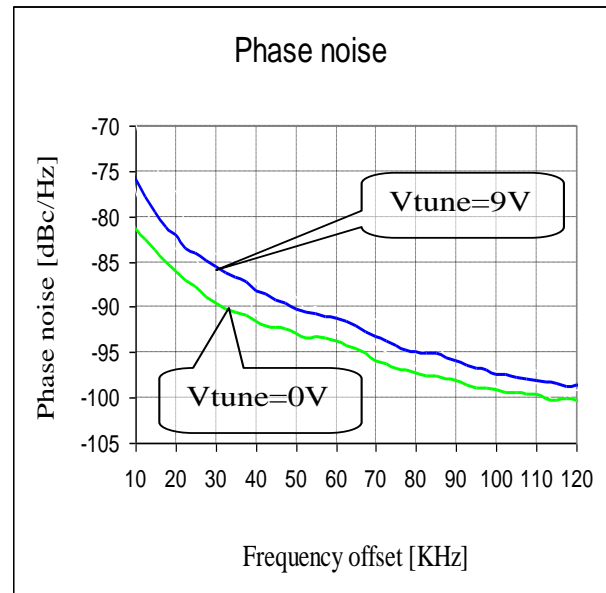


Fig. 8. Measured phase noise at second harmonic of push-push VCO

5. Conclusion

The main goal of this paper is to present method for design microwave voltage controlled oscillators with low phase noise. It was analytically shown that is possible to synchronize two oscillators and frequency of generated signal to be twice fundamental frequency of single oscillator. This statement is very important in design microwave VCO's, because it is general method for reducing phase noise. A example for Ku band VCO design, using mutually coupled oscillators was presented. Measurement results of manufactured VCO confirm statement that two oscillators can be synchronized to generate twice bigger output frequency.

References

- [1] Ulrich Rohde 'A new efficient method of design low noise microwave oscillators' Synergy Microwave Corporation
- [2] Ulrich L. Rohde, Ajay Kumar Poddar, and Georg Bock 'THE DESIGN OF MODERN MICROWAVE OSCILLATORS FOR WIRELESS APPLICATIONS' John Wiley & Sons
- [3] Andrei Grebennikov 'RF and microwave transistor oscillator design' John Wiley & Sons
- [4] Vendelin Rohde, Pavo 'Microwave circuit design using linear and nonlinear techniques
- [5] Matthias Schott, Friedrich Lenk, Chafik Meliani and Wolfgang Heinrich 'Low Phase Noise X-Band Push-Push Oscillator with Frequency Divider' MTT

SYSTEM FOR SIMULTANEOUSLY THERAPY BY RUNNING LOW FREQUENCY MAGNETIC FIELD AND ACUPRESSURE

Dimiter Tz. Dimitrov, Sasho Guergov

**Technical University of Sofia, Bulgaria
1000 Sofia, "Kl. Ohridsky" str. 8
Tel. (+359 2) 965-2278; e-mail: dcd@tu-sofia.bg*

Abstract

An simultaneously application of low frequency magnetic field and acupressure is described in the paper. A visualisation of space configuration of low frequency static magnetic field is done in the paper, also. A design of system for acupressure is done together with mathematical description of action of mechanical device for acupressure. The requirements for design of system for therapy with low frequency magnetic field and acupressure is presented. Some mechanical solutions for system for acupressure are described in the paper, also.

1. Introduction

The results of therapy by acupressure would be more good if there would be provided more intensive movement of the blood in around the points of acupressure. This activation of blood's movement can be provided by application of low frequency magnetic field together with acupressure.

The application of China's method for acupressure is very actual in medical therapy, now. Usually physician provide application of acupressure by his hands. It's inconvenient first of all for physician. He's able to work for short time. Then he can continue after relax, but the number of these procedures per day are limited. In other side it would be better to provide acupressure simultaneously on more points on the human body. It's impossible because physician has only two hands.

It's clear that it's necessary to provide special device for acupressure, which can be used together with special device for creating of low frequency magnetic field around the points for acupressure. Therefore the application of system for simultaneously application of acupressure and low frequency magnetic field is very actual, now.

2. Design of devices for creating of low frequency magnetic field around the points for acupressure

Usually the low frequency magnetic field can be created using two coils, connected to the output of apparatus for magneto-therapy. This apparatus is a source of special electrical signals for the coils. The space configuration of magnetic field in the patient's area depends to the mutual disposition of local inductors and the value of electrical current in the inductors. Always the inductors are without ferrous core. Therefore the waveform of magnetic induction is the same as the waveform of electrical current in the coils (inductors). Usually the waveform of electrical current in the coils is as rectangular pulses with variable frequency in the frequency band 0,1Hz – 100Hz. It's difficult for the organism to do an adaptation to the parameters of magnetic field because of variable frequency. This provides more good results after magneto therapy. These results can be obtained after short time of application of magnetic field. The magnetic induction in the patient's area should not exceed 10 mT.

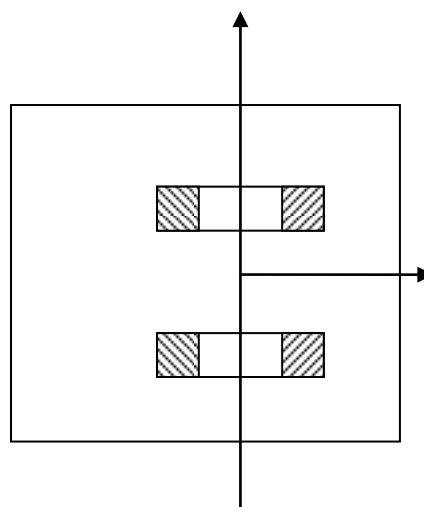


Fig. 1. Disposition of the two inductors

The space configuration of magnetic field can be seen on the base of mathematical description of magnetic field and computer simulation. The mutual disposition of the two inductors can be seen on Fig. 1. The space disposition of the lines of vectors of magnetic induction in the points of plane XOZ can be obtained by mathematical description and computer simulation. It can be seen on the Fig. 2.

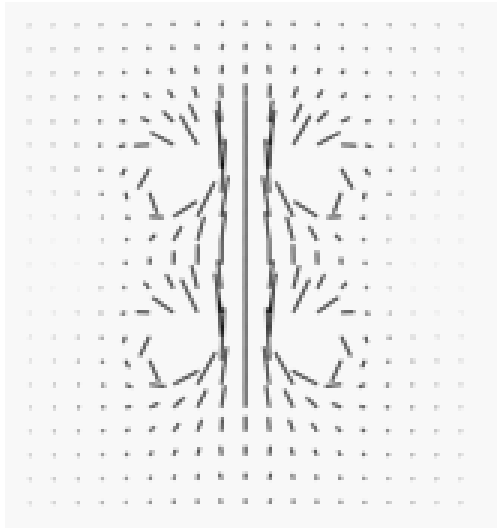


Fig. 2. Space dispositions of the lines of vectors of magnetic induction in the points of plane XOZ

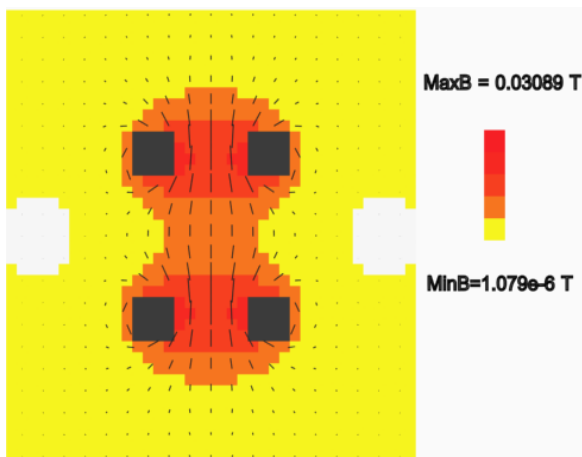


Fig. 3. Space distribution of the values of magnetic induction in the points of plane XOZ

The space distribution of the values of magnetic induction in the points of plane XOZ is an other result of computer simulation of space-temporal configuration of low frequency magnetic field in the patient's area. It can be seen on the Fig. 3. The calculation has been done for the value of relative magnetic permeability of alive tissues 1 and value of electrical current in the coils $I=2A$.

3. Design of the bed for therapy by running magnetic field

The method for computer simulation of space configuration of low frequency magnetic field of pair coils can be used for computer simulation of space configuration of magnetic field in the case of running magnetic field, also. In this case the coils can be as one or two sequences on the bed Fig. 2.

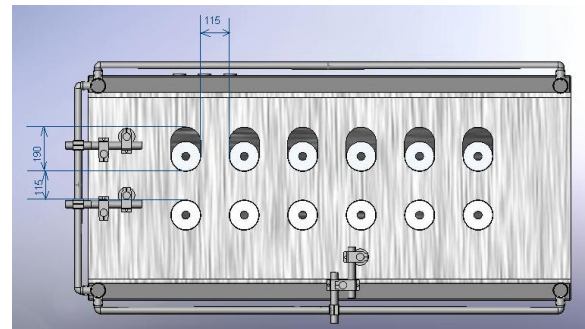


Fig. 4. The disposition of coils on the bed in the case of running magnetic field

The materials of the bed should be non magnetic. An appropriate plastic can be used. This plastic should has enough mechanical strong. This materials should has high mechanical hardness, high chemical steady, high steady for wear out, good skid, high electrical steady, good absorption of hits.

The patients should be recumbent on the coil's sequence on the bed. The mutual disposition of two sequence coils and patient's body can be seen on fig. 5.

On the patient's body should be two or more mobile coils depend of the number of coil's sequences. The coils on the bed should be on when they are under mobile coils.

The "movement" of low frequency magnetic field can be obtained by electronic switching over of the coils on the bed together with electronic switching over of several coils situated on special rolling stand on the human body. The apparatus for magnetotherapy, which provides the signals for coils can be seen on fig. 7. The space distribution of magnetic induction's value of running magnetic field (fig. 6) has been done for different position of "mobile" coils.

The apparatus for magnetotherapy, which provides the signals for coils can be seen on fig. 7. This apparatus can provide measurement of the value magnetic induction in different points around the

human body, using special drill for low frequency magnetic field.

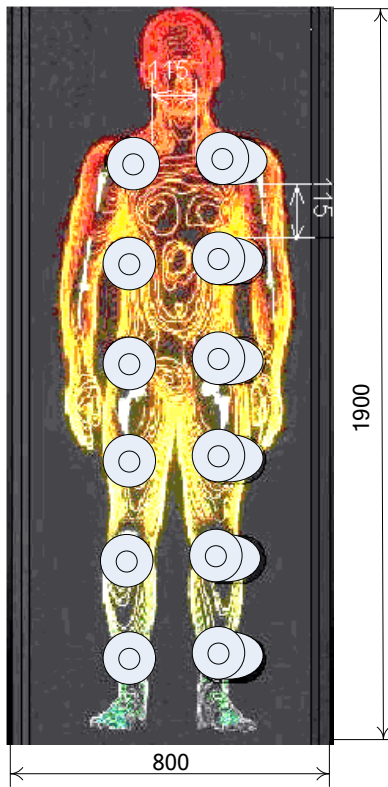


Fig. 5. Mutual disposition of two sequence coils and patient's body

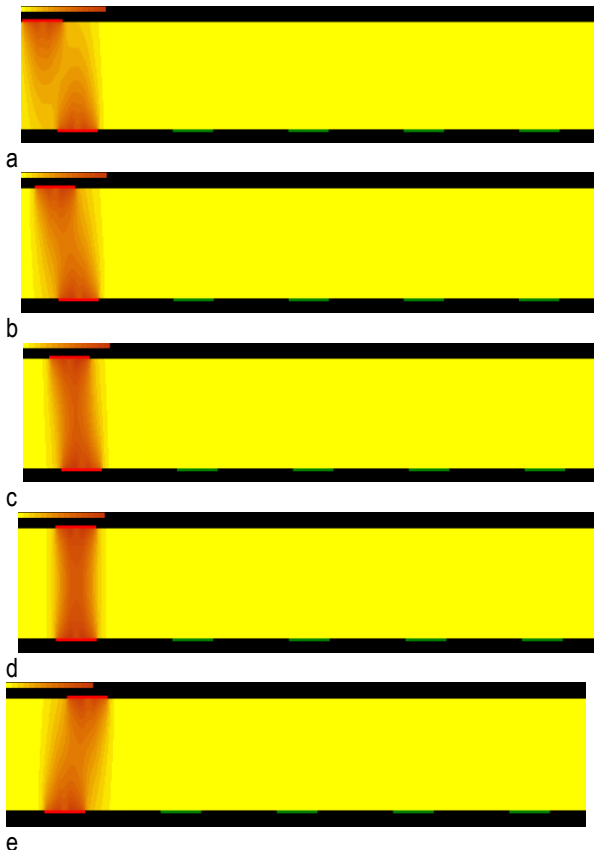


Fig. 6. Space distribution of magnetic induction's value of running magnetic field



Fig. 7. Apparatus for magneto-therapy

4. Design of mechanical device for acupressure

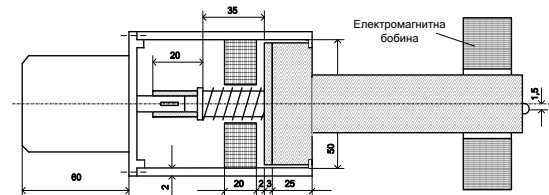


Fig. 6. The modified device for acupressure simultaneously with low frequency magnetic field

Usually the line of mechanical pressure is the axis of coils. The sizes of coils can be different according to the sizes of "active" area around of the acupuncture points. On fig. 6 can be seen a mechanical device for acupressure. For simultaneously application of low frequency magnetic field and mechanical acupressure, the line of mechanical pressure should be the same as the line of coil.

3. Conclusion

1. A bed for simultaneously therapy by running magnetic field and acupressure has been suggested in the paper.

2. A computer simulation of space distribution of magnetic induction' values of pair coils depending of the value of electrical current around the points of acupuncture in different cases of disposition of coils on the human body has been done in the paper.

3. A mechanical construction of device for simultaneously acupressure with low frequency magnetic field (Fig. 6) have been done, also.

References

- [1] D. Tz. Dimitrov, Computer Simulation of Space Configuration of Low Frequency Magnetic Field in Magnetotherapy, p.28-32, Electronics and Electrical Engineering, ISSN 1392-9631, 2005, -No.3 (59).
- [2] Д. Ц. Димитров, Изследване на пространствената конфигурация на нискочестотно магнитно поле в магнитотерапията. стр. 38-43. "Електроника и Електротехника", No. 9-10, 2005.
- [3] D. Dimitrov, A. Dimitrov, Computer Simulation of Low Frequency Magnetic Field, p.171-175, Proceedings of 17th EAEEIE Annual Conference on Innovation in Education for Electrical and Information Engineering, June, 1-3, 2006, University of Craiova, Romania.
- [4] Хилебрехт, М. Акупресура, ISBN9548793253, Емас, 1998, с. 240.
- [5] Хилебрехт, М. Акупресура – път към добро здраве, Емас, 2000, с.240.

CHANNEL ZAPPING TIME ANALYSIS OF IPTV OVER WIMAX ACCESS NETWORK

Brunonas Dekeris

Lina Narbutaitė

Rasa Brūzgienė

*Kaunas University of Technology
Department of Telecommunications
Studentų str. 50-452, Kaunas, Lithuania, LT- 51368
E-mail: rasa.bruzgiene@ktu.lt*

Abstract

IPTV – Internet protocol television - is a digital TV broadcast over IP networks, providing not only direct TV broadcasts, but also multiple additional services such as Video on Demand, an electronic program guide, internet service on the TV screen, games, karaoke and so on. IPTV and ancillary services conducted combining unicast and multicast flows in the methods of communication both core and access networks using different transmission methods, which are characterized by distinctive flows through the factors that influence the QoS. One of the most important factors for users evaluation of quality of service is a channel zapping time. Some of the factors that influence IPTV service channel zapping time is the delay in access and the user's home network nodes. In this paper we analyze the provision of IPTV over WiMax access network (IEEE 802.11d), the potential problems and the factors influencing the TV channel zapping time. A method to minimize the TV channel zapping time and simulated test environment results are presented and compared with the conventional transmission of IPTV over Wimax access network and proposed method of transmission over DSLAM access network.

1. Introduction

IPTV is defined as a multimedia service, with the necessary of using an IP core network and service providers chosen access network for TV channels transmission. Unlike the core network, the selection of IPTV access network is influenced by various factors, such as: geographic location of IPTV users, infrastructure of equipment deployment options in the access network, the economic benefits and in this case for IPTV service providers is especially important properly choose the right infrastructure of IPTV service access network.

WiMax (Worldwide Interoperability for Microwave Access) is a wireless access network, widely used

for high data rate in a wide range of users coverage. Due to the wide range of users coverage, WiMax network provides access to the services in remote areas, where implementation of other access infrastructure (DSL, optic) is simply too expensive or altogether impossible. These basic characteristics affect service providers selection of WiMax network as an access network for IPTV and additional multimedia services. There are two principal WiMax network structures: fixed access WiMax network (IEEE 802.16d) and mobile access WiMax network (802.16e) [1]. In this paper authors analyze the impact of WiMax network (IEEE 802.16d) used as an IPTV access network to IPTV QoE (Quality of Experience) in respect of the users.

IPTV service providers undertake to ensure proper quality of service (QoS) in accordance with approved ITU-T recommendations, ensuring TV users satisfaction with the service. Quality of Service (QoS) and service quality of experience (QoE) ratio is very important for the IPTV service, because each of these characteristics value affects the IPTV service core and access networks settings, such as [2]:

- Packet loss rate;
- Packet jitter;
- End to end delay;
- Channel zapping time.

IPTV traffic transmission rate over fixed Wimax access network varies from one to several Mbps and therefore transfer rate for service is limited. Due to the limited access network bandwidth, IPTV service equipment, such as STB (Set Top Box), can not simultaneously receive all broadcast channels and when the user selects of a new TV channel inevitably emerges channel change delay in the access

network [3]. Method to minimize IPTV channel zapping time over fixed WiMax access network and simulation results are presented in this paper.

2. IPTV over fixed WiMax

IEEE 802.16d fixed wireless access network provides the opportunity to transfer both standard definition (SD) and high definition (HD) video streams, accordingly WiMax access network is used for IPTV service provision. Figure 1 shows the architecture of IPTV service over fixed WiMax access network.

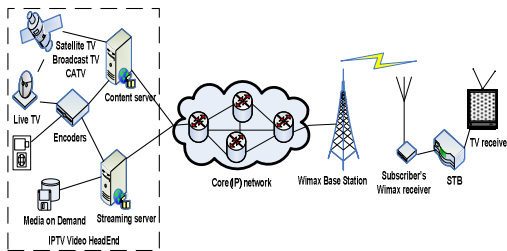


Figure 1. IPTV over fixed WiMax access network

IPTV service architecture over a fixed WiMax access network consists of Video HeadEnd, core (IP) network, access network (WiMax Base Station (BS), subscriber's WiMax receiver, STB (Set Top Box), TV receiver.

3. IPTV channel zapping time

IPTV channel zapping time is the time lag from the channel change request as the user pushes the button on the remote control until the first video I frame is received on STB. Channel zapping time is an important QoE parameter for IPTV user, so in this case, according to the research work [4], channel zapping time should be less than 0.43 ms in order to ensure user satisfaction with the IPTV service by at least 3.5 points by MOS (Mean Opinion Score), so it is very important as far as possible to reduce it.

IPTV service channel changing process is presented in Figure 2. The channel zapping time is composed of these main factors:

- IGMP processing time – delay, resulting from the first IGMP Leave request on the STB to the Home Gateway until the first I frame of the selected TV channel, received in the STB buffer;

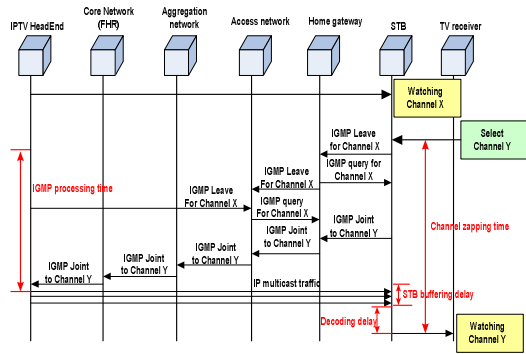


Figure 2. Overview of channel zapping time

- Access network delay – time, needed to broadcast video stream from the selected channel IGMP Join request submission;
- STB jitter buffer delay – is required to remove the unsmooth display caused by the delay jitter over the Internet [3];
- Video decoding delay – the time required for video stream decoding and presentation from the STB to the TV receiver. This time is influenced by the arrangement of images sequence (I, B, P) in the GOP (Group of Picture).

4. Proposed IPTV channel change method

To compare the results obtained by simulation [3], authors proposed IPTV channel change method is adapted to the IEEE 802.16d WiMax access network (Figure 3).

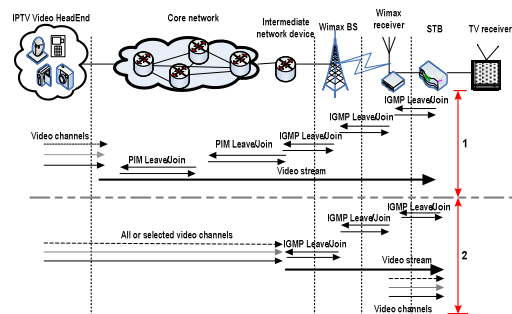


Figure 3. IPTV channel change using multicast channel flow (1) and proposed transmission method (2) using fixed WiMax access network

Figure 4 presents the IPTV service channel change algorithm using the authors proposed IPTV transmission method.

The main idea of the proposed channel change method is that, when the IPTV service user press

the channel change button on the remote control and looks forward during switching process less than 1 minute (T_v), the intermediate network device starts send less quality (MPEG - 2, SDTV) video stream of the selected channel. Less quality video stream is replaced by the high quality (HDTV) video stream only after 1 minute from the channel change request.

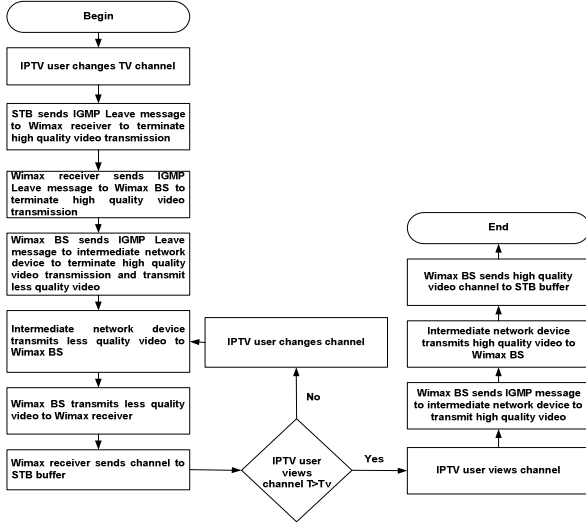


Figure 4. IPTV channel change algorithm of proposed transmission method

5. Mathematical model for IPTV channel zapping time evaluation over fixed WiMax access network

First of all, the IPTV channel zapping time evaluation over fixed WiMax access network has been done for two scheduling types of IPTV traffic: a non-priority and priority IPTV traffic. Figure 5 presents the schemes of two scheduling types of IPTV traffic.

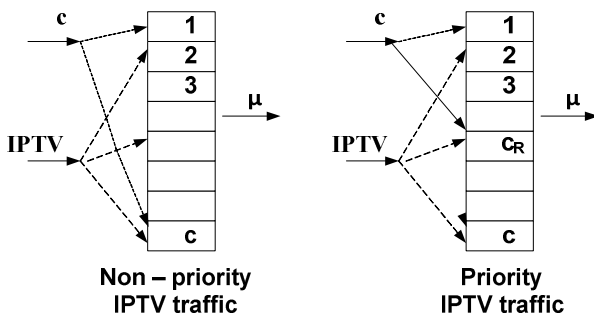


Figure 5. Schemes of two scheduling types of IPTV traffic: non - priority and priority

The non-priority scheme does not differentiate between common data traffic and IPTV traffic and all

channels in BS are using for all types of services. Using priority scheme channels were divided into two parts: normal and reserved for IPTV. When a common call arrives, the system will check if there is an available normal channel for it. If it is not available, the call will be blocked. When IPTV call arrives, the system will check if there is an available normal channel for it. If it is available, a channel will be assigned for the call. If it is not available, the system will check if there is an available reserved channel for it. If it is available, a channel will be assigned for the call. If it is not available, the call will be blocked. For evaluation the IPTV traffic blocking probability Markov chain is used. Each state, in the Markov chain represents the number of occupied channels. The all traffics are assumed to follow a Poisson arrival process with mean rates λ_c – for total channels and λ_{IPTV} – for IPTV channels. They have exponential service time distribution with mean rate $\frac{1}{\mu}$. Here are a total of C channels of

which $C_{IPTV}=C-C_R$ (where C_R – number of reserved channels) are prioritized only to IPTV traffic. Solving the Markov chain authors get IPTV traffic blocking probability:

- for non-priority scheme:

$$P_{IPTV} = \frac{(\lambda_c + \lambda_{IPTV})^c}{C! \mu^c} \cdot \frac{1}{\sum_{j=0}^c \frac{(\lambda_c + \lambda_{IPTV})^j}{j! \mu^j}}, \quad (1)$$

- for priority scheme:

$$P_{IPTV} = \frac{(\lambda_c + \lambda_{IPTV})^{C_{IPTV}} \times (\lambda_{IPTV})^{C-C_{IPTV}}}{C! \mu^C} \times P(0), \quad (2)$$

where P_{IPTV} – is IPTV traffic blocking probability; $P(0)$ – probability, that all channels are available:

$$P(0) = \left[\sum_{j=0}^{C_{IPTV}} \frac{(\lambda_c + \lambda_{IPTV})^j}{j! \mu^j} + \sum_{j=C_{IPTV}+1}^C \frac{(\lambda_c + \lambda_{IPTV})^j \times \lambda_{IPTV}^{j-C_{IPTV}}}{j! \mu^j} \right]^{-1}, \quad (3)$$

The channel zapping time is

$$D_{zapping} = D_{send} + D_{buff} + D_{signal} + D_{GOP} + D_{b-jitter} + D_{retrans} \quad (4)$$

where $D_{zapping}$ is the channel zapping time; D_{send} is the total channel change delay using conventional transmission; D_{buff} is the delay in STB buffer; D_{signal} is the IGMP signalling transmission delay; D_{GOP} is

the GOP delay; D_{b_jitter} is the dejitter buffer delay; $D_{retrans}$ is the retransmission delay. The total channel change delay, using conventional transmission can be expressed as

$$D_{send} = D_{transm} + D_{switch} + D_{IGMP}, \quad (5)$$

where D_{transm} is the transmission delay; D_{switch} is the switching delay; D_{IGMP} is the IGMP message transmission delay. The delay in STB buffer can be expressed as

$$D_{buff} = \frac{\frac{H_{r1} \times H_{r2} \times C_I \times F_I}{H_{comp}} \times N_{GOP}}{L_{BS} \times (1 - \rho_{other}) \times (1 - R_{IPTV})}, \quad (6)$$

where H_{r1} , H_{r2} are horizontal and vertical video resolution; C_I is the colour image intensity; F_I is the frame intensity; H_{comp} is the video compression rate; N_{GOP} is the number of GOP; L_{BS} is the line rate of BS; ρ_{other} is the traffic load of other services. R_{IPTV} is ratio, used for IPTV streaming, which can be evaluated as

$$R_{IPTV} = \frac{B_{MPEG} \times N_{ch} \times N_{ch-user}}{L_{BS} - (L_{BS} \times \rho_{other})}, \quad (7)$$

where B_{MPEG} is video MPEG bandwidth; N_{ch} is the number of channels; $N_{ch-user}$ is the number of users, which are using the same channel at the same moment.

The retransmission delay can be evaluated as

$$D_{retrans} = (D_{signal} \times P_{IPTV}) \times 10, \quad (8)$$

IGMP signalling transmission delay can be expressed as

$$D_{signal} = \frac{S_{IGMP} \times N_{ch-user}}{L_{rate_down}} + \frac{S_{IGMP} \times N_{ch-user}}{L_{rate_up}}, \quad (9)$$

where S_{IGMP} is the size of IGMP packet; L_{rate_down} is the downstream line rate of access network; L_{rate_up} is the upstream line rate of access network.

6. Results of IPTV channel zapping time over IEEE 802.16d access network using proposed transmission method

According to the mathematical model, the efficiency of the IPTV channel change algorithm of proposed

transmission method was performed using a Matlab simulation program. The initial data, used in simulation, according to Cisco and Agilent Technologies, are given in Table 1.

The simulation was done by changing the GOP size (Figure 7), IPTV probability P (Figure 8) and as were used other services in the network, not only IPTV, the load of other services ρ_{other} was varied too. Figure 6 presents IPTV traffic blocking probability in BS with two scheduling types.

Table 1. Parameters used in simulation

Parameter	Value
D_{b_jitter}	150ms
D_{transm}	80ms
D_{switch}	2ms
D_{IGMP}	20ms
D_{DSLAM}	50ms
L_{BS}	250Mbps
L_{rate_up}	3Mbps
L_{rate_down}	10Mbps
S_{IGMP}	64bit
N_{ch}	3
$N_{ch-user}$	20
H_{r1}, H_{r2}	920x782
C_I, F_I, H_{comp}	8, 30, 30
C	30
C_{IPTV}	5
B_{MPEG}	2Mbps

As can be seen, when is used the priority IPTV traffic, the probability that the call, that came will be blocked is far lower than in non-priority IPTV traffic. In this case, using a scheduling type of priority IPTV traffic in WiMax BS, IPTV applications will be attended with lower losses.

Comparing channel zapping time values of the proposed method of transmission over WiMAX access network to the IPTV transmission over DSLAM access network, when the GOP=1.6 s, channel zapping time increases by less than 0.6 s.

In contrast to the DSLAM, it is influenced by the retransmission delay over WiMax access network.

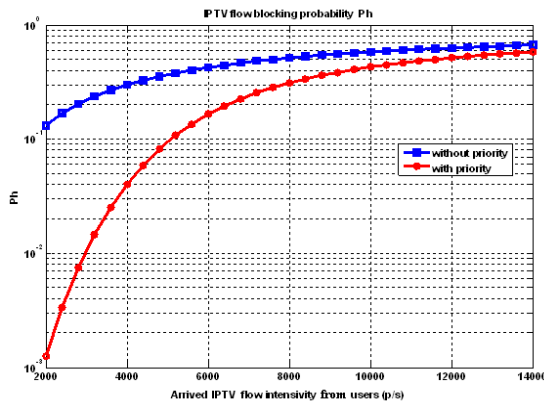


Figure 6. IPTV traffic blocking probability in BS with two scheduling types: with priority and without priority

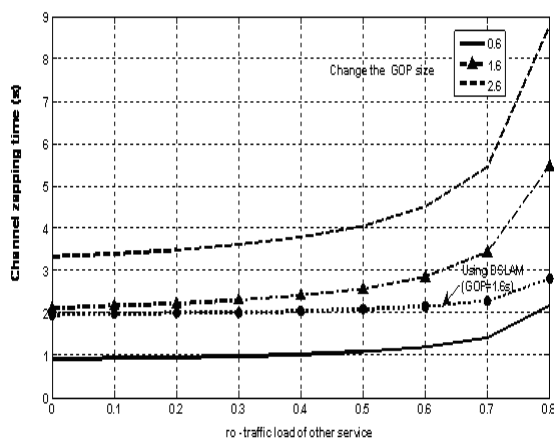


Figure 7. Channel zapping time versus load of other services, in the case of different GOP sizes (0,6 s; 1,6 s; 2,6 s)

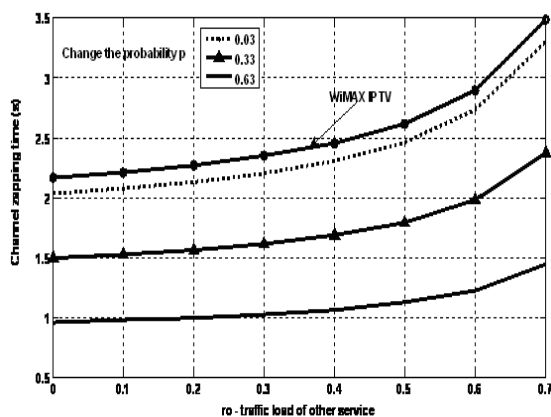


Figure 8. Channel zapping time versus load of other services in the case of different IPTV probabilities (0,03; 0,33; 0,63), GOP=1,6s

Comparing channel zapping time value of the traditional method of transmitting IPTV over WiMax to the proposed transmission method, when the GOP is equal to 1.6 s, it can be seen, that the pro-

posed method can reduce the channel zapping time by more than 1.5 s, and the load of other services may be up to 0.6 of total throughput.

7. Conclusions

In this paper authors proposed IPTV channel change transmission algorithm and compared channel zapping time: a) using conventional transmission over WiMax access network and proposed method; b) using transmission of proposed method over WiMax access network and DSLAM access network. According to the obtained results, it can be stated:

- using a non-priority IPTV traffic in WiMax BS, IPTV applications will be attended with more losses than priority IPTV traffic;
- if GOP = 0.6 s, channel zapping time is about 1 s using the proposed method of transmission over WiMAX access network;
- Channel zapping time value (GOP = 1.6 s) of the proposed transmission method is 1.5 times lower than in conventional IPTV transmission over WiMax.

References

- [1] Omneya Issa, Wei Li, Hong Liu, "Performance Evaluation of TV Over Broadband Wireless Access Networks", *IEEE Transactions on Broadcasting*, vol. 56, no. 2, June 2010, pp. 201-210.
- [2] Peter Siebert, Tom N. M. Van Caenegem, Marcel Wagner, "Analysis and Improvements of Zapping Times in IPTV Systems", *IEEE Transactions on Broadcasting*, vol. 55, no. 2, June 2009, pp. 407-418.
- [3] B. Dekeris, L. Narbutaite, "IPTV Channel Zap Time Analysis", *Electronics and Electrical Engineering*, no. 10 (106), Technologija, Kaunas, 2010, pp. 117-120.
- [4] R. Kooij, K. Ahmed, K. Brunnström "Perceived Quality of Channel Zapping", *Proceedings of the Fifth IASTED International Conference Communications Systems and Networks*, August 2006.

THE INVESTIGATION OF FILTERS FOR REAL-TIME DATA ACQUISITION

L. Svilainis¹, R. Jurkonis², D. Kybartas¹, A. Chaziachmetovas¹

¹Signal processing department, Kaunas University of Technology,
Studentu str. 50, LT-51368 Kaunas, Lithuania

²Biomedical Engineering Institute, Kaunas University of Technology,
Studentu str. 65, LT-51369 Kaunas, Lithuania

T. +370 37 300532; F. +370 37 753998;

E. linas.svilainis@ktu.lt / rytis.jurkonis@ktu.lt / darius.kybartas@ktu.lt / andrius.chaziachmetovas@ktu.lt

Abstract

Estimation of sound pressure level by using less expensive PVDF and BaTiO₃ multilayer ceramic ultrasonic transducers has been investigated. Calibration of proposed transducers was done with the help of commercial hydrophone HNP-1000 from Onda Corp., Sunnyvale. This work compares these less expensive transducers against hydrophone in sound pressure sensitivity over 1 MHz to 15 MHz frequency range. Experimental results are presented. The proposed inexpensive sensor design is using high voltage multilayer ceramic capacitor. It has indicated good sensitivity (0.5 μ V/Pa to 3 μ V/Pa) over frequencies 1 MHz to 8 MHz.

1. Introduction

The performance estimation of the sonoporation, therapeutic ultrasound, high intensity focused ultrasound (HIFU) [1], diagnostics and imaging equipment requires the acoustic pressure estimation [2]. Usually investigation is carried out using expensive hydrophone. Furthermore, hydrophone usually is made using Polyvinylidene Fluoride (PVDF) film and it is very sensitive to the mechanical damage [3]. When high intensity ultrasound is used, cavitation might rip out the PVDF metallization. It is desired to have the inexpensive sound pressure registration equipment with moderate sensitivity and accuracy. Experimental investigation of possible candidates is presented below.

2. Sensor requirements

Usual measurement procedure (Figure 1) involves the hydrophone as the local pressure sensor: hydrophone size is desired to be small. Results of Apfel and Holland presented in [4] indicate that at 1 MHz frequency the inertial cavitation threshold is 0.25 MPa of peak negative pressure; 0.6 MPa at

5 MHz and 0.85 MPa at 10 MHz. When hydrophone is used to determine how close the radiation is to the aforementioned thresholds, high sensitivity is not necessary. Intensities used in HIFU [5] can reach 30 MPa in compression and 10 MPa in negative peak pressure with optimal frequencies 0.7 MHz to 3 MHz [6]. Such pressures can damage the expensive sensor in case of long term use.

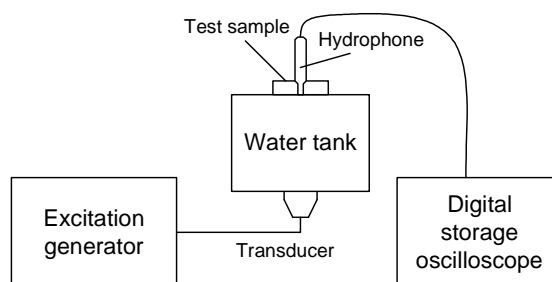


Figure 1. Hydrophone measurement

Such sensor also is used in transducer directivity study [7]. For general purpose studies the bandwidth beyond 5 MHz is sufficient.

3. Proposed sensors design

Two types of transducers were chosen for evaluation. One candidate was the epoxy-coated PVDF. Another was multilayer ceramic capacitor with sufficient BaTiO₃ content.

3.1. PVDF-based sensor

The main problem associated with PVDF application in pressure sensing is the rip off of the electrode due to cavitation. One of the possible solutions could be to coat the PVDF electrode with more durable material. We had such candidate availa-

ble. It had epoxy coating in front of 2.5 mm diameter PVDF film. Coating was also used for focusing: sensor had about 10 mm focal distance. Encapsulated transducer had 4 mm diameter.

On the other hand such design does not allow point pressure measurement: the result is the integrated pressure over the sensor's area.

3.2. BaTiO₃-based sensor

The multilayer ceramic capacitor (MLCC) usually has high capacitance thanks to high dielectric permittivity of the BaTiO₃ used as dielectric. The BaTiO₃ has piezoelectric properties. Therefore it was decided to use MLCC as sensing element. The idea of MLCC with BaTiO₃ use as the piezo-sensor is not new: authors [11] report MLCC use as inexpensive force sensor array. Capacitor is very small, cheap and has readily metallization. Thanks to multilayer structure it has to be better matched to coaxial cable impedance. It should be easy to polarise thanks to low Curie temperature (120°C) and high field strength thanks to multilayer structure (Figure 2).

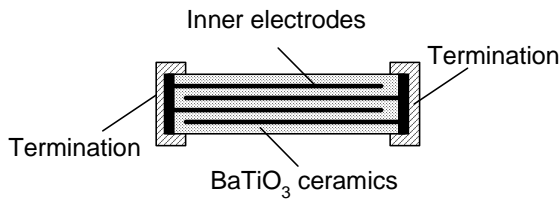


Figure 2. MLCC structure

The 1 nF 1206 size (3.2x1.6 mm and 1.25 mm thickness) 630 V MLCC with X7R class dielectric was chosen for experiments. Experiments were carried out to evaluate the most sensitive arrangement of the MLCC position in sensor (Figure 3).

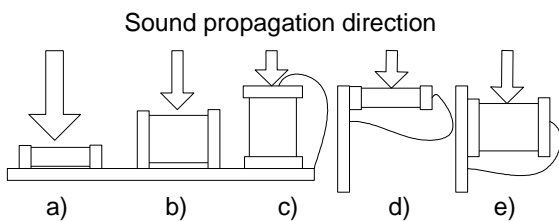


Figure 3. MLCC arrangement for sensitivity investigation

The spherically focused ultrasonic transducer by Karl Deusch (model TS 12PB2-7P30; frequency range 1 MHz to 6 MHz, diameter 12 mm) was used as ultrasound source. Acoustic beam of this transducer was investigated. Assessment was made using the 1 mm steel wire reflector in pulse-echo op-

eration mode [7]. Investigation of beam profile in longitudinal direction has revealed that peak intensity is at 27 mm (Figure 4). The lateral beam size is about 1.5 mm.

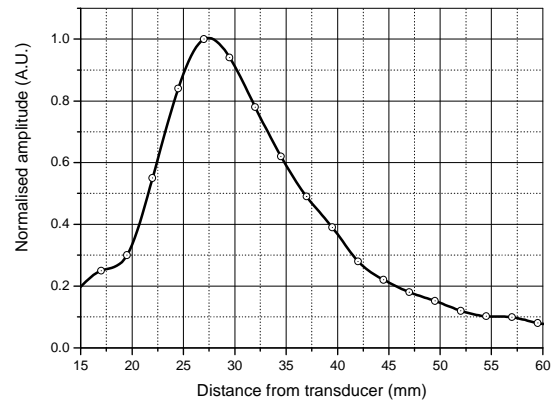


Figure 4. Acoustic source performance along transducer axis (longitudinal)

Sensor was placed at 27 mm distance from acoustic source according the Figure 1. Pulse trains of 2.7MHz frequency (transducer center frequency) 100Vpp square pulses were used for transducer excitation. The sensor output signal was averaged by scope (Hameg HMO3524) and peak negative voltage was registered.

Sensor was investigated in poled and un-poled conditions. Poling was performed using 500V source and 150°C hot air flow. Obtained results are grouped in Table 1.

Table 1. Transducer parameters

Arrangement	a	b	c	d	e
Ouput signal, unpoled, mVpp	4	1	4	8	2
Ouput signal, poled, mVpp	12	-	18	40	-

From Table 1 analysis it was decided to use arrangement d) for final sensor construction (Figure 5).

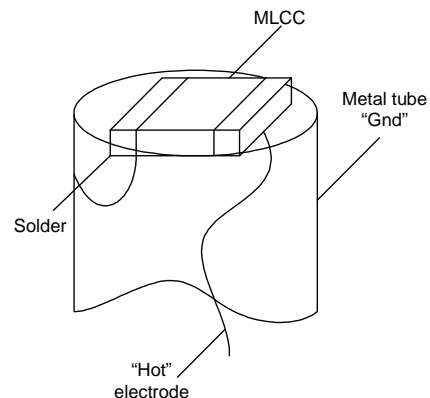


Figure 5. BaTiO₃-based sensor construction

MLCC was placed inside the 100 mm long 3 mm diameter tube and coaxial cable attached at the end.

4. Sensitivity investigation

Acoustic effect parameters can be assessed with the help of professional hydrophone. We have used the commercial hydrophone HNP-1000 from Onda Corp., Sunnyvale (Figure 6: sensitivity over frequencies range corrected according to [8]).

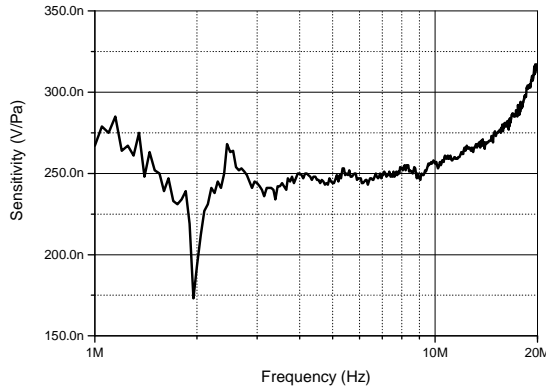


Figure 6. Hydrophone sensitivity

The sensitivity M of hydrophone was corrected using the hydrophone output capacitance $C_h(f)$ given in data sheet and the input capacitance C_{in} of the reception channel (oscilloscope) [8]:

$$M_c(f) = \frac{M(f)C_h(f)}{C_h(f) + C_{in}}, \quad (1)$$

Manufacturer declared calibration uncertainty is ± 1 dB for $1 \text{ V}/\mu\text{Pa}$ [9]. This hydrophone was used as reference for calibration.

Same focused ultrasonic transducer by Karl Deutsch was used as ultrasound source. Acoustic source was placed at 27 mm distance from investigated sensor according the Figure 1. Arbitrary waveform generator Rigol DG1022 was placed into CW sine wave burst mode. Output voltage was 10 Vpp. The hydrophone signal was averaged by scope and peak negative voltage was registered. The obtained voltage was converted into pressure using (1). Refer Figure 7 for registered acoustic peak negative pressure AC response.

Actual transducer peak is at about 2.7 MHz. The obtained pressure was stored as reference.

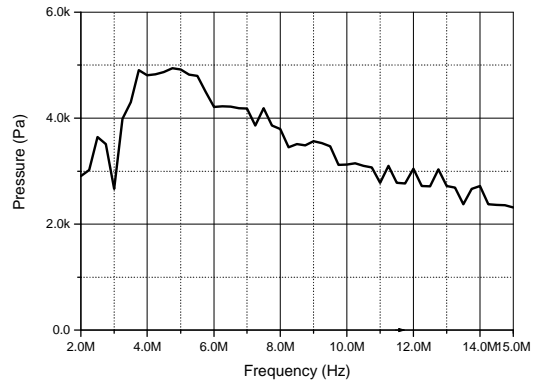


Figure 7. Peak negative pressure AC response for acoustic source

Then the pin transducer was placed at same location and the peak negative voltage on transducer registered. The voltage registered by pin transducer V_P was converted into sensitivity using the pressure P_h registered by hydrophone:

$$M_P(f) = \frac{V_P(f)}{P_h(f)} = \frac{V_P(f) \cdot M_c(f)}{V_h(f)}, \quad (2)$$

Results of obtained pin transducer sensitivity are presented in Figure 8.

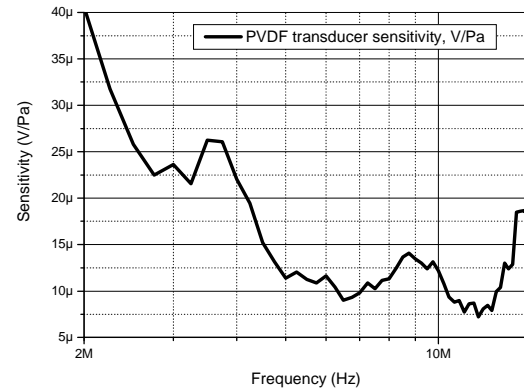


Figure 8. PVDF transducer sensitivity

It can be concluded that PVDF-based transducer has better sensitivity: almost 100 times higher, but the response is not as flat as the hydrophone (refer Figure 9 for comparison in dB).

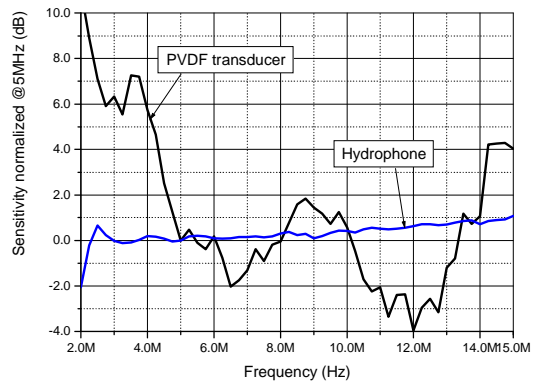


Figure 9. Sensitivity AC response comparison in dB @ 5 MHz

Another transducer, made from multilayered BaTiO₃ was investigated the same way (Figure 10).

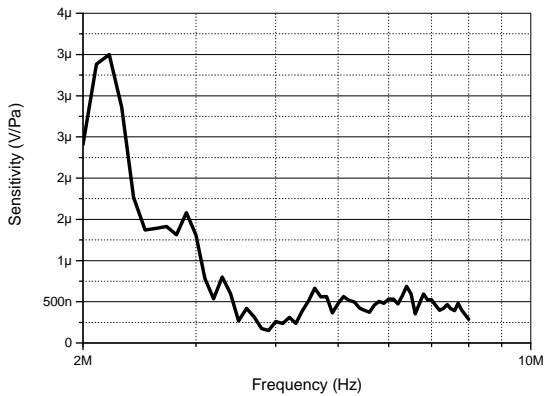


Figure 10. BaTiO₃ sensor sensitivity

This transducer has lower sensitivity than PVDF sensor and variation in frequency response is much higher (refer Figure 11 for sensitivity comparison normalized @ 5 MHz).

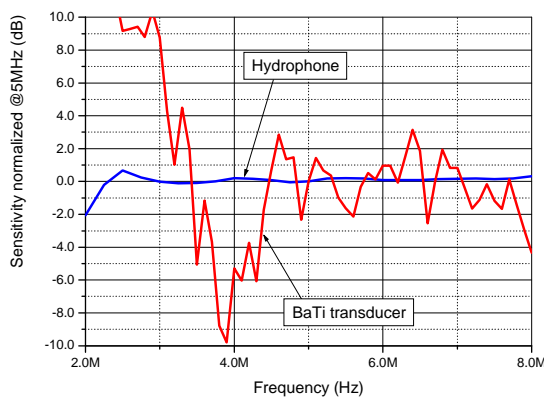


Figure 11. BaTiO₃ sensor sensitivity comparison in dB @ 5 MHz

Unfortunately, scope sensitivity was too low to register the signals reliably. Therefore signals at frequency range above 3 MHz were not stable to be registered. In future research the automated received voltage estimation has to be established. It can be done using sine wave correlation technique and automated acquisition system [10]. It can be seen that despite low sensitivity BaTiO₃ sensor also has acceptable sensitivity variation at higher frequencies within 3 dB. Sensitivity variation can be reduced using the damping of the backing layer.

5. Conclusions

Application of much cheaper pressure sensors AC response was studied. It has been concluded that measurements still can be carried out since sensors calibration is possible. Using commercial, wideband

hydrophone we were able to obtain the sensitivities for our sensors. After calibration, new sensors can be used instead of expensive hydrophone. Later, when rough estimation has been carried out using the cheaper sensors, final performance verification can be done using the expensive hydrophone. Such approach allows guarding the expensive hydrophone from possible damage during the extensive, long-lasting examinations. Future research should investigate the bandwidth improvement, AC response variation reduction techniques and better performance estimation equipment. Sensor linearity has to be investigated and compared against the commercial hydrophone.

6. Acknowledgment

Authors acknowledge Mykolas Ragulskis for his help with experiments on MLCC sensor. Also we express our gratitude to Stasys Burnovas for PVDF transducer design and fabrication.

References

- [1] K. O. Rove, K. F. Sullivan, E. D. Crawford, "High intensity Focused Ultrasound: Ready for Primetime", *Urologic Clinics of North America*, 2010, vol.37, pp. 27-35.
- [2] R. C. Preston, ed., "Output measurements for medical ultrasound". Berlin: Springer – Verlag 1991.
- [3] G. R. Harris, "Hydrophone measurements in diagnostic ultrasound fields," *IEEE Trans. on Ultras. Ferroel. and Freq. Control*, vol. 35, pp. 87–101, 1988.
- [4] R. E. Apfel, and C. K. Holland, "Gauging the likelihood of cavitation from short-pulse, low duty cycle diagnostic ultrasound", *Ultrasound in Med. and Biol.*, 1991, vol.17, pp.179-185.
- [5] Laghi, A. L. Baert, J. Brizuela, "New Concepts in Diagnosis and Therapy of Pancreatic Adenocarcinoma", Springer, 2011.
- [6] S. Ergun, "Analytical and numerical calculations of optimum design frequency for focused ultrasound therapy and acoustic radiation force", *Ultrasonics*, 2011, vol.51 pp. 786–794.
- [7] L. Sankauskas, R. Jurkonis. "Determination of focal zone of transducer by 3D acquisition of ultrasound field signals" *Proc.Int. Conf. on Biomedical eng.*, 2010, pp. 21-24.
- [8] "Converting from EOC sensitivity to amplifier-loaded sensitivity," Onda Corp., Sunnyvale, CA, USA.
- [9] *Certificate of Hydrophone Calibration*, Onda Corp., Sunnyvale, CA, USA, 30 September, 2008.
- [10] L. Svilainis, V. Dumbrava, A. Chaziachmetovas, "Universal acquisition system for frequency domain parameters measurement", in: *Proc. IEEE Conf. IDAACS'2011*, 2011, pp.10-15.
- [11] K.-R. Lin, et al., "Occlusive bite force measurement utilizing flexible force sensor array fabricated with low-cost multilayer ceramic capacitors (MLCC)", *IEEE conf. Proc. Transducers 2009*. pp. 2238 – 2241.

DESIGN AND SIGNAL PROCESSING OF A ECG RECORDER

Deyan M. Milev

*Faculty of Telecommunications, Technical University of Sofia, Bulgaria
1000 Sofia, "Kliment Ohridski" str.8
E-mail: dmilev@tu-sofia.bg*

Abstract

The paper presents an analysis on data input/output methods, standards for radio-communication in body sensor networks.

Long time digital data recordings in ambulatory devices have become possible today with the presence of high capacity flash memories.

In the second part a use-case scenario for remote monitoring of ECG and pulse rate is presented. To demonstrate the use of intelligent Bluetooth ECG is employed in described scenario.

1. Introduction

The modern technology offer far greater opportunities they can be easily programmed either online by connecting the device to a PC using Bluetooth technology or offline by inserting a pre-configured flash card. Wireless communication eliminates data transmission cable and allows to display real time ECG, in this way the appropriate electrode placement can be checked anytime even during the ECG session. The measurements are stored on a conventional SD/MMC flash card to avoid data loss. The ECG storage quality (diagnostic, holter, rhythm) and the size of the memory card can be chosen in order to meet the user's needs and achieve the best results.

2. Main text

In this context, data logging has a critical importance to make the patient's health history available to the health care provider. In implementing such patient treatment and monitoring equipments, researchers can design power-full medical devices with embedded processors that are easier to use, accessible and affordable. Implementation begins with the physiological interface to collect the signals from the human body. Using required front-end solution for essential signal conditioning, processor can perform further digital signal processing, meas-

urements, recordings and analysis to monitor patient condition. As well as short-term measurements long-term measurements can be recorded in massive data storage and they can be transferred to a computer workstation for advanced analysis. Over the last two decades, researchers have studied on developing some portable physiological data logging systems consisting of various analog signal conditioning and digital data processing solutions with different data recording capacities. These systems have been used generally in Electrocardiography (ECG) studies to detect infrequent cardiac arrhythmias or transitory cardiac function abnormalities. Several system designs have been described in this context. Some of them achieved the performance of commercial Holter recorders, systems that are named after an ECG recorder developed by N.J.Holter (1961), regarding the portability and nonvolatile data storage capacity. As a result of the developments in solid-state technology, researchers presently can implement such systems in a small and light structure with huge capacity of data storage. For instance, they can record the samples of physiologic signals in a flash memory card, Multi Media Memory Card (MMC) or Secure Digital Memory (SD) card. They can easily transfer the recorded data to a computer workstation for advanced signal analysis.

In this chapter we described such a microcontroller-based recorder design. It can be used as a reference model to build portable data logging systems. The design is powered by a NiMH battery. It integrates a microcontroller and its interfaces including a front-end unit for bio-signal conditioning. It provides recording capacity up to 1GB and sampling rate up to 1 kHz. Thus, it can be used for logging the data related to the various bio-signals. It includes off-the-shelf components and can be easily built with inexpensive components including an embedded microcontroller, PIC 18FXXX, from Microchip family. In this case, we used it to get the 500 Hz rated samples of ECG signal and evaluate them

for R-wave peak detection in QRS complexes, by using an on-line procedure. The system measure the interbeat times between the consecutive peaks, and records them into a file in the MMC/SD card recording media.

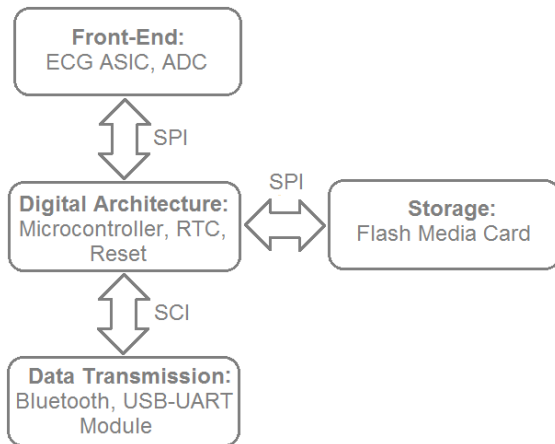


Figure 2-1. ECG Recorder Telemedicine System Block Diagram

The main function of this system is to acquire, store and transmit the ECG signals and provide mobility to the patient in two operation modes. First, in on-line transmission mobility is subject to a limited space, determined by the Bluetooth device class. Second, off-line acquisition is available through Holter operation mode. Therefore, this technology primarily designed for long-term usage in both modes [3].

Front-End: This block is for signal conditioning and digital conversion.

The function of this OEM Application Specific Circuit (ASIC), is to condition ECG signals from the electrodes. It also has the following characteristics: built-in pacer pulse detector, filtered lead-off for each electrode, programmable input offset for each channel, selectable reference electrode, on-chip RF filtering on all inputs and built-in self-test capability. This ASIC is configured through serial peripheral interface (SPI).

ADC: Digital conversion of the ECG differential channels is achieved through Analog Devices' analog to digital converter AD7716BS [1], with 4 independent and simultaneous delta-sigma sampling channels with 22 bits resolution. This ADC has 3 configurable sampling frequencies: 250, 500 and 1000 Hz. Samples from each channel, including channel and device address, are stored in 32-bit registers for later transmission. This device signals

each end of conversion through a pin connected to the microcontroller [11].

Digital Architecture: This stage is constituted by three main components: microcontroller, a real-time clock (RTC) circuit and a reset circuit. A microcontroller is used for setting the configuration of peripheral devices, processing and storing digital data acquired by the front-end, and establishing communication with local stations or APs through Bluetooth or USB. When the flash memory card is used, most of the processing time of μC is employed to update the FAT16 information in RAM and to communicate with the card. Therefore, the memory card and the front-end are connected to the μC through two different serial interface to ensure independence of the acquisition and storage process. Also, the end conversion pin of the ADC was connected to a high priority external interrupt to ensure that every set of samples was received with as little delay as possible. This set of samples is buffered awaiting its storage in the card. The 22-bit samples provided by the ADC can be stored and/or transmitted in both a 22-bit or 16-bit format, that is, data can be pre-processed in the μC to reduce storage and data rate requirements [1].

RTC: serial real-time clock used is a low-power clock/calendar with I2C bus interface for data transfer. The clock/calendar provides seconds, minutes, hours, day, data, and year information for recording identification purposes. Reset is used as a supervision circuit providing circuit initialization and timing supervision for the μC , to generate a power-on reset and power supply monitoring [4].

Storage: In this stage, collected data is stored in a flash memory card using FAT16 file format. Therefore, the memory card can be removed from this block for data retrieval in any computer-based platform. Each acquisition produces a new file with a simple protocol structure including sampling rate and lead configuration. Communication between the memory card and the μC is established through SPI bus. In the prototype, three different memory cards were tested since they share a common communication protocol: Multimedia Memory Card (MMC), Secure Digital Card (SD) and TransFlash [2].

Data Transmission: Two independent serial communication protocols are proposed: USB and Bluetooth. The four line SCI communication (RX, TX, RTS, CTS) go through a quad channel digital isolator.

Two AA batteries provide power to the model. A 95% efficiency step-up switching converter is used to generate 3.3V for system component. Exhaustive battery life-time measurement has not been carried out for all the operations modes. For a design estimate we considered the worst case for minimum battery life-time.

This condition occurs in two cases: Holter mode, which includes the SD and real-time transmission, which includes the Bluetooth module. In both cases, two 2500mAh AA batteries were assumed as power supply for the system.

In Holter mode, calculations were made using maximum current during memory writing and maximum and minimum writing times according to manufacturer's specification for both MMC and SD cards. A preliminary estimate suggests that battery lifetime should be at least 25 hours for MMC and 20 hours for SD cards.

3. Illustrations

Secure Digital Cards (SD) / Multimedia Memory Card (MMC), are used to hold information in many common electronic devices. SD/MMC cards can operate three different communication modes: one bit SD mode, four-bit SD mode, and SPI mode. SPI is a more basic protocol and it is widely supported by many microcontrollers.

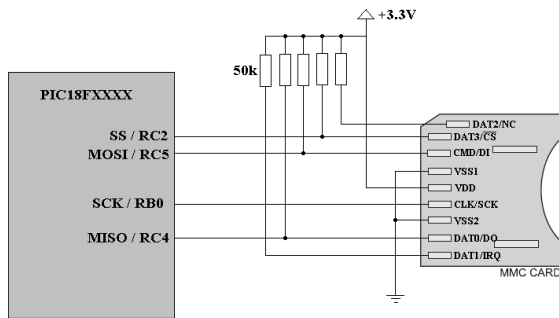


Figure3-1. Wiring Diagram for an SD Card

An SD card has 9 pins. Only 7 of these pins are used to communicate with an SD card in SPI mode. SD require between 2 and 3.6 VDC. In this case, I use power supply to provide 3.3 VDC to both the PIC and to the SD card. 50k pull-up resistors are essential, even for the pins that are not being used for SPI communications. Note that pull-up resistor should not be used on the clock line [5].

From Table 3-1, it is apparent that many SD Card pins are dual-purpose [6]. SPI is distinct from the 1-

bit and 4-bit protocols in that the protocol operates over a generic and well-known bus interface, Serial Peripheral Interface (SPI) [7]. SPI is a synchronous serial protocol that is extremely popular for interfacing peripheral devices with microcontrollers. Most modern microcontrollers support SPI natively high data rates. The SPI communications mode supports only a subset of the full SD Card protocol.

Pin	Name	Function (SPI Mode)
1	DAT3/CS	Chip Select/Slave Select (SS)
2	CMD/DI	Master Out Slave In (MOSI)
3	VSS1	Ground
4	VDD	Supply Voltage
5	CLK	Clock (SCK)
6	VSS2	Ground
7	DAT0/DO	Master In Slave Out (MISO)
8	DAT1/TRQ	Unused or IRQ
9	DAT2/NC	Unused

Table 3-1. SD Card Pin Assignments

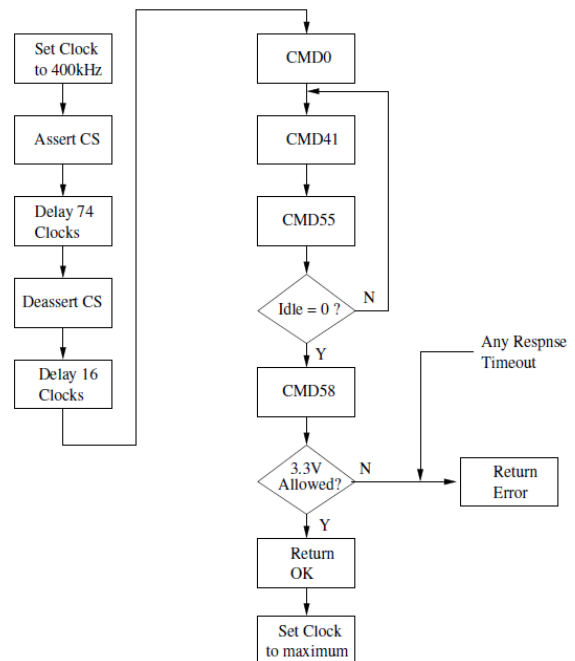


Figure 3-2. SD Card Initialization Sequence

The initialization sequence is characterized in the flowchart Figure 3-2 [8].

SD cards require a specific initialization sequence. Parts of the initialization sequence are historical, and other parts are required for backward and for-

ward compatibility. MMC and SD are not substantially different, the primary difference from a software point of view is in the initialization sequence. Card initialization starts by setting the SPI clock to 400kHz. This is required for compatibility across a wide range of MMC and SD Cards [9]. Next, at least 74 clocks must be issued by the master before any attempt is made to communicate with the card. This allows the card to initialize any internal state registers before card initialization proceeds. Next, the card is reset by issuing the command CMD0 while holding the SS pin low [10]. This both resets the card and instructs it to enter SPI mode. Note that while the CRC, in general, is ignored in SPI mode, the very first command must be followed by a valid CRC, since the card is not yet in SPI mode. The CRC byte for a CMD0 command with a zero argument is constant 0x95. Next, the card is continuously polled with the commands CMD55 and ACMD41 until the idle bit becomes clear, indicating that the card is fully initialized and ready to respond to general commands. Next, the command CMD58 is used to determine if the card supports the processor's operating voltage. CMD58 returns a bitfield containing the allowed operating voltage ranges, typically between 2.7V and 3.6V. It is assumed that the MSP430 is using a voltage supply of 3.3V. Finally, the SPI clock is set to the maximum rate allowed.

4. Conclusion

SD Cards offer a cost-effective way to store large amounts of data in a removable memory storage device. The simplicity of the SD Card protocol and the flexibility in interfacing with these devices makes them ideal for use with small microcontrollers. Combined with the low-cost, low power and its advanced features like onboard DMA and SPI, a fast and low-overhead complete data logging solution can be implemented quickly and inexpensively. Additional application-level support for a file system such as FAT16 can extend the usefulness of this solution even further.

References

- [1] Analog Devices "AD7716", Rev A, 1995 Available: http://analog.com/UploadedFiles/Data_Sheets/9287474ad7716.pdf
- [2] Jun Li, Sharp. Interfacing a MultiMediaCard to the LH79520 System-On-Chip, http://sharpsma.com/pub/productfocus/publications/micro/mcu/tec_appnote_LH79520_multimediacar.pdf
- [3] ScanDisk. Secure Digital Card Product Manual – Revision 1.7, September 2003.
- [4] Texas Instruments. MSP430x1xx Family User's Guide, <http://focus.ti.com/lit/slau049.pdf>
- [5] SD Card Association. <http://sdcard.org/>.
- [6] D. A. Peredina and A. Allen, "Telemedicine Technology and Clinical Applications," JAMA, vol. 273, 1995, pp. 483-88.
- [7] D. F. Leotta and Y. Kim, "Requirements for Picture Archiving and Communications Systems (PACS)," IEEE EMB Mag., vol. 12, Mar. 1993, pp.62-69.
- [8] F. Goeringer, "Medical Diagnostic Imaging Support System for Military Medicine", SPIE Medical Diagnostic Imaging IV: Image Capture, Formatting, and Display, vol. 1444, 1991, pp. 340-50.
- [9] American College of Radiology, National Electrical Manufacturers Association, "Digital Imaging and Communications in Medicine (DICOM): Version 3.0," Draft Standard, ACR-NEMA Committee, Working Group V], Washington, DC, 1993.
- [10] P. A. West, Private communication, Department of Family Medicine, University of Washington, Seattle, Aug. 1995.
- [11] M. A. Cawthon et al., "Preliminary Assessment of Computed Tomography and Satellite Teleradiology from Operation Desert Storm," Invest. Radiol., vol. 26, 1991, pp. 854-57.

PORTABLE EQUIPMENTS FOR REMOTE MONITORING OF HEART ACTIVITY IN TELEMEDICINE

Deyan M. Milev

*Faculty of Telecommunications, Technical University of Sofia, Bulgaria
1000 Sofia, "Kliment Ohridski" str. 8
E-mail: dmilev@tu-sofia.bg*

Abstract

In this paper we describe the software development of a 12-lead ECG.

The device is designed to capture the 12-lead ECG and transmit it via Bluetooth to a standard personal computer. The personal computer can then be used to store, display or print the recorded ECG.

The software was developed using Visual Basic and is designed to run on any device supporting the .NET Framework.

Further work is required to refine the developed software to support enhanced visualization and storage of the recorded data.

1. Introduction

Bluetooth technology is intended to replace the cables connecting portable and/or fixed devices while maintaining high levels of security.

A fundamental strength of Bluetooth wireless technology is the ability to simultaneously handle data and voice transmissions which provides users with a variety of innovative solution such as hands-free headsets for voice calls, printing and fax capabilities, and synchronization for PCs and mobile phones, just to name a few. The range of Bluetooth technology is application specific.

Bluetooth technology operates in the unlicensed industrial, scientific and medical (ISM) band at 2.4 to 2.485 GHz, using a spread spectrum, frequency hopping, full-duplex signal at a nominal rate of 1600 hop/sec. The 2.4 GHz ISM band is available and unlicensed most countries.

Bluetooth technology's adaptive frequency hopping (AFH) capability was designed to reduce interference between wireless technologies sharing the 2.4 GHz spectrum. AFH works within the spectrum to take advantage of the available frequency. This is done by the technology detecting other devices in the spectrum and avoiding the frequencies they are

using. This adaptive hopping among 79 frequencies at 1 MHz intervals gives a high degree of interference immunity and also allows for more efficient transmission within the spectrum. For users of Bluetooth technology this hopping provides greater performance even when other technologies are being used along with Bluetooth technology.

The EKG device detects and amplifies the tiny electrical changes on the skin that are caused when the heart muscle depolarizes during each heart beat.

Devices on the market that analyze ECGs, such as patient monitors, stress test systems, and holter analysis systems, do a good job of detecting beats and classifying arrhythmias.

This software implements the basic ECG analysis functions of beat detection and classification as C function. This release includes three version of beat detector. Two are general-purpose beat detection, where one represents a more efficient version with slightly different performance characteristics. The third beat detector is more computationally efficient, uses very little memory, and is embedded in a program that performs beat classification functions and may be used alone in applications that do not require beat classification.

2. Main text

Fig. 1-1 shows the basic operations of the beat detection algorithm. The beat detection algorithm can be broken down into two sections, the filters and the detection rules. This present release contains three versions of QRS detector. All three versions use the same filters and differ primarily in the details of the detection rules and code implementations.

The filters signal to generate a windowed (time limited) estimate of the energy in the QRS frequency band.

- Low pass filtering,

- High pass filtering,
- Taking the derivative,
- Taking the absolute value of the signal
- Averaging the absolute value an 80 ms window.

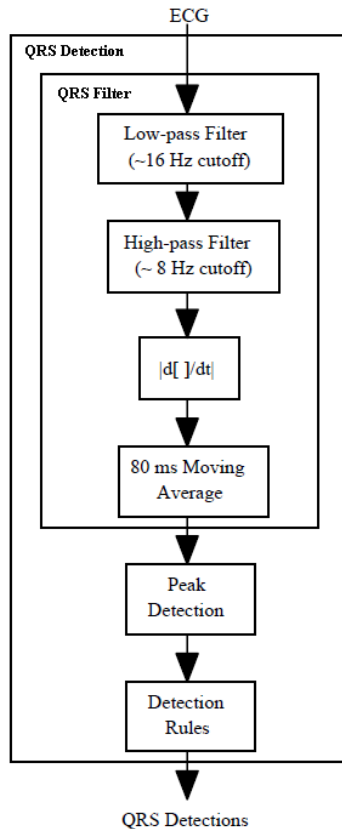


Figure 1-1. Beat detection operations

The final filter output produces what might be called a lump every time a QRS complex occurs. T-waves generally produce smaller lumps than QRS complexes. The high pass, low pass, and derivative combine to produce a bandpass filter with a pass band from 5 to 11 Hz, roughly the bandwidth that contains most of the energy in the QRS complex. The theory and implementation of these filters are detailed in [1], [2], and *Biomedical Digital Signal Processing* [3].

In [1] and [2], the filtered signal was squared rather than rectified. This operation caused the QRS detector to be somewhat gain sensitive. In this implementation I have used the absolute value, reducing the gain sensitivity and slightly improving the performance of the algorithm. The averaging windows was chosen to be roughly the width of a typical QRS complex. In the original algorithm this window was 150 ms wide to allow for the wide QRS complexes produced by Premature Ventricular Contractions (PVCs).

Since then, it has been shown that a narrower window produces better results [4].

After the signal has been filtered, QRS detects peaks in the signal. Each time a peak is detected it is classified as either a QRS complex or noise, or it is saved for later classification. The algorithm uses the peak height, peak location and maximum derivative to classify peaks. The following is an outline of the basic detection rules for the algorithm.

1. Ignore all peaks that precede or follow larger peaks by less than 200 ms.
2. If a peak occurs, check to see whether the raw signal contained both positive and negative slopes. If not, the peak represents a baseline shift.
3. If the peak occurred within 360 ms of a previous detection check to see if the maximum derivative in the raw signal was at least half the maximum derivative of the previous detection. If not, the peak is assumed to be a T-wave.
4. If the peak is larger than the detection threshold call it a QRS complex, otherwise call it noise.
5. If no QRS has been detected within 1.5 R-to-R intervals, there was a peak that was larger than half the detection threshold, and the peak followed the preceding detection by at least 360 ms, classify that peak as a QRS complex.

The rules as outlined above are implemented in QRSDet and detailed in [1] and [2].

The detection threshold used in 4 and 5 above is calculated using estimates of the QRS peak and noise peak heights. Every time a peak is classified as a QRS complex, it is added to a buffer containing the eight most recent QRS peaks. Every time a peak occurs that is not classified as a QRS complex, it is added to a buffer containing the eight most recent non-QRS peaks (noise peaks). The detection threshold is set between the mean or median of the noise peak and QRS peak buffers according to the formula:

$$\text{Detection_Threshold} = \text{Average_Noise_Peak} + TH * (\text{Average_QRS_Peak} - \text{Average_Noise_Peak})$$

where TH is the threshold coefficient. Similarly, the R-to-R interval estimate used in 5 is calculated as the median or mean of the last eight R-to-R intervals. Originally, I estimated average QRS peak values, noise peak values, and average R-to-R intervals using the median of the last eight values. The beat detector must begin with some initial threshold estimate. In order to make an initial estimate, I de-

tect the maximum peaks in eight consecutive 1-second intervals. These eight peaks are used as are initial eight values in the QRS peak buffer, I set the initial eight noise peaks to 0, and I set the initial threshold accordingly. I initially set the eight most recent R-to-R intervals to 1 second.

3. Illustrations

The proposed ECG telemedicine system is divided in several functional blocks: a DAM, an Access Point and local or remote station supporting telemedicine software application Figure 3-0. Firstly, the DAM is the device in charge of the acquisition, digitalization and processing of patient's ECG signals. Once the data is processed, it can be stored in a memory card for posterior inspection, or it can be wirelessly transmitted via Bluetooth to an AP or via USB to a local monitoring station [8].

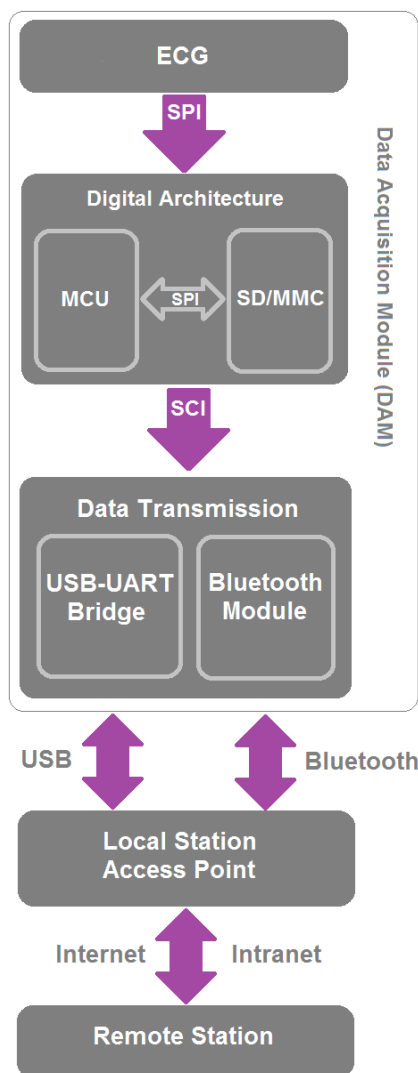


Figure 3-0

Secondly, the AP is a device located in a place near the patient which maintains connection between the DAM and the remote station via Internet/Intranet using TCP/IP. This connection could be continuous or event driven, t.e. when a risk situation is detected [9].

Finally, the local and remote stations run applications to visualize, analyze and store the information received from each patient.

UART interface is a standard 4 – wire interface with adjustable baud rates from 1200bps to 3Mbps [6].

3.1. Figure and table captions

Bluetooth supports multiple connections up to 4 slave units. There are two types of multiple connection modes: Multi-Drop Mode and Node Switching Mode.

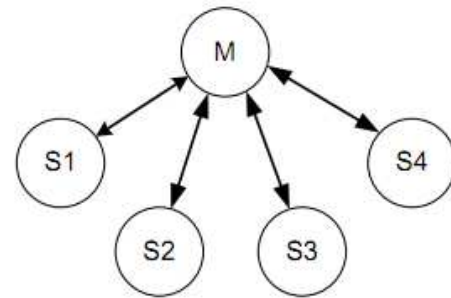


Figure 3-1. Multi-Drop Mode

In Multi-Drop Mode a master unit can connect to maximum 4 slave units at the same time and they transfer data bi-directional as in Figure 3-1.

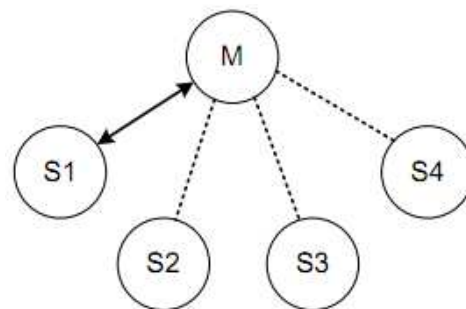


Figure 3-2. Node Switching Mode

In Node Switching Mode, the master unit maintains multiple connections with maximum 4 slave units but only one connection with one slave unit is active and data is transferred as shown in Figure 3-2.

Bluetooth compatibility is attained with an OEM module from BlueRadios, the BR-C30 Class 1[5]. This module is configured using AT commands and

accepts or establishes connections with other devices using Serial Port Profile (SPP) conforming to Bluetooth V1.2. The default communication baud rate is 115.2 kbps.

Performance at different sample rates—all filter lengths and time related constants scale with sample rate changes so that the constants and filter lengths are equivalent to the constants and filter lengths in the 200/100 samples-per-second implementation. Ideally, implementations at other sample rates would perform the same as the 200/100 samples-per-second implementation, but round off approximations in constants and filter lengths result in slight differences in performance [7].

Table 3-1 lists the sensitivities and positive predic- tivities for beat detection and beat classification for three combinations of base rate and beat rate.

Base Rate	Beat Rate	QRS Sens.	QRS +Pred.	PVC Sens.	PVC +Pred.
200	100	0.9975	0.9981	0.9371	0.9664
250	125	0.9974	0.9981	0.9359	0.9597
300	150	0.9974	0.9979	0.9303	0.9665

Table 3-1. Beat Detector and Classifier Performance at Different Sample Rates

Table 3-2 lists the sensitivities and positive predic- tivities for beat detection alone on a wider range of sample rates [10]. Performance differences only seem significant when the base sample rate is dropped as low as 100 or 125 SPS [11].

Sam. Rate	QRS Sens.	QRS +Pred.	QRS Sens.	QRS +Pred.
100	0.996856	0.997905	0.995839	0.996423
125	0.997426	0.998257	0.99666	0.996788
150	0.997458	0.998016	0.997429	0.997652
175	0.997601	0.998093	0.997119	0.997268
200	0.997426	0.998071	0.997397	0.997588
225	0.997228	0.997994	0.997268	0.997769
250	0.997502	0.99806	0.997087	0.9973
300	0.99736	0.998016	0.99745	0.997897
325	0.997448	0.997874	0.997578	0.997684
360	0.997535	0.998038	0.997503	0.997865

Table 3-2. Beat Detector Performance at Different Sample Rates

4. Conclusion

An 12-lead ECG telemedicine device for non-clinical applications has been successfully developed and tested for two particular functions: ecg-holter and on-line transmission. Since, all memory cards tested exceed the usual sampling rate for holter mode, the TransFlash was selected because it is smaller than the others. Further study will be carried out to test transmission reliability in the presence of a variety of standard consumer electronics, e.g. cordless phones and WiFi devices operating in the same frequency band that may adversely affect data transmissions via Bluetooth at different distances.

Furthermore, data compression algorithms will be studied to optimize memory card usage by reducing records size and power consumption due to data writing. Finally, an agent-based Java application is being developed to provide analysis and detection of arrhythmia using several vital-sign signals.

References

- [1] J. Pan and W.J. Tompkins, "A real-time QRS detection algorithm," *IEEE Trans. Biomed. Eng.*, vol. BME-32, pp. 230-236, 1985.
- [2] P. S. Hamilton and W. J. Tompkins, "Quantitative investigation of QRS detection rules using the MIT/BIH arrhythmia database," *IEEE Trans. Biomed Eng.*, vol. BME-33, pp.1157-1165, 1986.
- [3] Tompkins WJ (ed.). *Biomedical Digital Signal Processing: C-Language Examples and Laboratory Experiments for the IBM PC*. 1993. Englewood Cliffs, NJ: PTR Prentice Hall.
- [4] Wieben, O., Tompkins W.J., Afonso, V.X., "Classification of PVCs with a fuzzy logic system," *Proceedings-19th International Conference-IEEE/EMBS*, pp. 65-67, 1997.
- [5] BlueRadios, "BR-C30 Class1, Class2, and Class 3 Bluetooth ver1.2", 2005. Available: <http://www.blueradios.com/BR-C30.pdf>
- [6] Welch Allyn OEM Technologies, "ECG/Respiration ASIC: ECG 3-lead, 5 lead, 12-lead and RESP Signal Processing", (11/09/2003).
- [7] S. Yu, J. Cheng, "A Wireless Physiological Signal Monitoring System with Integrated Bluetooth and WiFi Technologies", *Proceedings of the 2005 IEEE Engineering in Medicine and Biology 27th Annual Conference* Shanghai, China, September 1-4, 2005.
- [8] C. S. Patichis, E. Kyriacous, S. Voskarides, M. S. Pattichis, R. Istepanian, and C. N. Schizas, "Wireless telemedicine systems: an overview," *IEEE An-*

- tennas Propag. Mag.*, vol. 44, Apr. 2002, pp.143-153.
- [9] A. Hernandez, F. Mora, G. Villegas, G. Passariello, and G. Garrault, "Real-Time ECG Transmission Via Internet for Nonclinical Applications", *IEEE Trans. Inform. Technol. Biomed.*, Sept. 2001, pp. 253-257.
- [10] Moody, G.B., Mark, R.G., "Development and evaluation of a 2-lead ECG analysis program," *Computers in Cardiology*. 1982; 39-44.
- [11] J. L. Urrusti and W. J. Tompkins, "Performance evaluation of an ECG QRS complex detection algorithm," *Proc. Annual International Conference of the IEEE Engineering in Medicine and Biology Society*, pp. 800-801, 1993.

USING GENETIC ALGORITHM FOR ROUTING

Valentin Hristov^{*}, Boris Tudjarov^{}**

^{}Department of Computer Systems and Technology at South West University
66, Iv. Mihajlov, 2700 Blagoevgrad, Bulgaria
E-mail: v_hristov@swu.bg*

*^{**}Department of Design Fundamentals, Technical University – Sofia
8, Kl. Ohridski blvd, 1000 Sofia, Bulgaria*

Abstract

The present paper presents a program for Routing based on Genetic Algorithms. The most popular routing protocol is Open Shortest Path First- OSPF based on finding a minimum-length (cost) route between a given pair of nodes. It was proposed by Dijkstra and has been widely researched. The Dijkstra algorithm is considered as the most efficient method but when the network is very big, then it becomes inefficient since a lot of computations need to be repeated. Also it can not be implemented in the permitted time. The purpose of present paper is to propose a program based on genetic algorithm which to solve above problem as looking for routes with minimum cost between source and destination.

Keywords – Genetic Algorithms, Open Shortest Path First - OSPF.

1. Introduction

Nowadays the most popular routing protocol is Open Shortest Path First- OSPF based on finding a minimum-length (cost) route between a given pair of nodes. It is based on the Bellman optimization theory. But when the network is very big, then it becomes inefficient since a lot of computations need to be repeated. Also it can not be implemented in the permitted time.

The purpose of present paper is to propose a program based on genetic algorithm which to solve above problem as looking for routes with minimum cost between source and destination.

2. Genetic Algorithms

The biological foundations of the genetic algorithms (GA) are explained very briefly below.

The complete set of genetic material (all chromosomes) is called genome. Chromosomes consist of genes, blocks of DNA, each gene encodes a specific protein.

During the reproduction, the genes of the parents formed an entirely new chromosome by recombination (or crossover). New produced offspring then undergo mutation, i.e. elements of DNA change. Adaptability of the organism is measured by the success in his life.

GAs are used when pursuing a specific result (objective), when the solution requires a relatively large time resource or in cases where the solution is not known or has no solution. Algorithm starts with a set of solutions (represented by chromosomes with specific information about genes) called initial population. According to their viability are chosen solutions to form the next population (offspring). To more appropriate decisions (decisions are compared in terms of pursued result/goal) are given better chances for reproduction. New population is expected to be better than the old. This is repeated until some condition (for example: a number of generations or a sufficiently good solution) is satisfied.

The sequence in the genetic algorithm can be represented as follows:

- 1) generate initial random population of n chromosomes (solutions);
- 2) calculating the viability $f(x)$ of each chromosome in the population n (in the target function - called "fitness function") and identification of chromosomes with priority for the next population (m in number, $m < n$);
- 3) establishing a new population by repeating following steps until the new population is completed:
 - 3.1) preserving the predetermined number m of the best solutions (according to their fitness - the fitness function values);
 - 3.2) election of two parental chromosomes of m chromosomes;
 - 3.3) using of crossover to cross the parents to form the next generation (children);

3.4) using of mutation to mutate the newly created chromosomes;

3.5) pasting the new generation in the new population (adding n-m new chromosomes and filling the population);

3.6) replacement- using newly generated population for the further implementation of the algorithm;

4) stop and return the report if the final check-condition is satisfied;

5) loop, go to step 2).

In [1], [2], [3] are represented several interactive Java applets for the demonstration of the performance of genetic algorithms.

3. Program using Genetic Algorithm for Routing

As a special kind of stochastic search algorithms, genetic algorithm is a problem solving method which is based on the concept of natural selection and genetics. Genetic algorithms are inspired by Darwin's theory about evolution. Algorithm is started with a set of solutions (represented by chromosomes) called population. Solutions from one population are taken and used to form a new population. This is motivated by a hope, that the new population will be better than the old one. Solutions which are selected to form new solutions (offspring) are selected according to their fitness - the more suitable they are the more chances they have to reproduce. This is repeated until some condition (for example number of populations or improvement of the best solution) is satisfied. The space of all feasible solutions (it means objects among those the desired solution is) is called search space. Each point in the search space represents one feasible solution. Each feasible solution can be "marked" by its value or fitness for the problem. We are looking for our solution, which is one point among feasible solutions - that is one point in the search space.

Figure 1 shows the Source code of proposed program (in Python Programming Language).

When initializing the population, proposed algorithm starts from the SOURCE. The algorithm selects one of the neighbours provided that it has not been picked before. It keeps doing this operation until it reaches to DESTINATION. Both SOURCE, and DESTINATION are constants that user may change as they wish. If we are solving above problem, we

are usually looking for route, which will be the best among others.

The evaluation function takes a path in the population. It gets the distance between each node pair in the path, by calling a function to read from the distance array. Adds them together and returns the sum as the cost of the path.

The program selects two individuals from the population with the lowest costs.

The crossover function takes two parents to mate. It looks for the common points in the parents. The common nodes are where these two paths intersect. Among the common points, the program selects one of them randomly. It makes the crossover from that point.

The search space can be whole known by the time of solving a problem, but usually we know only a few points from it and we are generating other points as the process of finding solution continues. The evaluation function takes a route in the population. If the offsprings' fitnesses are less than the nodes with maximum fitnesses in the population, we replace them with the nodes with the maximum fitnesses.

An experiment is developed and realized. The network topology has 20 nodes connected with 62 links as in [6]. We set two nodes as source and destination. Each link has a cost associated with them. The costs on the links are stored in matrix 20x20 (dist.txt). In this matrix, the cells with 10,000 in them represent that there is no direct link between those nodes. The program uses also a file (parents2.txt) with initial population [7].

We run the steps selection, crossover, and replace part 50 times i.e. number of generations

(Crossover probability is chosen 0.99 and mutation probability- 0.1).

On Fig. 2 is represented a part of generated, after calculations, report and more precisely path cost (the minimum, maximum, and average numbers) versus number of generations. As it can be seen from the Fig.2 the program gets close to optimum very quickly.

```

class GA:
    #Read the files with info about the first population and the scoring
    #
    def get_info(self, file1, file2, separator):
        try:
            f1 = open(file1, 'r')
            f2 = open(file2, 'r')
            f1 = f1.readlines()
            f2 = f2.readlines()
        except Exception, ex:
            print "Error ", ex
        population = [(1,2,3,6), (1,4,5,6), ...] * (n/length)
        score = [(1000,1,2,1,2,3), (2,1000,2,1,2,1), ...] * (n/n)
        for i in range(len(population)):
            population.append((20), split(separator))
        for i in range(len(population)):
            population[i][1] = int(population[i][1])
        for i in range(len(f1)):
            score_table.append(f1[i].split(separator))
        for i in range(len(score_table)):
            for j in range(len(score_table[i])):
                score_table[i][j] = int(score_table[i][j])
        return [population, score_table]

    #Calculate the score of one individ
    # Input - the individ, the table with scores
    def score_func(self, pop, score_table):
        score = 0
        for i in range(len(pop)-1):
            try:
                x = pop[i]
                y = pop[i+1]
                score = score + score_table[x][y]
            except: print "Error"
        return score

    def avg(self, Top_scores, population_count):
        score_sum = 0
        for i in range(population_count):
            score_sum += Top_scores[i]
        return score_sum / float(population_count)

    def build_generation(self, population, score_table):
        a = GA()
        population_count = len(population)
        scores = [] #list with scores of the indivs and their number -> score[number, score points]
        for i in range(population_count):
            scores.append(a.score_func(population[i], score_table))
        Top_scores = sorted(scores, key=lambda i: (i[1], reverse=False))

        [n, len(scores)]
        new_population = []
        counter = 0

```

```

# crossover tuples
while counter < population_count - 1:
    ind1 = population[Top_scores[counter][0]]
    ind2 = population[Top_scores[counter + 1][0]]

    for i in range(1, len(ind1)-1):
        for j in range(1, len(ind2)-1):
            if ind1[i] == ind2[j]:
                check = True
            for ii in range(1, len(ind2)-1):
                for jj in range(i+1, len(ind2)-1):
                    if ind1[i] == ind2[jj]: check = False

            if check:
                child = ind1[:i]+ind2[i:]
                if child not in new_population:
                    new_population.append(child)
            else:
                check = True

        try:
            for ii in range(1, len(ind1)-1):
                for jj in range(i+1, len(ind1)-1):
                    if ind2[ii] == ind1[jj]: check = False

            if check:
                child = ind2[:ii]+ind1[ii:]
                if child not in new_population:
                    new_population.append(child)
        except: print

        counter += 2
        counter = population_count - 1

    #Generate the next generation
    for i in new_population:
        if i not in population:
            counter += 1
            population.append(i)
            scores.append((counter, a.score_func(i, score_table)))

    Top_scores = sorted(scores, key=lambda i: (i[1], reverse=False))
    print 'min : ', Top_scores[0][1], ' max : ', Top_scores[4][1], ' avg : ', self.avg(Top_scores, population_count), '\n'
    next_generation = []

    try:
        if len(Top_scores) > population_count:
            for i in range(population_count):
                next_generation.append(population[Top_scores[i][0]])
        print next_generation[0]
        return next_generation
    except Exception, ex: print "Error ", ex

def run(self, gen_num, dist = dist.txt, par = 'parents2.txt', separator = '\n'):
    population, score_table = self.get_info(dist, par, separator)
    for generation in range(gen_num):
        population = self.build_generation(population, score_table)

if __name__ == '__main__':
    ga = GA()
    ga.run(10)

```

Fig.1. Source code of proposed program

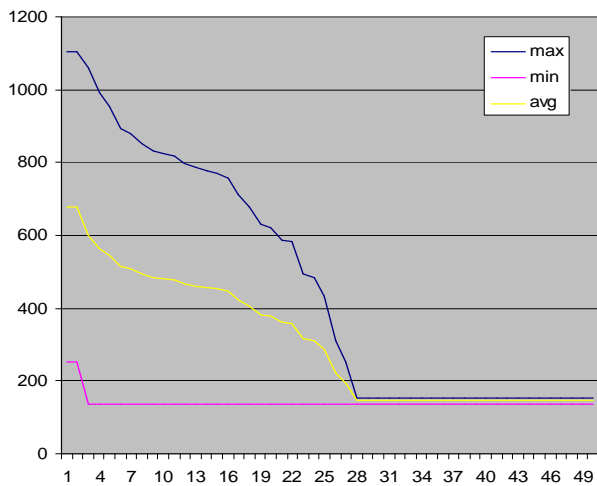


Fig. 2. Path costs versus number of generations

4. Conclusion

In present paper, we propose a program based on genetic algorithm which efficiently solves the routing problem in computer networks and more precisely looking for routes with minimum cost between source and destination.

References

- [1] Туджаров Б., В. Пенчев, В. Христов, XML Моделиране на генетични алгоритми, Българско списание за инженерно проектиране, брой 8, март 2011г, с.75-80.
- [2] Tudjarov B., N. Kubota, V. Penchev, V. Hristov, Web based Modeling and Calculation of Genetic Algorithms, Proceedings of the IWACIII'2011, China (accepted).
- [3] www.obitko.com (accessed February 18, 2011).
- [4] www.php.net (accessed February 18, 2011).
- [5] cisco.netacad.net (accessed September 2, 2011).
- [6] http://www.bilalgonen.com/research/publications/GA_shortest_path_BilalGonen.pdf (accessed September 2, 2011).
- [7] cst.swu.bg/~vhristov/GA_for_Routing.zip (accessed September 2, 2011).

ELLEIEC PROJECT A COMPARATIVE EVALUATION OF TEACHING PRACTICES IN EUROPA – RECOMMENDATIONS AND BEST PRACTICES

Samuel NOWAKOWSKI, Nathalie BERNARD-ISSENMANN

*PRES de l'Université de Lorraine, NUTICE
34 cours Léopold
54056 Nancy, FRANCE
Samuel.nowakowski@nancy-universite.fr
Nathalie.bernard@nancy-universite.fr
Hamed YAHOU
Université Claude Bernard Lyon 1
41, Boulevard Andre Latarjet
69622 Villeurbanne, FRANCE
hamed.yahoui@univ-lyon1.fr*

Abstract

In this paper, we are going to present the methodology we have adopted to propose recommendations for e-Learning related to the objectives of ELLEIEC project. First, we present the general context and then, we expose the different steps of the study which lead to e-Learning recommendations for the Virtual Entrepreneurship Center.

Keywords: *eLearning; comparative assessment; best practices*

1. Introduction

ELLEIEC (Enhancing Lifelong Learning for the Electrical and Information Engineering Community) is an ERASMUS thematic network which is funded by the European Commission for a three-year period (October 2008-September 2011). ELLEIEC will establish, as main output, a virtual centre for the development of enterprise skills and competencies and investigate and report on the implementation issues and impact of Lifelong Learning on the employability of people over Europe in the Electrical and Information Engineering field. The virtual centre will connect learners of any age to a network of educators within academic institutions, business training advisory bodies and business mentors across Europe. The Virtual Centre for enterprise will provide a facility through which any learner within Europe can develop their enterprise skills and hence the centre will contribute to the competitiveness of the population in new venture creation and the economic growth of the European Union. Engagement of staff and learners with the Centre will

also contribute to the excellence of European education and research in the enterprise area. ELLEIEC will provide a guideline for an internal e-learning assessment offer which will be a reference point for any applicant in the Lifelong learning framework. Finally ELLEIEC will test some mobility network to promote mobility through the studying of good practice in the design of International cooperation at PhD, master and bachelor levels with attractive application. A methodology for an assessment of eLearning enterprise courses compared to more classical delivery methods, to define a valuable e-learning tools.

In task V, ELLEIEC project have the aim to develop a methodology for an assessment of e-learning enterprise courses compared to more classical delivery methods, as well as to participate in the quality assessment of e-learning tools and in effort to define some valuable e-learning tools for course delivery.

The objectives were to submit a common questionnaire to different populations of students to evaluate teaching/learning process. The evaluation will explore many cases as :

Assessment of knowledge, skills and competence obtained by student during the learning process

- Identification of differences while using traditional teaching methodology and using e-learning tools and appropriate methodology.
- Evaluation of satisfaction, motivation, enjoyment, etc.

- Self-evaluation of achievements in learning process while using e-learning tools and appropriate methodology in comparison with traditional teaching.

2. Methodology

To achieve the main objectives of Task V, we have established the following milestones:

- state of the art concerning eLearning and the existing comparisons between the delivery methods
- state of art in terms of good practices, guidelines and existing projects in the field of eLearning
- design of the questionnaire taking into constraints coming from the involved partners (from the technical and methodological points of view)
- online survey and analysis of the results
- recommendations for the VCE.

Hereby, a figure which summarizes the main step and their interactions to achieve the objectives of the task.

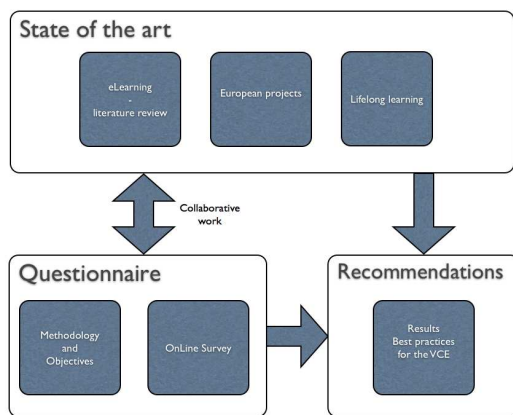


Figure 1. Task V – Milestones

A. State of the art

Our state of the art had to fulfill some specific constraints. First, because of the baseline of the task (comparative study of learning delivery methods), we have identified the need to have a common literature review and a shared knowledge of the important actors and actions in the field of eLearning for each partner country. Second, we have to design a specific questionnaire with an adapted methodology which will give us the possibility to compare all types of experiments from eLearning to face-to-face including specific tools (Tablet PC, ePortfolio, funded by the European Commission

Users Response Systems) and blended learning. This questionnaire will be discussed in the next part. Third, to be aware of the works done in others projects or studies, we need to have a common basis of references (bibliography, list of projects). These references will enrich the collaborative work which lead to the recommendations for the VCE. At least, using the results of the comparative analysis using the questionnaires and the best practices identified in the state of the art, Task V team will recommend some important features for the VCE.

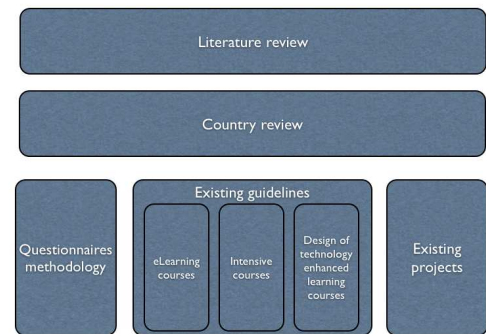


Figure 2. State of the art – Structure

B. Experiments

Each partner will contribute to the comparative study by bringing their own pedagogical experiences (see table 1). The objective is to have a large variety of:

- pedagogical approaches (eLearning, blended learning, face to face, technology enhanced learning),
- technology used (Users Response Systems, Tablet PC, ePortfolio, LMS),
- students (different levels, different domains, different countries, ...).

These experiments were performed during year 2010/2011. Others experiments were organized in year 2009/2010 but the questionnaire was not adapted. The feedback of these first experiments has given new tracks to design the question which is currently used.

Table 1. Experiments

Type of Experiments	Universities	Domains	Number of involved students	% of eLearning
A Practice in Using ePortfolio in a Higher Education Course Taught at Distance	Ege university, Izmir, Turkey	Object Oriented Programming	22 students: 7 undergrad, 15 grad	50

Enhancing learning by using Tablet PCs in a networked classroom	Universidad Politécnica de Valencia, Spain	Electronic Algorithms and Data structure	20-20 / 30	50
CISCO Courses	University of Rousse, Bulgaria	Network	15	100
MEDICAL INFORMATION SYSTEMS Handbook for Laboratory Exercises and Self testing@	University of Sofia, Bulgaria	Information Technology in Medicine	180/year	50
Blended Learning in Guided Propagation and Antennas	IST-UTL Lisbon, Portugal	Telecommunication	70	15
LMS	Kaunas University	Biomedical Digital Processing	20	60
eLearning versus classical one	Joseph Fourier University, Grenoble, France	Network and Telecommunications	5	50

Taking into account the feedback of the use of the first questionnaire, the current questionnaire is the results of a collaborative work between all the partners involved in Task V. The main constraint was the questionnaire would be used for all the experiments. The questions had to fit as well for eLearning experiments as face-to-face or blended learning.

The questionnaire is structured by the following main parts:

Table 2. Structure of the questionnaire

Main categories	Details
Institutions	Which country, town, university,
Personal informations	Gender, age, domain, level, year in bachelor or Master
Tools	Evaluation of the usability (scale 1 to 5 from strongly disagree to strongly agree)
	I think this tool is easy to use I was able to learn this tool quickly The tool operated correctly The tool interface is attractive
	Evaluation of the effectiveness (scale 1 to 5 from strongly disagree to strongly agree)
	The tool was helpful to achieve my learning goals This tool was useful enough to complete learning tasks

	Evaluation of the satisfaction (scale 1 to 5 from strongly disagree to strongly agree)
	I was satisfied with the tool
	Evaluation of the productivity (scale 1 to 5 from strongly disagree to strongly agree)
	The tool helps me to finish tasks in shorter time comparing other tools
Methods	Evaluation (scale 1 to 5 from strongly disagree to strongly agree)
	My profeciency in using this tool is good I am satisfied with this methodology of learning I learned the course material better with this approach The pedagogical method helps me monitoring my own learning The pedagogical method engages me more in the course work I needed instructor's help in following the course material The pedagogical method helped me to improve creativity The pedagogical method motivated me to interact more with my teacher and the other students The pedagogical method enabled collaborative work with the other students I put more time for learning the course material than traditional class
Perspectives / Expectation	Evaluation of the expectation (scale 1 to 5 from strongly disagree to strongly agree)
	My expectations at the beginning of the course were very high
	Evaluation of the satisfaction (scale 1 to 5 from strongly disagree to strongly agree)
	The course approach has met my expectations Overall, I was satisfied with this course approach I would recommend this approach for other courses
ECTS evaluation	Evaluation
	How many hours have you spent to complete this course (lecture, assignment, home work with other resources) ? In order to complete the course, how much time have you spent using others resources (books, library, internet, ...) not included in the regular material ?
Experience in learning technology	Evaluation
	User Response Systems, ePortfolio, TabletPC, PPT, LMS, onLine tests, ...
Personal informations	How frequent do you use computer ?

	Do you own a personal computer ? Do you have an internet connection ? How frequent do you use your computer ? Since when, do you have an internet connection ?
--	---

These main parts have been chosen to be filled by any student what ever the experiment. The questionnaire counts 45 questions and has been implemented in LimeSurvey to have onLine survey and statistical functionalities.

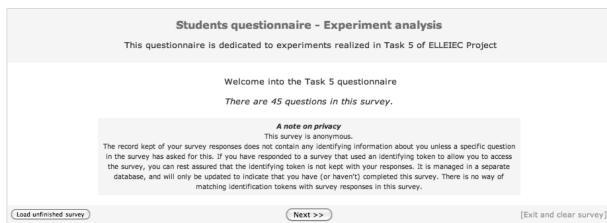


Figure 3. onLine survey – Homepage

Some informations concerning the in progress survey:

- 73 students have answered to the questionnaires from France, Spain, Portugal, Bulgaria, Turkey and Lithuania.

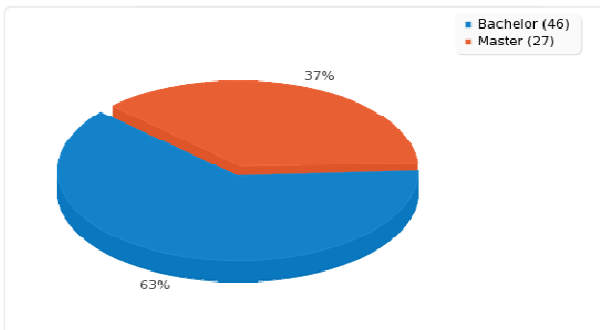


Figure 4. onLine survey – Levels

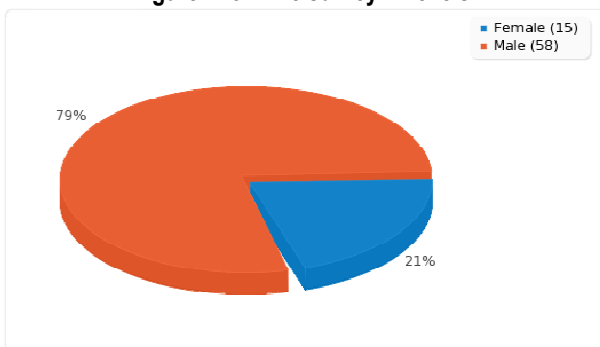


Figure 5. onLine survey - Genders

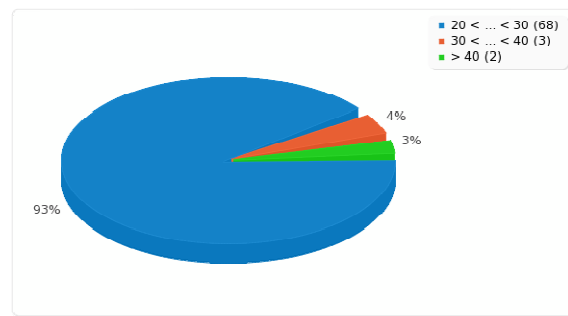


Figure 6. onLine survey – Ages

3. Recommendations

Following the results of the state of the art and the analysis made during the experiments, we have identified some key points to be considered for the design of the VCE. These key points are the following :

- tutoring
- delivery
- design
- assessment
- learning styles

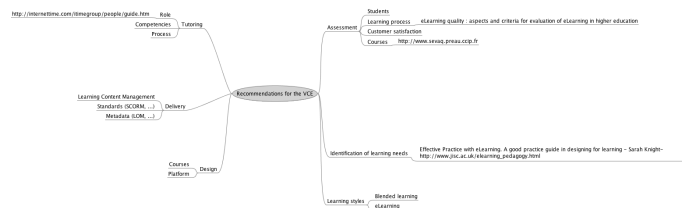


Figure 7. Mindmap including main recommendations

4. Conclusion

In this paper, we have described the activities led in Task V of ELLEIEC project. This Task dedicated to eLearning from the points of the technologies, the methodologies, the assessments methods, the used tools, the partners experiences is the task which proposes to the whole projects her competencies in eLearning. With the work done, all the partners of the project will have a sort of handbook summarizing important references, how-to to start with eLearning, and recommendations and guidelines which help them in their own eLearning strategies.

Acknowledgment

The authors would like to thank all the partners involved in task V activities.

Nina Bencheva, Yoana Ruseva, Bahar Karaoglan, José V. Benlloch-Dualde, Milcho Manev, Carlos Vaz de Carvalho, Maria Joao Martins, Romanas Krivickas, Dorin Popescu, Laszlo Komaromi, Juan José Marcuello Pablo, Ilmars Slaidins, Michael Hoffmann, Dimiter Dimitrov, Ismo Hakala, Maciel Barbosa

References

- [1] Barrett, H. C. (2009). Electronic Portfolios – A chapter in Educational Technology: An Encyclopedia to be published by ABC-CLIO 2001. (<http://www.helenbarrett.com/portfolios/encyclopedia/entry.htm>).
- [2] Bilén S.G. et al. (2009). Tablet PC Use and Impact on Learning in Technology and Engineering Classrooms: A Preliminary Study. Workshop on the Impact of Pen-Based Technology on Education, pp. 11-19.
- [3] Blackboard Learning System, (www.blackboard.com).
- [4] Bonk, C. J., Graham, C. R., (2005). Handbook of blended learning: Global Perspectives, local designs. San Francisco, CA: Pfeiffer Publishing.
- [5] Border, J., Stoudt, K. and Warnock, Mary. (2006) E-Learning Concepts and Techniques, (http://iit.bloomu.edu/Spring2006_eBook_files/chapter4.htm#h4_2).
- [6] Britain, S. and Liber, O. (2004). A Framework for the Pedagogical Evaluation of eLearning Environments. (http://www.cetis.ac.uk/members/pedagogy/files/4thMeet_framework/VLEfullReport).
- [7] Chen, C., Jones, K. (2007). Blended Learning vs. Traditional Classroom Settings: Assessing Effectiveness and Student Perceptions in an MBA Accounting Course, The Journal of Educators Online, January 2007, Volume 4, Number 1
- [8] Drewitz, I., (2009). Evaluation of e-learning platforms, mSysTech, (http://www.eworks.de/research/2009/03/Evaluierung-E-Learning-Plattformen/Evaluation_of_e-learning_platforms.pdf).
- [9] Gray Harriman Ltd. (2010). E-Learning Resources, (<http://www.grayharriman.com/index.htm>).
- [10] Hristov, Ts. (2009). Implementation and investigation of a WEB-Based eLearning Software Platform, PhD thesis.
- [11] Koile, K., Singer, D. (2008). Assessing the Impact of a Tablet-PC-based Classroom Interaction System. Monograph of the 3rd Workshop on the Impact of Tablet PCs and Pen-based Technology on Education. Evidence and Outcomes, Purdue Univ., West Lafayette, Indiana, USA, pp. 73-80.
- [12] Kolás, L., Staupe, A. (2010). Implementing delivery methods by using pedagogical design patterns, (<http://www2.tisip.no/E-LEN/papers/EDMEDIA04/SymposiaNTNU.pdf>).
- [13] Maguire, C., Zhang, J. Working Paper "Effective Blended Learning for Development, Tokyo Development Learning Centre, (<http://www.jointokyo.org/en/>).
- [14] Microsoft® Class Server Solution Review, (<http://www.microsoft.com/education/classserver.msp>).
- [15] Mougalian, C., Matesol, S., (2006). Moodle, the electronic syllabus, lends itself to ProCALL, (<http://faculty.miis.edu/~bcoble/CALLme/page2/page9/page9.html>).
- [16] Ng, E. M.W. (2010). Extending Learning to Interacting with Multiple Participants in Multiple Web 2.0 Learning Communities. (<http://iisit.org/Vol7/IISITv7p011-023Ng769.pdf>).
- [17] O'Hear, S., e-learning 2.0 - how Web technologies are shaping education, (http://www.readwriteweb.com/archives/e-learning_20.php).
- [18] Rashty, D. Traditional Learning vs. eLearning, Mount St. Mary's College. (http://www.msmc.la.edu/include/learning_resources/).
- [19] Richardson, W. (<http://weblogg-ed.com/>).
- [20] Sneller, J. (2007). The Tablet PC classroom: Erasing borders, stimulating activity, enhancing communication. proceedings of the 37th ASEE/IEEE Frontiers in Education Conference, 2007 © IEEE. doi: 10.1109/FIE.2007.4417929.
- [21] TjTaylor Ltd. Corporate English Language Training, (<http://www.tjtaylor.net/english/elearning-online-and-blended.htm>).
- [22] Wall, J., Smith, et al. (2005). An International Comparison Of eLearning In Action – An Interactive Graphical on Line Teaching Resources for Residential Construction in Australia and a Blended Programme to Support Irish Entrepreneurs in Ireland. In: QUT Research Week 2005, 4-5 July 2005, Brisbane.
- [23] Zhang, D., et al. (2004). Can E-learning Replace Classroom Learning? Communications of the ACM May 2004, Volume 47 No 5, pp. 74-79.

SEGMENTATION OF NEURO MR IMAGES THROUGH SEMI-SUPERVISED LEARNING

Vladimir H. Kanchev¹, Ivo R. Draganov², Antoaneta A. Popova^{3*}

^{1,2,3}Radiocommunications and Videotechnologies Dept.

Technical University - Sofia

8 Kliment Ohridski Blvd., 1000 Sofia, Bulgaria

Tel.: +359 2 965 2274, E-mail: {v_kanchev, idraganov, antoaneta.popova}@tu-sofia.bg

Abstract

In this paper an algorithm is presented for segmentation of degraded and healthy tissue from neuro images of patients who suffered from AD, MCI, and healthy ones. We construct a model of 3D region mask and then imposed it on the test neuro images for segmentation. During training neuro images of AD and healthy patients are subjected to the following operations: pre-processing, brain extraction, image registration to an atlas, tissue segmentation and then classifier is applied in order to create a 3D mask. During segmentation white, grey matter and CSF are separated by Fuzzy C-means clustering. After that we perform feature extraction, estimation of statistics of 3D mask region in the test image.

Key-words: segmentation of neuro images, semi-supervised learning, Alzheimer's disease, clustering

1. Introduction

Alzheimer's disease (AD) is an incurable, degenerative and terminal disease that affects more than 5 million Americans now and it is estimated that 13 million elderly will be diagnosed by AD in the 2050 year in the US alone [1].

We should first distinguish AD, Mild Cognitive Impairment (MCI), and dementia. AD is a progressive neurodegenerative disorder associated with a disruption of neuronal function and a gradual deterioration in cognition, function, and behaviour [2], MCI describes and early, but abnormal state of cognitive impairment in which people continues to do well in their daily activities [3]. Dementia is a serious loss of cognitive ability in a person, beyond what is expected from their age.

AD is pathologically characterized by presence of amyloid deposition and neurofibrillary tangles, together with the loss of cortical neurons and synapses – it starts firstly in the entorhinal cortex and hippocampus, then to temporal lobe, parietal lobe and finally into parts of the frontal cortex and cingulate gyrus [4]. It must be noticed that cognitive

impairment of normal ageing – deficits in memory as an example, is concerned with reversible synaptic alteration, not neuron death [5].

Often AD goes unrecognized because it can be definitely diagnosed after patient's death, when the brain can be closely examined for certain microscopic changes caused by the disease. For diagnose of AD, are used patient's history, additional information of relatives, clinical observation with neuro - psychological tests as Mini-Mental State Examination (MMSE).

Since MMSE will provide normal results for a patient at early stages of AD, medical visualization techniques, as MRI, fMRI and PET, are employed additionally. Cognitive test results depend on comfort of patient with testing, his or her general health, used medication, fatigue and so on.

There are two underlying approaches for visualisation: in first case during SPECT and PET neuro imaging pharmaceutical compound as carbon-11, fluorine-8 are used for tracing of A-beta deposits beta - amyloid deposits. In other case we measure volume of human brain to estimate atrophy of human brain during progress of AD. Volume shrinkage of brain happens far earlier before symptoms of AD and MCI appear. This is less expensive and faster method, as well.

Since properties of human brains are different, it is crucial to use registration to a MRI brain image template. There are three main methods for registration: voxel - based morphometric techniques [7], ROI method and computational anatomy methods.

Current problem of estimation of brain shrinkage during AD is developed mainly in [8], and algorithms of semi-supervised learning are presented in [9, 10]. In [11] is presented another method for detection of AD by other popular semi-supervised learning method.

By modelling we aim to extract regions of brain which are most discriminative for presence of traces of mentioned diseases and to reduce preliminary information we need and calculation complexity of algorithms. Main purpose of current paper is to compare and estimate different methods of calculation of statistics of extracted features from selected regions. At last we apply clustering algorithms as ISO – Data.

In Part 2 the main algorithm is given, then in Part 3 – some experimental results and finally a conclusion is made.

2. Main algorithm

Here are presented stages of two algorithms: first one is for calculation of 3D mask that comprises parts of human brain where presence of degenerative tissues is most probable. The mask is created by applying a SVM classifier or KL divergence criteria for determination of most distinctive regions in two pre-processed and registered images of two patients - AD and healthy patients (Fig. 1). In second algorithm (Fig. 2) a mask is imposed on diagnosed patients with AD, MCI and healthy one and statistics of extracted features are computed.

The algorithms should manage with following obstacles: non-identical properties of human brain tissues in MRI images according to employed scanner, different size of human brain and due to age and sex of patients, varied degradation of brain tissues in different stages of development of AD, presence of different artefacts and image noises.

2.1. Pre-processing

In order to subdue already mentioned differences in degenerated tissue the pre-processing of neural images consists of following operations:

1) Reorientation of human brain – change orientation of human brain when subsequent operations demand it.

2) Resampling of image files - perform resampling of image data to decrease resolution of MRI image. Thus we reduce necessary memory and following operations requires objects with smaller size. On the contrary we perform upsampling in case of application of higher resolution mask.

3) Skull stripping – algorithms of removing of extracranial tissue from human brain image are semi-

automatical or automatical. Yet current software tools that execute this operation need human inspection to obtain accurate results.

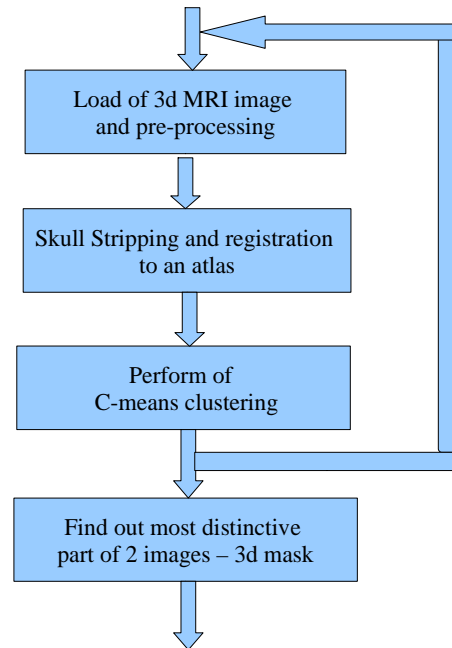


Fig. 1. 3D Mask construction by semi-supervised learning

4) Bias field correction – due to appeared artefacts, MRI images of human brain contain spatial variations. We apply bias correction in order to compensate them – it is implemented in software tools, as well.

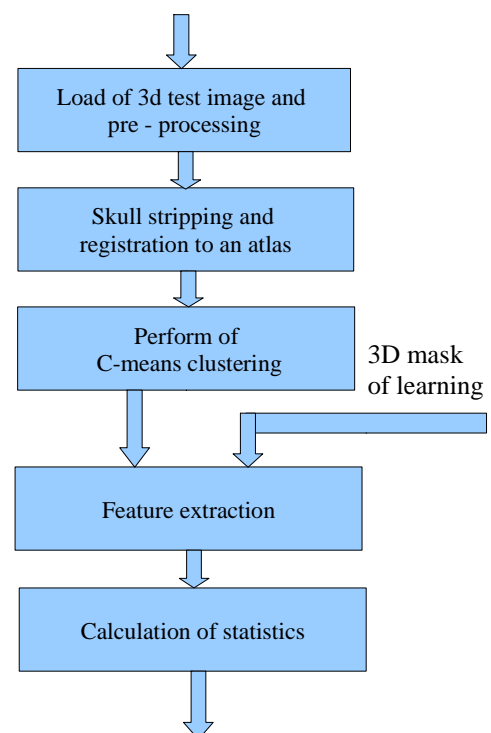


Fig. 2. Calculation of statistics from test image

5) Registration – image registration (warping) transforms image data to one coordinate system. In case of intra subject registration we register different images to a coordinate system of one image from image set and apply usually linear warping. In case of inter subject registration we use non-linear or linear registration to one coordinate system of external 3D model of human brain called atlas.

6) Reslicing – after registration we reslice pre-processed image. In this case transform matrix is applied to processed image, which is cut, analyzed and reconstructed with voxels whose size, volume and form is the same as template image.

7) Tissue segmentation – in order to extract basic anatomical entities in human brain, as white matter (WM), gray matter (GM) and cerebral spinal fluid (CSF) we apply C-means clustering method.

8) Reslicing – final operation is reslicing of preprocessed image. In this case transform matrix is applied to processed image, which is cut, analyzed and reconstructed with voxels whose size, volume and form are the same as template image.

After preprocessing of images we construct saturation map of segmented brain tissues in which different concentricity of intensity values account for healthy or non-degraded tissues.

2.2. Classifiers for construction of mask

In order to construct mask of most discriminating part of two groups of neuro images, we apply two methods: estimation with Kullback-Leibler (KL) divergence and probabilistic SVM.

In a certain point of distribution, KL divergence has the following value:

$$KL_{q,p}(u) = \int_{-\infty}^{+\infty} p(x) \log \frac{p(x)}{q(x)} dx, \quad (1)$$

where x is a descriptor of image in position u , $p(x)$ and $q(x)$ are probability distributions of measured quantities. In our case x is a measure of intensity values from a corresponding tissue from MRI image. So output of this operation is a gray-scale mask whose maximum values indicate regions with higher difference between two groups of neuro images.

We select SVM because of its good generalization properties with small training sample. In current algorithm it is the probabilistic version of SVM de-

scribed in [12]. The SVM training procedure consists of solving convex optimization problem. Let $\{x_i, y_i\}_{i=1 \dots N}$ is a set of training samples, where each sample $x \in \mathfrak{R}^d$ (d is the dimension of input space) is labelled with $y \in \{-1, 1\}$. If $K_{ij} = K(x_i, x_j)$ is the kernel matrix, where $K(x, y)$ is a Mercer kernel. Training SVM consists of determination the Lagrange multipliers α_i of the following optimization problem:

$$\min_{\alpha} \sum_{i=1}^M \sum_{j=1}^M \alpha_i \alpha_j y_i y_j K(x_i, x_j) - \sum_{i=1}^M \alpha_i, \quad (2)$$

$$s.t.: \sum_{i=1}^M \alpha_i y_i = 0, \quad C \geq \alpha_i \geq 0, \quad i = 1, \dots, M$$

where $C > 0$ is the upper bound determining the generalization properties of the SVM. For our classification task, we use the Gaussian kernel represented by:

$$K(x_i, x_j) = \exp\left(-\frac{(x_i - x_j)^2}{2\sigma^2}\right). \quad (3)$$

The class assignment for sample x with unknown class label, is given by:

$$y = \text{sgn}\left(\sum \alpha_i y_i K(x_i, x) + b\right). \quad (4)$$

2.3. Fuzzy C-means and ISO-data clustering

FCM is a clustering algorithm that performs fuzzy discrimination of input data through the following function for optimal discrimination:

$$J_{FCM}(P, U, \chi, c, m) = \sum_{i=1}^c \sum_{k=1}^N (u_{ik})^m \cdot d_{ik}^2(x_k, p_i) \quad (5)$$

on the condition that:

$$\sum_{i=1}^c u_{ik} = 1 \quad \text{for } \forall k \in \{1 \dots N\}, \quad (6)$$

where P and U are variables whose optimal values we seek, and: χ is the number of clusters of input data, $m \geq 1$ is the fuzzy degree, and u_{ik} describes the level of memberships of feature vector x_k to cluster, represented by $U = [u_{ik}]$ with $c \times N$ discriminating fuzzy matrix. The total number of feature vectors is N . While d_{ik}^2 is the distance between feature vector x_k and the prototype p_j . The matrix d_{ik}^2 is determined from:

$$d_{ik}^2(x_k, p_i) = |x_k - p_i|_A^2 = (x_k - p_i)^T \cdot A(x_k - p_i). \quad (7)$$

The matrix A can be every positive or negative matrix.

Let minimum of $J_{FCM}(P, U)$ be denoted with (P^*, U^*) and the necessary conditions for it are:

$$p_i = \frac{\sum u_{ik}^m x_k}{\sum u_{ik}^m}, \quad (8)$$

$$u_{ik} = \frac{1}{\sum \left(\frac{d_{jk}^2}{d_{ik}^2} \right)^{\frac{1}{m-1}}}. \quad (9)$$

ISODATA is a more complex algorithm, where the number of clusters is determined by repetitive calculations, division or merging of clusters, depending of standard deviations of samples from input data. Here the number of clusters, number of elements in separate clusters, thresholds for standard deviations of their elements and distances between elements are determined a priori. This algorithm is more flexible than standard k-means.

At the beginning is supposed presence of c fixed clusters in input data, their centroids are calculated, labels of separated samples are determined, and once again the centroids are calculated in order to decrease quadratic error of input data and current prototypes. Last two operations are repeated iteratively while the sum of distances between data points and prototypes is smaller than the selected threshold. Here minimization function is

$$J = \sum_{i=1}^c \left(\sum_{k, x_k \in S_i} d_{ik}^2 \right) = \sum_{i=1}^c \left(\sum_{k, x_k \in S_i} |x_k - p_i|^2 \right), \quad (10)$$

where S_i is a part of input data χ , corresponding to cluster i , d_{ik}^2 is the Euclidian distance metric between cluster prototypes and vectors of input data, belonging to them $x_k \in S_i$. With J is presented the total intra-cluster sum of quadratic error. Cluster prototypes are calculated in the following way:

$$p_i = \frac{\sum_{k=1}^N u_{ik} \cdot x_k}{\sum_{k=1}^N u_{ik}}, \quad (11)$$

where u_{ik} take 0 or 1 according to memberships of x_k in S_i .

In the case of k-means clustering we have fixed, unchanging prototypes.

3. Experimental results

In order to construct 3D mask of probable degenerative tissue of human brain, we select two distinctive images from diagnosed AD and healthy patients.

We perform skull stripping automatically by BrainSuite [13], registration of neuro images and statistical estimation of extracted features – intensity values by BrainImage Suite [14]. Neuro images are selected from ADNI – Alzheimer's Disease Neuroimaging Initiative. We calculate mean value and standard deviation of intensity values of voxels from three tissues – white tissue, gray tissue and CSF from applied mask on neuro images of AD, MCI and healthy patients (Table 1).

	Mean intensity value of voxels from segmented regions			Standart intensity deviation of voxels from segmented regions		
	CSF	GM	WM	CSF	GM	WM
1. Healthy patient	0.02	124.9	224.1	3	60	16.74
2. MCI patient	0.1	148.7	411.7	5.1	65.2	102.6
3. AD patient	0.05	87.5	217.8	2.7	40.7	53.5

Table 1. Statistical intensity estimation of voxels from segmented regions

4. Conclusion

We see that degeneration of brain tissue leads to change in intensity values of voxels in neuro images. In order to increase discrimination of healthy from degenerative tissues, we need to use more complex features or combination of features from preliminary selected regions of human brain.

5. Acknowledgment

This work is supported by Research and Development Sector (R&DS) with TU-Sofia under Grant No

102pd177-7 "Creation of models and object segmentation, applied to medicine and education".

References

- [1] L. Hebert, P. Scherr, J. Bienias, D. Bennett, and D. Evans. Alzheimer Disease in the US Population: Prevalence Estimates Using the 2000 Census. *Arch Neurol*, Vol. 60, 2003, pp. 1119–1122.
- [2] R. Petersen, Mild Cognitive Impairment. *Continuum Lifelong Learning, Neurology*, Vol. 13, 2007, pp. 13–36.
- [3] R. Terry, E. Masliah, D. Salmon, et al. Physical Basis of Cognitive Alterations in Alzheimer's Disease: Synapse Loss is the Major Correlate of Cognitive Impairment. *Ann Neurol.*, Vol. 30, 1991, pp. 572–580.
- [4] R. Petersen, Mild Cognitive Impairment as a Diagnostic Entity. *J Intern Med*, Vol. 256, 2004, pp. 183-194.
- [5] L. Apostolova, P. Thompson, A. Green, C. Jack, D. Harvey, R. Petersen, L. Thal, J. Cummings, C. DeCarli for the ADCS Group, 3D Analysis of Hippocampal Atrophy Progression in MCI subjects. In Proc. Of the 132nd Annual Meeting of the American Neurological Association, Featured in the "Dementia Walking Tour" ANA Session, Washington DC, October 2007.
- [6] P. Hof, J. Morrison. The Aging Brain: Morphomolecular Senescence of Cortical Circuits, *Trends Neurosci*, Vol. 27, 2004, pp. 607–613.
- [7] J. Ashburner, and K. Friston, Voxel-Based Morphometry — The Methods. *Neuroimage* Vol. 11, pp. 805–821.
- [8] R. Filipovych, S. Resnick, and C. Davatzikos, Semi-Supervised Cluster Analysis of Imaging Data, *Neuroimage*, Vol. 54, Iss. 3, 2011, pp. 2185-2197.
- [9] O. Chapelle, B. Schölkopf, and A. Zien, *Semi-Supervised Learning*. MIT Press, Cambridge, MA, 2006.
- [10] X. Zhu, Semi-Supervised Learning Literature Survey, University of Wisconsin–Madison, Tech. Rep. 1530, 2006.
- [11] R. Teramoto, Prediction of Alzheimer's Diagnosis using Semi-Supervised Distance Metric Learning with Label Propagation, *Computational Biology and Chemistry*, Vol. 32.6, Dec 2008, pp. 438-441.
- [12] J. Platt, Probabilistic Outputs for Support Vector Machines and Comparison to Regularized Likelihood Methods, In: A. Smola, P. Bartlett, B. Schölkopf, and D. Schuurmans (Eds.): "Advances in Large Margin Classifiers", Cambridge, MA, 2000.
- [13] X. Papademetris, M. Jackowski, N. Rajeevan, R. Constable, and L. Staib, BiImage Suite: An Integrated Medical Image Analysis Suite, Section of Bioimaging Sciences, Dept. of Diagnostic Radiology, Yale School of Medicine, <http://www.bioimagesuite.org>.
- [14] B. Dogdas, D. Shattuck, and R. Leahy, Segmentation of Skull and Scalp in 3D Human MRI Using Mathematical Morphology Human Brain Mapping, Vol. 26, No. 4, 2005, pp. 273-85.

ALGORITHM FOR COAXIAL PART'S DESIGN OF CABLE MULTIMEDIA NETWORK

Dobri Dobrev, Lidia Jordanova

*Faculty of Telecommunications, Technical University of Sofia,
8 Kl. Ohridski str., 1000 Sofia, Bulgaria
email: dobrev@tu-sofia.bg*

Abstract

In this paper a method for coaxial part's design of hybrid fiber-coaxial multimedia system is presented. The method is based on a study of noise and signal distortion introduced by the amplifiers that are connected in the coaxial line between the subscriber and the optical node. Dependencies are obtained for determining the acceptable output levels of the amplifiers, which take into account both the number of amplifiers and their parameters, and the actual channel loading. Formulas for calculating the required number of amplifiers, their gain coefficients and the distance between amplifiers are derived. An algorithm is presented to design the coaxial channel of hybrid network.

1. Introduction

Modern cable multimedia systems are of the hybrid fiber-coaxial (HFC) type. One of the main problems of these systems is the coaxial part of the cable distribution network. For compensation of the signal attenuation in the coaxial cable, radio frequency (RF) amplifiers are used, but they cause noise and distortion of the transmitted signals. Noise and distortion products accumulate along the coaxial line and worsen the quality of the received image and sound, and the errors in data transmission increase [1-3].

The quality worsening of the received signal in the coaxial part of a cable multimedia system can be estimated on the basis of parameters such as carrier-to-noise ratio (CNR) and carrier-to-interference ratio (CIR) measured at the drop amplifier output. Those parameters evaluate the portion of noise and distortions introduced by trunk amplifiers, feeders and drop amplifiers that are connected in the coaxial line between the subscriber and the optical node.

When designing a HFC multimedia system it is necessary to make advance planning of acceptable degradation of CNR and CIR parameters in coaxial and optical parts of the network. The aim is the

values of these parameters measured at the output of the subscriber outlet (SO) to satisfy the requirements: $CNR_{SO} \geq 49$ dB and $CIR \geq 54$ dB.

The tree-and-branch topology of the coaxial distribution network is the cause of the noise funnel effect in the reverse path channel. With such an effect the noise and inter-modulation products from all the cable network branches interfere with the signals from the subscriber's cable modems. As a result, the value of the bit error ratio (BER) at the receivers outputs of the headend is increased and the communications over the reverse path get worse or cut-off [4,5].

The main purpose of the paper is to develop an algorithm to design the coaxial channel of HFC multimedia system in order to ensure the given values of quality parameters.

2. Architecture of HFC multimedia network

HFC multimedia networks are usually realized on the hierarchical principle (Fig.1). The highest hierarchical level includes a primary optical ring which includes one primary and several secondary headends. The primary optical ring transports digital information using SDH or SONET standards. The second hierarchical level consists of secondary optical rings that are connected to the primary ring. Distribution hubs are connected to the secondary optical rings. Through optical lines the signals are transported from the hubs to the optical nodes that feed the coaxial network segments forming the lowest hierarchical level of the system.

Classical coaxial multimedia networks are implemented in the three-stage scheme. It consists of a trunk, distribution lines and a subscriber drop (home networks). Wide-band RF amplifiers are included along the coaxial lines because of the great losses inherent to coaxial cables. Since additional noise

and distortions are caused by each amplifier, a limitation of the number of amplifiers must be imposed, the coverage area of the coaxial network thus being reduced. Typically feeder lines are built short with no more than two amplifiers to provide a gain high enough to meet the needs.

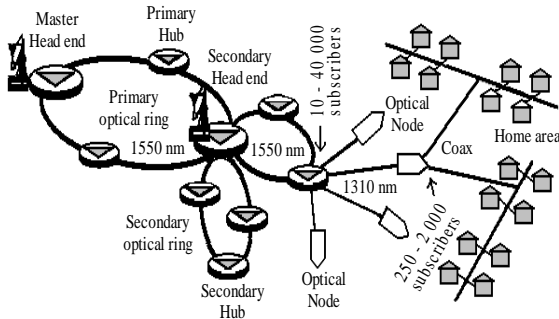


Fig. 1. HFC system topology

In [5] a mathematical model of the reverse path channel is suggested with the funnel effect being taken into consideration. If the carrier-to-noise ratio at the receiver input of the headend is known then the model makes it possible to optimize the topology of the coaxial distribution network and the number of the optical nodes whose signals are summarized in the receiver.

3. Limitations due to noise and distortions in the coaxial network

The quality worsening of the received signal in the coaxial part of a HFC system can be estimated on the basis of parameters such as CNR and CIR measured at the drop amplifier output. Those parameters evaluate the portion of noise and distortions (CSO and CTB) introduced by trunk amplifiers, feeders and drop amplifiers that are connected in the coaxial line between the subscriber and the optical node. The total CNR (in dB) can be expressed by

$$CNR_{\Sigma} = -10 \lg \sum_{i=1}^M 10^{\frac{-CNR_i}{10}}, \quad (1)$$

where CNR_i is the carrier-to-noise ratio at the output of the i -th amplifier in dB. For a cascade of M identical amplifiers, all operating with the same output level and tilt, CNR_{Σ} (in dB) can be easily calculated as follows

$$CNR_{\Sigma} = CNR - 10 \lg M \quad (2)$$

The CNR at the output of a single amplifier is given by the formula

$$CNR = U_{out} - K - 10 \lg(kTB) + 108.75 - NF = U_{out} - K - 1.54 - NF, \quad (3)$$

where U_{out} is the amplifier output level in dB μ V, K and NF are the gain and the noise figure of the amplifier in dB, respectively, k is the Boltzmann's constant ($1.38 \cdot 10^{-20}$, mW/Hz·K), T is the absolute temperature (290 K), B is the bandwidth (4.75 MHz) and $10 \lg(kTB) + 108.75 = 1.54$ dB μ V is the thermal noise in bandwidth 4.75 MHz.

From expressions (2) and (3) can be determined the acceptable minimum output level of the M -th amplifier (in dB μ V). It depends on the required carrier-to-noise ratio at the output of the coaxial channel CNR_{CCh} and can be defined as follows [3]:

$$U_{out \min} \geq CNR_{CCh} + K + 1.54 + NF + 10 \lg M \quad (4)$$

When M amplifiers are included in the coaxial line connecting the subscriber with the optical node, the following expression can be used to determine the value of parameter CIR (in dB):

$$CIR_{\Sigma} = -k_1 \lg \sum_{j=1}^M 10^{\frac{-CIR_j}{k_1}}, \quad (5)$$

where the coefficient k_1 depends on kind of distortion prevailing: $k_1 = 15$ with CSO and $k_1 = 20$ with CTB. As the influence of CTB is prevalent, for a cascade of M identical amplifiers can be written

$$CIR_{\Sigma} = CIR - 20 \lg M. \quad (6)$$

In the specifications issued by broadband equipment manufacturers CIR of the amplifiers is given for a reference output level $U_{out \text{ref}}$ (dB μ V) and channel loading N_{ref} (e.g. 36, 42 or 57 channels). When the amplifier output level and the number of channels differ from those given in the specifications, then the following correction of the amplifier performance must be made:

$$CIR = CIR_{\text{ref}} - k_2 (U_{out} - U_{out \text{ref}}) - 10 \lg(N/N_{\text{ref}}). \quad (7)$$

where U_{out} is the actual amplifier output level in dB μ V and N is the actual channel loading. If expression (7) refers to CSO, then $k_2 = 1$ and if (7) refers to CTB, then $k_2 = 2$. Thus it can be seen that all distortions are worsened when amplifier output level and channel loading raised.

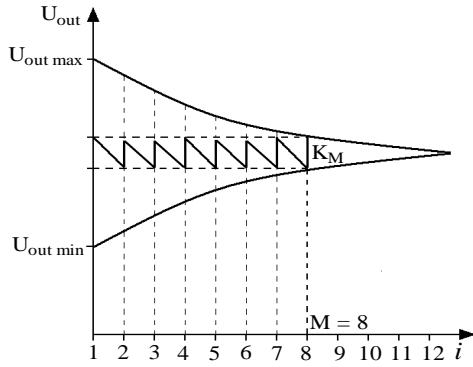


Fig. 2. Acceptable dynamic range of U_{out}

The maximum output level of the M -th amplifier $U_{out\ max}$ depends on the required carrier-to-interference ratio at the output of the subscriber outlet CIR_{SO} . Taking into account expressions (6) and (7) the following formula to determine $U_{out\ max}$ (in dB μ V) is obtained [3]:

$$U_{out\ max} \leq U_{out\ ref} - 10\lg(N/N_{ref}) - 20\lg M. \quad (8)$$

The values $U_{out\ min}$ and $U_{out\ max}$ come closer to each other and coincide for a given amplifier when the number N of the channels and M of the cascade amplifiers is increased (see Fig. 2). If the parameters of the wideband amplifiers and the attenuation in the coaxial cables on sale are taken into consideration it can be concluded that the coaxial trunk line can not be longer than 7 km and the number of amplifiers in the line can not exceed 10-15.

4. Determining the number of RF amplifiers and their gain

The acceptable level of the signal at the subscriber outlet U_{SO} is provided by adequate signal amplification in the coaxial and the optical transmission lines. The point of the unit gain concept is the transmission coefficient in the separate cable segment to be 0 dB. In other words, the amplifiers gain in this segment should compensate the total losses in it.

If this rule is used for the coaxial part of the network then the gain of the i -th RF amplifier in the cascade K_i (in dB) must be

$$K_i = (\alpha/100)l_{(i-1),i} \quad (9)$$

The quantity α is the cable attenuation in dB per 100 m given in the cable data sheets, $l_{(i-1),i}$ is the length of the coaxial cable between the $(i-1)$ -th and i -th amplifier in meters.

Dependencies (4) and (8) and the concept of unit gain can be used to determine the acceptable number of amplifiers in the coaxial lines and their gain. Let's assume that the RF amplifiers are of equal gain and there is an equal distance between them. Then the number M and the gain K_M (in dB) of the amplifiers can be determined by the equations

$$K_M = U_{out\ ref} - CNR_{CCh} - (NF + 1.54) - 10\lg(N/N_{ref}) - 30\lg M \quad (10)$$

$$K_M = \frac{L_{CL}}{(M-1)} = \frac{\alpha}{100} \cdot \frac{l_{CL}}{(M-1)} \quad (11)$$

where L_{CL} is the total cable loss (in dB) for a coaxial line with length l_{CL} (in meters).

5. Algorithm for coaxial channel design

When designing the coaxial part of a HFC multimedia system the following parameters must be given: the maximum length of the coaxial line l_{CL} , the channel loading N and the parameters of the selected cable (α) and amplifiers (NF , $U_{out\ max}$, CSO and CTB). The purpose is to determine the required number of amplifiers, their optimum gain and the distances between two adjacent amplifiers.

At first, it is necessary to calculate the total signal attenuation in the coaxial line

$$L_{CL} = (\alpha/100)l_{CL}. \quad (12)$$

The next step is to determine the distance S_i between the first and i -th RF amplifier so that the following condition to be met:

$$S_i = 100(i-1)K_i/\alpha \approx l_{CL}. \quad (13)$$

The gain of the i -th amplifier K_i is calculated using expression (10).

From the results obtained

$$i=2 \Rightarrow S_2 = 1 \cdot (100/\alpha) \cdot K_2$$

$$i=3 \Rightarrow S_3 = 2 \cdot (100/\alpha) \cdot K_3$$

$$\dots$$

$$i=M \Rightarrow S_M = (M-1) \cdot (100/\alpha) \cdot K_M \approx l_{CL}$$

it is obvious that condition (13) is satisfied for $i=M$. Therefore, the number of amplifiers that can be included in the coaxial line is M , and their gain is equal to that of the M -th amplifier.

To determine the distance between two adjacent amplifiers the following equation can be used:

$$l_{(i-1),i} = l_{CL} / (M - 1). \quad (14)$$

Finally, it is necessary to specify the admissible amplifiers output levels. They are given by the following formulas:

$$\begin{aligned} U_{\text{out max}} &= U_{\text{out ref}} - 20 \lg M \\ U_{\text{out min}} &= U_{\text{out max}} - K_M \end{aligned} \quad (15)$$

6. Conclusion

The algorithm here described make it possible easy design of the coaxial multimedia network to be performed when given the parameters of both the cable and amplifiers chosen and the HFC system (such as CNR and CIR at the subscriber outlet). The practical results show very good agreement between computed and measured values of network parameters (error less than 2 %).

7. Appendix and acknowledgments

The research described in this paper is supported by the Bulgarian National Science Fund under the contract No ДДВУ 02/74/2010.

References

- [1] D. Large, J. Farmer. *Broadband Cable Access Networks*, Elsevier, USA, 2009.
- [2] E. Bartlett. *Cable communications Technology*, McGraw-Hill, USA, 2005.
- [3] D. Dobrev, L. Jordanova. "Noise and distortion limitations in the design of HFC CATV systems", *Optical Fiber Technology*, Volume 12, Elsevier, USA, 2005, pp. 196-204.
- [4] W. Ciciora, J. Farmer, D. Large, M. Adams. *Modern Cable Television Technology*, Elsevier, USA, 2004.
- [5] L. Jordanova, D. Dobrev. "Improvement of the HFC System Reverse Path Performance", *Proceedings of the 14th ISC "Electronics"*, Volume 1, BG, 2005, pp. 156-151.

BROADCAST SIGNAL PROCESSING IN THE HEADEND OF A CABLE MULTIMEDIA SYSTEM

Lidia Jordanova, Dobri Dobrev, Tsveta Dimitrova

*Faculty of Telecommunications, Technical University of Sofia,
8 Kl. Ohridski str., 1000 Sofia, Bulgaria
email: dobrev@tu-sofia.bg*

Abstract

This article presents a block for processing of satellite and terrestrial television signals, received at the headend of hybrid fiber/coaxial (HFC) multimedia system. The architecture of the developed block and criteria for selection of its constituent modules (such as signal processors, digital receivers, remultiplexers, scramblers, DVB modulators, up-converters, etc.) are given. Appropriate schemes to implement some of the basic modules, building the block for broadcast signal processing, are suggested.

1. Introduction

The headend of a cable multimedia system is designed to receive the signals from satellite and terrestrial radio and television programs, to make processing of these signals for transmission to a cable distribution network and maintenance of an interactive communication with the users of additional services (Internet access, VoD, VoIP etc.). Processing of the received signals is necessary because of the different standards which are used in terrestrial (DVB-T/T2), satellite (DVB-S/S2) and cable (DVB-C/C2) broadcasting. Moreover, there are two systems for delivery of high-speed interactive services across cable networks (DOCSIS and DVB), which are incompatible. Therefore, there is a need to develop devices that can handle both standards. The application of such programmable and flexible devices in the headend and Set-Top-Box (STB) allows implementation of multiple standards on the same hardware platform [1-3].

Modern cable multimedia networks are always two-way, use optical fiber extensively, and are segmentable so as to allow simultaneous frequency reuse in various network sections. Two-way transmission of high-speed interactive services is performed by Cable Modem Terminal System (CMTS) that is located in the headend or in the hubs. Cable modem (CM) or STB is used in order to receive the data packets addressed to the subscriber and to transmit the data to the CMTS.

One of the main trends in the development of cable multimedia systems is to push as much as possible signal-processing equipment out to the hubs. This reduces the bandwidth requirement between headend and hub. For instance, if the VoD movies are stored at hubs and streamed from there to specific customers on demand, only the occasional content updates need be sent down from the headend to hub-based servers. Similarly, telephone host digital terminals (HDTs) at hubs can terminate calls from subscribers, and only the multiplexed DSx signals are transported over baseband optical links back to the headend where the switch is located. Such a solution allows furthermore reducing the possibility of outages affecting many subscribers simultaneously, and improving the quality of service [4-5].

The headend of a cable multimedia system can be divided into three fundamental modules. The first one is intended for processing of received broadcast signals, the second – for supporting interactive communication, and the third module provides network, services and subscribers management. The object of this paper is the architecture of the first module and the equipment needed for its building.

2. Modulation and Access Techniques for Down- and Upstream Channels

The systems here considered differ by using radio frequency (RF) carriers to transmit the information signals. Two frequency bands are provided for signal transmission from the headend to the subscribers: 112 MHz to 550 MHz (for analog video broadcasting) and 550 MHz to 862 MHz (for narrow casting services – data, voice and digital video). Analog video signals are transmitted by using VSB-AM while QAM methods (usually 256-QAM) are mainly used to transmit digital video programs and data. The system reverse paths make use of the 5 MHz to 65 MHz frequency band and subscribers' signals

are transmitted by using QPSK or 16-QAM methods.

For transmission of RF signals over the optic fiber are used optic carriers whose wavelength may be 1310 nm or 1550 nm while with DWDM the wavelengths can be chosen from the wave range recommended by ITU. The transmission can be based on either direct laser modulation or an external modulator. The parameters of the optical channels with direct laser modulation are of poor quality due to laser chirping, nonlinearity and slightly sloping transfer characteristic etc. To eliminate such a disadvantage a laser with a constant bias current and an external modulator at its output is used.

The Frequency Division Multiplexing (FDM) technique is the traditionally employed access method in CATV broadcasting networks. This technique, however, has limitations if it were to be used for the support of the new multi-rate, multi-service, multimedia services. Most appropriate for these cases is the combined FDMA/TDMA method in which the upstream bandwidth is divided to a few dozens of FDMA channels, each shared by a limited number of subscribers on a TDMA basis. Each subscriber will be assigned to a particular carrier and his traffic cells will be multiplexed into particular time slots in this carrier.

3. Block for broadcast signal processing

On Fig. 1 is shown the architecture of a module for processing of signals, received by the satellite or terrestrial antennas and those that are obtained from local sources, such as cameras, VCRs and DVDs. As is known, in satellite transmission are used predominantly QPSK signals, while in terrestrial television is still large share of analog TV programs that are transmitted via VSB-AM signals.

In order to transmit received AM-VSB signals over the cable distribution network they should be moved to another channel, which differs from broadcast channel. For this purpose analog signal processors (ASP) are used. The digital signal processors (DSP) convert the signals of digital television programs from RF to baseband MPEG Transport stream (TS). The same functions perform the satellite receivers which are often associated with decoders to descramble the satellite signals. Such descrambling digital satellite receivers are often termed as integrated receiver-decoder (IRD).

Cable operators often create their own local movie, sports or news channels. Since the output audio/video signals from the cameras or VCRs and DVDs are analog, these signals need to be converted into a digital. Conversion of the analog A/V signals to a MPEG TS is done by the MPEG encoder. The encoders are relatively expensive devices and can account for a large share of the total headend cost.

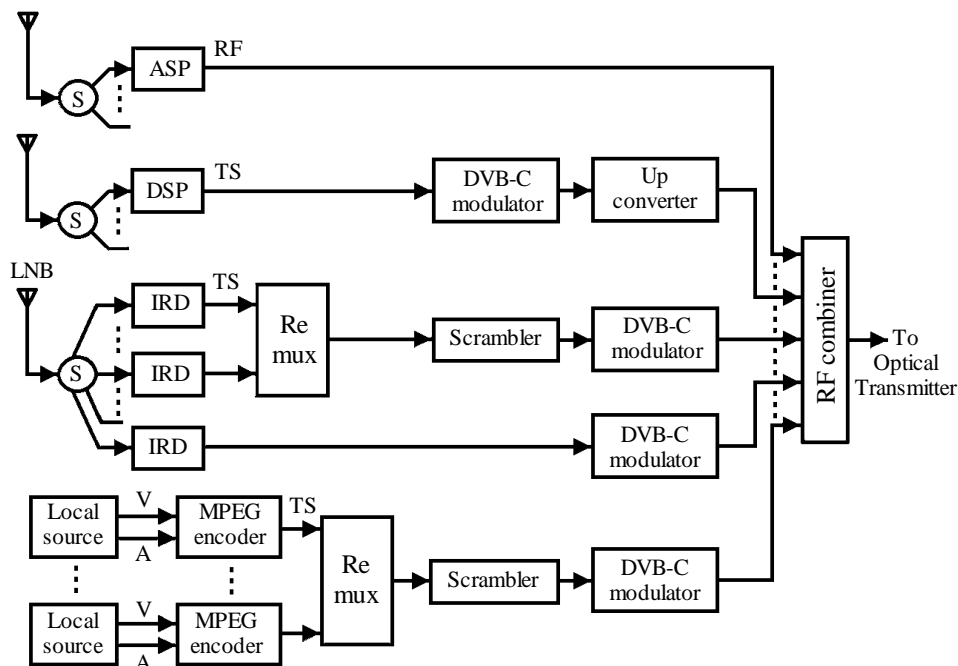


Fig. 1. Block for broadcast signal processing

The remultiplexers are used to form new transport streams that carry selected TV programs. Every remultiplexer has typically 8 or 16 ASI inputs, each of which is connected to its digital satellite receiver or MPEG encoder. It is very important to remultiplex the correct digital channels in each Transport stream. As is known, a news channel can be very efficiently compressed for transmission over a very small digital bandwidth. On the other hand a sports channel, which has a very high rate of a changing picture, cannot be compressed to the same extent as a news channel. Hence, efficient digital compression can be achieved if the remultiplexer creates its own re-bundle transport stream consisting of a mix of sports, news and movie channels.

Before submitting to the digital QAM modulators, the newly formed transport streams must be scrambled. This is done in order the signal to become unintelligible to those who are not authorized to receive it. After the QAM modulation the signal is fed to the upconverter which is frequency agile and the cable operator has the option of setting its output at any convenient frequency band in the cable TV spectrum. In many cases, the scrambler and up-converter are integral part of QAM modulators. Finally, the QAM signals are combined using conventional splitters. The output of RF combiner is the total set of broadcast signals, which are supplied to all subscribers.

4. Equipments required for developed block

This section deals with the electronic devices most commonly used in the headends to format broadcast signals for transmission on the cable plant. These devices include analog and digital signal processors, DVB-C modulators and up-convertors.

4.1. Signal processors

Signal processors are normally used to transfer incoming RF signals from off-air antennas or incoming cables to the cable plant.

Figure 2 illustrates a typical block diagram of analog signal processor. The incoming VSB-AM signal is supplied to a bandpass filter, BPF1, which is tuned to the incoming channel. In mixer M1, driven by local oscillator LO1, the received RF signal is down-converted to the intermediate frequency (IF or f_i), where $f_i = 38.9$ MHz – for the picture carrier and $f_i = 33.4$ MHz – for the sound carrier. The IF signal

is up-converted to the assigned output RF channel in mixer M2, driven by local oscillator LO2. Band-pass filter BPF3 eliminates the image of the second conversion process and any spurious signals coming from mixer M2.

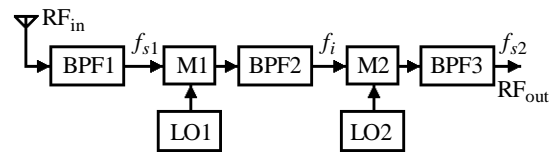


Fig. 2. Analog signal processor

On Fig. 3 a simplified diagram of the digital signal processor is shown. A digital signal is recovered off-air in DVB-tuner 1 and supplied to the PSIP processor and remultiplexer (remux). Processing of the received signal in the tuner includes: demodulation, analogue-to-digital conversion, filtering, error-protection decoding, removing the randomizing pattern. As a result, the MPEG transport stream (MPEG-TS) is obtained.

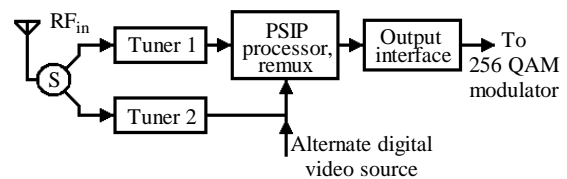


Fig. 3. Digital signal processor

As is known, digital video signals include the program and system information protocol (PSIP), a series of tables that tell the receiver what programs are included in the multiplex and how to find them. These tables must be modified if some programs are removed from the multiplex and others are added from another off-air channel or other source.

In the configuration shown, a second program stream may be added from either another off-air channel via DVB-tuner2 or from another signal source. This program transport stream is supplied to the PSIP processor and remux. Its PSIP tables are merged with those from the first program stream and multiplexed into a higher-bandwidth stream that is supplied to a 256-QAM modulator.

4.2. DVB-C modulator

Figure 4 shows a typical block diagram of DVB-C modulator. The modulator locks to the MPEG transport stream fed to it at the baseband interface and consisting of 188 byte-long packets. In order to en-

sure adequate binary transition, a randomization process has to be applied to the MPEG-TS. To produce an error-protected packet a shortened Reed-Solomon (RS) code is applied (Type 204,188) with the ability to correct eight random byte errors. The packets, which are then 204 bytes long, are supplied to the convolution interleaver to make the data stream more resistant to error bursts. It is based on the Forney convolutional approach with $L = 12$.

The error-protected data stream is then fed into the mapper where the QAM quadrant must be differentially coded, in contrast to DVB-S and DVB-T. Then the signal is roll-off filtered with a roll-off factor of $\alpha = 0.15$ and supplied to the QAM modulator.

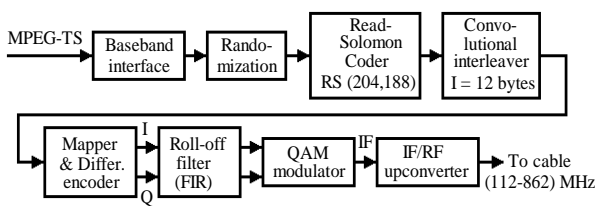


Fig. 4. DVB-C modulator

Since the modulation is performed on IF, the signal must be up-converted to the output channel. In some cases, the modulator includes the up-converter to the final channel assignment, in other cases, the up-converter will be external to the modulator.

One issue of concern is when scrambling is added in a digital transmission stream. In some headend systems, there is an external scrambler that adds scrambling prior to the modulator. In other headend systems, the scrambling is an integral part of the modulator.

4.3. Up-converter

If the output of the signal processor is frequency agile, meaning it can be set to any of a number of channels, the up-converter is replaced with a dual conversion output section, with a first IF above the maximum frequency the processor can output. Then the signal is filtered to remove the image, and down-converted to the output channel (Fig. 5).

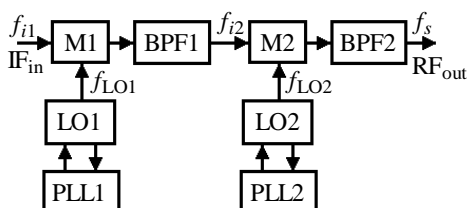


Fig. 5. Dual-conversion up-converter

The first local oscillator will up-convert the incoming IF signal ($f_{i1} = 38.9$ MHz) to some high frequency f_{i2} (f_{i2} must be higher than 862 MHz), i.e. the first local oscillator, LO1, operates at frequency $f_{LO1} = f_{i1} + f_{i2} = 38.9 + f_{i2}$ MHz. There may be some amplification at this second IF frequency before the signal is converted to the final output frequency in mixer M2, driven by local oscillator LO2. If the frequency for selected channel is f_s ($f_s = 112 \dots 862$ MHz) the frequency of LO2 will be $f_{LO2} = f_{i2} + f_s$.

The presented agile up-converter provides low spurious outputs. It is easy to establish that the image of both the first and the second conversion is well above any frequency we are interested in on the cable plant, and so far from the output frequency that it is easy to filter. This type of converters are best for setting the output of modulator (analog or digital) or CMTS on any frequency.

5. Conclusion

The block for broadcast signal processing presented in this paper ensures transmitting of both terrestrial and satellite radio and television signals through cable distribution networks. With its designing, the requirements of existing DVB standards are taken into account. The block was tested in order to determine the acceptable signal levels that ensure given parameters at the headend output.

6. Appendix and acknowledgments

The research described in this paper is supported by the Bulgarian National Science Fund under the contract No ДДВУ 02/74/2010.

References

- [1] D. Large, J. Farmer. *Broadband Cable Access Networks*, Elsevier, USA, 2009.
- [2] ETR 154, *Digital video broadcasting: Implementation guidelines for the use of MPEG-2 systems, video and audio in satellite, cable and terrestrial broadcasting applications*, EBU, Geneva, 1997.
- [3] ETS 300 429, *Digital broadcasting systems for television, audio and data services: Framing structure, channel coding and modulation for cable systems*, ETSI, 1995.
- [4] ECTE DV5111, *Digital broadcast delivery systems: Digital headend and distribution CFI response system description*, Scientific-Atlanta, Inc., 1997.
- [5] W. Ciciora, J. Farmer, D. Large, M. Adams. *Modern Cable Television Technology*, Elsevier, USA, 2004.

EDGE DETECTION IN SEQUENCES OF CT IMAGES

Veska M. Georgieva

Faculty of Telecommunications, Technical University of Sofia, Bulgaria
1000 Sofia, "Kl. Ohridsky" str.8
T. (+359 2) 965-3293; E-mail: vesg@tu-sofia.bg

Agata H. Manolova

Faculty of Telecommunications, Technical University of Sofia, Bulgaria
1000 Sofia, "Kl. Ohridsky" str.8
T. (+359 2) 965-2274; E-mail: amanolova@tu-sofia.bg

Abstract

In the paper is presented an approach for edge detection, which combines noise reduction with edge detection on a series of scales to achieve better results for shape and contours of different objects in sequences of CT images. So can be easier marked the differences in the inter sequence images in regard to observe better the changes in medical structures. To reduce the specific noise, the input CT image is decomposed on the base of wavelet packet transformation (WPT) by using of adaptive threshold of wavelet coefficients in the high frequency sub-bands of the shrinkage decomposition. Then the wavelet model is applied for Canny edge detector to develop a multiscale wavelet model for edge detection.

Implementations results are given to demonstrate the visual difference in 2 inter sequence images and some objective estimation parameters in the perspective of clinical diagnosis.

1. Introduction

Noise in CT is a multi-source problem and arises from the fundamentally statistical nature of photon production. This noise is not independent of the signal. It's Poisson distributed and independent of the measurement noise [1]. The measurement noise is additive Gaussian noise and usually negligible relative to the quantum noise. It comes from the motion of patient. The classical edge detectors work fine with high-quality images, but often are not good enough for noisy medical images. On the other hand approaches based on wavelet transform has been proposed separately for noise reduction and edge detection. Many existing methods for multiscale edge detection are based on DWT [2], [3].

In the paper is proposed to incorporate noise reduction and multiscale edge detection in CT images as a single process. To reduce the specific noise, the input CT images are decomposed on the base of WPT by using adaptive soft threshold on all high-

pass subbands of the shrinkage decomposition [4]. Then the wavelet model is applied for Canny edge detector to develop a multiscale wavelet model for edge detection [5]. On the base of the obtained edge maps of two consecutive CT images can be observe the specific difference in the shape and contours of medical objects.

2. Stages for CT images edge detection

In this paragraph are presented the basic stages of the algorithm, used to improve image edge detection and to demonstrate the difference by two consecutive CT images in the sequence, shown in Figure 1.

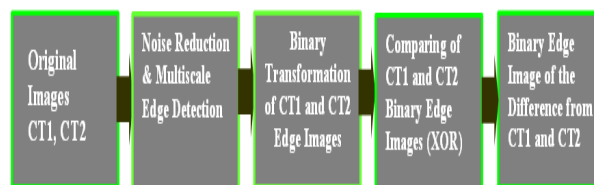


Figure 1. Block diagram of the algorithm

2.1. Noise reduction and multiscale edge detection

The first stage of the algorithm is noise reduction. It is based on the wavelet packet transform [4].

In an image contained Poisson noise can be presented as an additive noise model for each pixel is as follows (1):

$$s(x, y) = f(x, y) + n(x, y) \quad (1)$$

where $f(x, y)$ is the desired image, without noise, $n(x, y)$ is the noise.

The block diagram of this stage is presented in Figure 2.

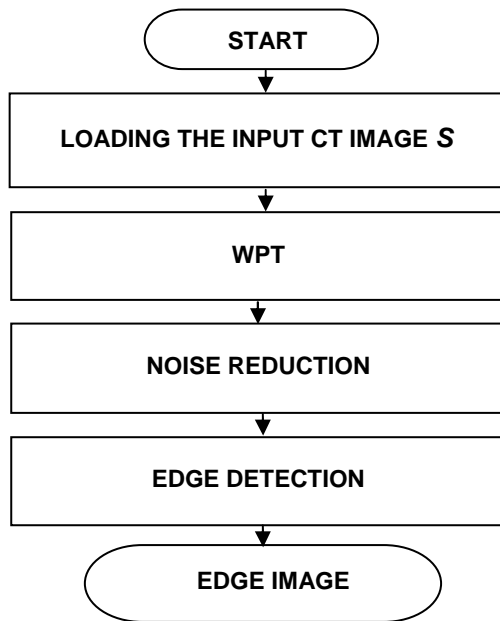


Figure 2. Block diagram of the stage for noise reduction and edge detection

The wavelet packet methods for noise reduction give a richer presentation of the image, based on functions with wavelet forms, which consist of 3 parameters: position, scale and frequency of the fluctuations around a given position. They propose numerous decompositions of the image, that allows estimate the noise reduction of different levels of its decomposition. For the given orthogonal wavelet functions exists library of bases, called wavelet packet bases. Each of these bases offers a particular way of coding images, preserving global energy, and reconstructing exact features. Based on the organization of the wavelet packet library, it is determined the decomposition issued from a given orthogonal wavelets. An optimal decomposition is used with respect to a conventional criterion. The criterion is a minimum of three different entropy criteria: the energy of the transformed in wavelet domain image, Shannon entropy and the logarithm of energy [6]. By determination of the global threshold it is used the strategy of Birge-Massart [7]. It uses spatial-adapted threshold, which allows to determine the thresholds in three directions: horizontal, vertical and diagonally. Choosing the threshold too high may lead to visible loss of image structures, but if the threshold is too low the effect of noise reduction may be insufficient. The procedure for noise reduction can be determined on the base of the calculated estimation parameters. PSNR and E_{FF} values are higher for better denoised CT image where the value of NRR is lower.

Wavelet filters of large scale are more effective for noise reduction, but at the same time increase the uncertainty of the location of edges. Canny edge detection method is optimal for step edges with application of additive noise model. From the point of wavelet transforms, it can be used more effective approach to adjust the scale of the filters. So the wavelet best shrinkage decomposition to noise reduction of the CT image can be used as wavelet model for Canny edge detection. The level of decomposition can be selected in depending on the requirement of details desired in the edges.

2.2. Binary transformation of CT edge images and comparing of their differences

To better compare the images we use the standard Otsu method [8] to transform the grayscale to a binary image and then find the difference between two consecutive images. The Otsu method for image binarization chooses an adaptive threshold to minimize the intraclass variance of the black and white pixels of the transformed image. Then in the output image we replace all pixels in the input image with luminance greater than **the threshold** with the value 1 (white) and replace all other pixels with the value 0 (black). Finally to compare the two images we perform an exclusive OR operation on the corresponding pixels of the two images. The resulting binary image's pixel is logical true (1) if **the first** image pixel or the second image pixel, but not both, are nonzero.

3. Experimental results

The formulated stages of processing are realized by computer simulation in MATLAB environment by using IMAGE PROCESSING TOOLBOX and WAVELET TOOLBOX. The image data consists of grayscale CT-slices images of the liver of size 512x512 pixels, 16 bits in DICOM format archived in 12 series. The simulation is made with additive Poisson noise with intensities values between 0 and 1 and corresponding to the number of photons divided by 10^{12} . The best results for the investigated sequence of CT images are obtained by the third, fourth and fifth level of the shrinkage decompositions. For noise reduction is used soft threshold. Errors as "missed detection" and "false alarm" in edge detection are minimized when the SNR of the detection filter is maximized. In the paper are analyzed some quantitative estimation parameters: Sig-

nal to noise ratio in the noised image (SNR_Y), Signal to noise ratio in the filtered image (SNR_F), Effectiveness of filtration (E_{FF}), PSNR and SSIM. In Table 1 are presented the obtained average results from simulation by using the proposed algorithm. They are compared with results obtained by using of classical Canny edge detector and multiscale edge detector based on discrete wavelet transformation (DWT). The best results are obtained by proposed approach including noise reduction on the base of WP transformation.

This comparison is very difficult through large variations of liver geometry between patients, the limited contrast between the liver and the surrounding organs and different amplitude of noise.

Table 1. Simulations results

Method of edge detection	Estimations Parameters				
	PSNR [dB]	SSIM	SNR_Y [dB]	SNR_F [dB]	E_{FF} [dB]
Canny edge detection (CED)	24.865	0.6	14.515	15.463	1.947
Noise reduction with DWT+CED	27.814	0.7	15.949	17.986	2.037
Noise reduction with WPT+CED	29.988	0.8	16.313	19.832	3.519

A visual presentation of the obtained results for the processed 2 consecutive images in sequence of 6 CT images can be seen in the next figures below.

In Figure 3 and Figure 4 are shown respectively the original and denoised CT1 and CT2 images. Figure 5 presents edge maps of the denoised CT1 and CT2 images. In Figure 6 are given respectively the obtained differences of original and denoised binary edge images.

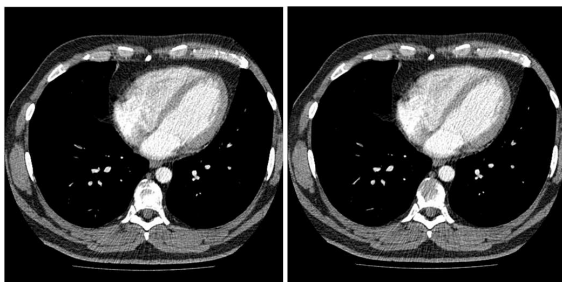


Figure 3. Original CT1 and CT2 images

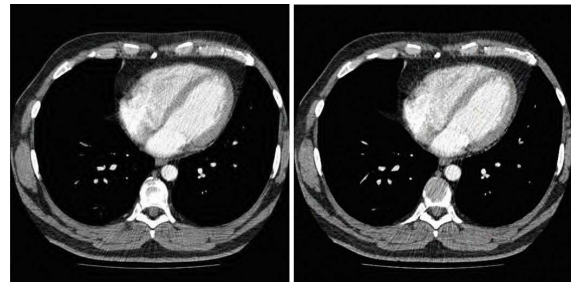


Figure 4. Denoised CT1 and CT2 images

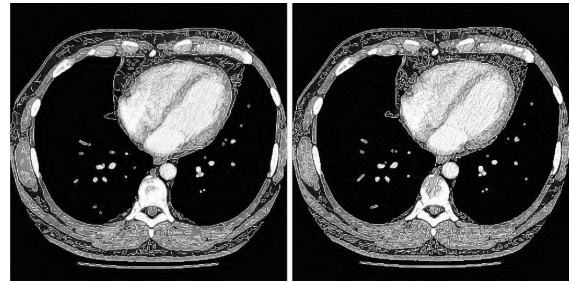


Figure 5. Edge maps of denoised CT1 and CT2 images

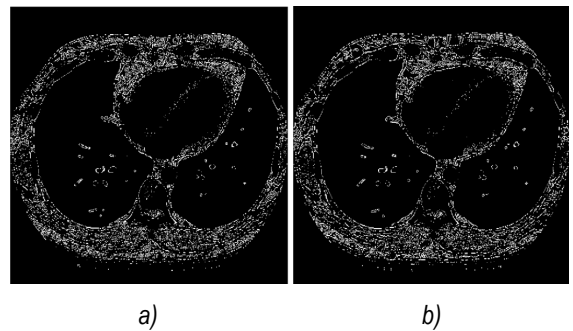


Figure 6. Binary edge images of the differences: a) of original CT1 and CT2; b) of denoised CT1 and CT2 images

4. Conclusion

The proposed wavelet based edge detection algorithm combines noise reduction with edge detection on a series of scales to achieve better results for shape and contours of different objects in sequences of CT images. The differences in the inter sequence images can be easier marked in regard to observe better the changes in medical structures. So the noise reduction process can't be applied by differences in the inter sequence images in the case of reiteration of elements in the same position for loss of specific medical information. The proposed approach can be used in clinical diagnosis or by modeling of anatomical organs and their visualization in 3D.

5. Acknowledgments

This paper was supported by the Joint Research Project Bulgaria-Romania (2010-2012): "Electronic Health Records for the Next Generation Medical Decision Support in Romanian and Bulgarian National Healthcare Systems", DNTS 02/19.

References

- [1] M. Smith, A. Docef, "Transforms in telemedicine applications", Kluwer Academic Publishers, 1999.
- [2] S. Mallat, S. Zhong, "Characterization of signals from multiscale edges", IEEE Trans. PAMI, 14 (7), pp.2207-2232, 1992.
- [3] S. Madchakham, P. Thitimajshima, P. Rakprathanporn, "Edge detection in speckled SAR images using wavelet decomposition", Proceedings of the 22nd Asian Conference on Remote Sensing, pp. 325-328, 2001.
- [4] V. Georgieva, R.Kountchev, I.Draganov, "An adaptive approach for noise reduction in sequences of CT images", MedDecSup 2011, accepted.
- [5] V. Georgieva, "Edge detection in ultrasound medical images using wavelet decomposition", Proceedings of the 5th CEMA'10, Athens, 2010, pp. 108-111.
- [6] R. Coifmann, M. Wickerhauser, "Entropy based Algorithms for best basis selection", IEEE Transaction on information theory, Vol.38, 1992, pp.713-718.
- [7] MATLAB User's Guide. Accessed at: www.mathwork.com
- [8] Otsu, N., "A Threshold Selection Method from Gray-Level Histograms," IEEE Transactions on Systems, Man, and Cybernetics, Vol. 9, No.1, 1979, pp.62-66.

APPLICATION OF MODIFIED FRACTAL SIGNATURE & REGNY SPECTRUM METHODS TO THE ANALYSIS OF BIOMEDICAL PREPARATIONS IMAGES

N. B. Ampilova

*Assoc. Prof. Comp. Sci. Dept, Math. & Mech. Faculty, St.Petersburg State University
Universitetsky pr. 28, Starii Peterhof, St.Petersburg 198504
ampilova@math.spbu.ru*

E. Y. Gurevich

*Sofia & Jacobs Foundation
Italyanskaya str. 10/5, St.Petersburg 191186
info@organicproduct.ru*

I. P. Soloviev

*Assoc. Prof. Comp. Sci. Dept, Math. & Mech. Faculty, St.Petersburg State University
Universitetsky pr. 28, Starii Peterhof, St.Petersburg 198504
soloviev@math.spbu.ru*

Abstract

The problem discussed in the paper is the essential part of the general research concerning the action mechanism of ultra-low doses (ULD) of medical preparations.

In this work we investigate a possibility to apply two fractal methods to analyze some classes of biomedical images. The first method — Modified Fractal Signature — was proposed in [6] for document analysis for automatic knowledge acquisition. The second method is based on the calculation of Regny spectrum for multifractal sets.

The investigation of applicability of described methods to 3 classes of preparations has been performed. Experimental results show that the method of modified fractal signature may be used for all given classes of images, whereas values of Regny spectrum for brain tumors do not allow us to classify them completely and an additional analysis has to be done. The important result of this work is that both methods are applicable to ULD-containing preparations.

1. Introduction

Traditional medicine as a rule uses simplified (linearized) models to describe the mechanism of a medical preparation effect on a living organism. At the same time the search of an adequate treatment methods requires to study the more complex, nonlinear and nonmonotonic reaction of an organism on the action of drug. To solve the problem we have to extend existing traditional methods by applying ULD of medical preparations. Investigations of ULD effects were performed by many scientists and now extensive experimental data are accumu-

lated. But the dynamics of processes concerning to ULD effect is rather complex and at the present time there is no any adequate mathematical model describing it. Nonetheless the research of such processes is performed by many methods, being an analysis of process images obtained in different points of time is a principal one. The methods widely used are texture, fractal, morphological analysis and neural network modeling as well.

A large body of research shows that self-organization property that is (according to [5]) “spontaneous beginnings of a structure, i.e. the appearance of an ordered state in an initial random distribution of the system components without apparent external action” is intrinsic to biological systems. We may consider images of such processes states as phase portraits of a complex dynamical system. Stable invariant sets (attractors) of self-organized systems often have complex geometrical structure — they are fractals or multifractals (unions of several fractal sets, being everyone has own fractal dimension). For such sets methods of calculation of fractal dimensions are used. Modified Fractal Signature method [6] is based on Minkovsky dimension that coincides with well-known box-counting dimension for non-empty bounded sets in \mathbb{R}^m . The basic idea of this approach is that a document is mapped onto a gray-level function. Furthermore, this function can be mapped onto a gray-level surface, and from the area of such a surface (called fractal signature) the

fractal dimension of the document image can be approximated.

Widely used approach is to calculate the special characteristic – multifractal (Regny) spectrum. Let $\{\mu_i\}$ be a probability measure defined on the set under investigation. The main idea of this approach is to use Regny entropy $S(q) = \frac{\ln \sum_i \mu_i^q}{1-q}$ which

depends on a parameter q and coincides with Gibbs-Shannon entropy $S = -\sum_{i=1}^W \mu_i \log \mu_i$ for $q = 1$ [1]. Unlike Shannon entropy, maximal value of Regny entropy corresponds to an ordered state of the system. Maximum principle, as applied to multifractal systems allows us to obtain a set of numbers (for different q) that are fractal dimensions of subsets in which Regny entropy is maximal. The spectrum is invariant with respect to brightness changing, rotation and scaling. Hence it may be used as some stable feature for a class of images. So, in [8] authors apply multifractal spectrum for texture analysis. It should be marked that there are several ways to calculate Regny spectrum ([3], [7], [8]). In this paper we follow the method developed in [7] that is based on the generation of coarsened partitions.

2. Main notions

Definition 1. Let F be a nonempty bounded set in R^n , $\Omega = \{\omega_l: l = 1, 2, 3, \dots\}$ — a covering F , $N_\delta(F)$ — the number of sets from Ω whose diameters are nongreater than δ . Let $dim_H F$ and $dim_T F$ denote Hausdorff and topological dimensions F respectively. F is said to be fractal if $dim_H F > dim_T F$. Box-counting (capacity) dimension is defined by $dim_B F = \lim_{\delta \rightarrow 0} \frac{\log_2 N_\delta(F)}{-\log_2 \delta}$.

Definition 2 [6]. δ -parallel body F_δ can be defined by $F_\delta = \{x \in R^n: |x - y| \leq \delta, y \in F\}$.

Definition 3. Let F be a nonempty and bounded set in R^n , F_δ — δ -parallel body F , $Vol^n(F_\delta)$ — n -dimensional volume of F_δ . For a constant s , if $\delta \rightarrow 0$, the limit of $Vol^n(F_\delta)/\delta^{n-s}$ is positive and

bounded, we say that F has Minkovsky dimension s , which is symbolized by $dim_M F$.

Theorem 1 [3] Let F be a nonempty bounded set in R^n . Then $dim_B F = dim_M F$.

3. Methods of analysis

3.1. Modified Fractal Signature Method

3.1.1. Method description

In [6] the authors call the method the Modified Fractal Signature approach since the direct computation of fractal dimension of a document image is not used, alternately the volume of a special thing — δ -parallel body — is estimated to approximate the fractal dimension.

Let $F = \{X_{ij}, i = 0, 1, \dots, K, j = 0, 1, \dots, L\}$ be an image with multigray level and X_{ij} be the gray level of the (i, j) th pixel. In a certain measure range, the gray-level surface of F can be viewed as a fractal. The surface area A_δ can be used to approximate its fractal dimension. In image processing the gray level function F is a nonempty bounded set in R^3 . The surface area may be calculated using the volume of a special δ -parallel body — blanket with the thickness 2δ . Denoting this volume $Vol^3(F_\delta)$

we have $A_\delta = Vol^3(F_\delta) / 2\delta$.

But according to the Definition 3 and Theorem 1 we can conclude that if

$$\lim_{\delta \rightarrow 0} Vol^3(F_\delta) / \delta^{3-D} = \beta > 0,$$

then $D = dim_M F = dim_B F$. Therefore, when δ is sufficiently small, we have $Vol^3(F_\delta) = \beta \delta^{3-D}$.

So, we have $A_\delta = \frac{Vol^3(F_\delta)}{2\delta} = \frac{\beta \delta^{3-D}}{2}$, from

which the fractal dimension D can be obtained. The value A_δ is said to be Fractal Signature. It should be noted that the essential distinction of images is their values of A_δ , hence in practice it is sufficient to calculate only fractal signatures.

According to Blanket Technique ([6]) the covering blanket is defined by its upper surface $u_\delta(i, j)$ and

its lower surface $b_\delta(i, j)$. Initially, $\delta=0$ and $u_0(i, j) = b_0(i, j) = X_{ij}$.

For $\delta=1, 2, \dots$ the blanket surfaces are defined iteratively as follows:

$$u_\delta(i, j) = \max \left\{ \begin{array}{l} u_{\delta-1}(i, j) + 1, \\ \max_{|(m,n)-(i,j)| \leq 1} u_{\delta-1}(m, n) \end{array} \right\}$$

$$b_\delta(i, j) = \min \left\{ \begin{array}{l} b_{\delta-1}(i, j) - 1, \\ \min_{|(m,n)-(i,j)| \leq 1} b_{\delta-1}(m, n) \end{array} \right\}$$

The volume of the blanket Vol_δ is computed from u_δ and b_δ :

$$Vol_\delta = \sum (u_\delta(i, j) - b_\delta(i, j)).$$

In practice, whole image F is divided into several non-overlapping subimages and A_δ is computed for every subimage. Then all A_δ are combined into the whole signature. Sometimes it is convenient to study a "map" of the image, where in every cell the corresponding fractal signature is written.

3.1.2. Numerical experiments

Fractal signatures were calculated for some kinds of connective tissues of animals. The picture shows one of images and the graphic illustrates the dependence of normalized fractal signature on the size of the partition box. Method demonstrates good separability of values for different classes of tissues.



Figure 1. Connective tissue: pharynx

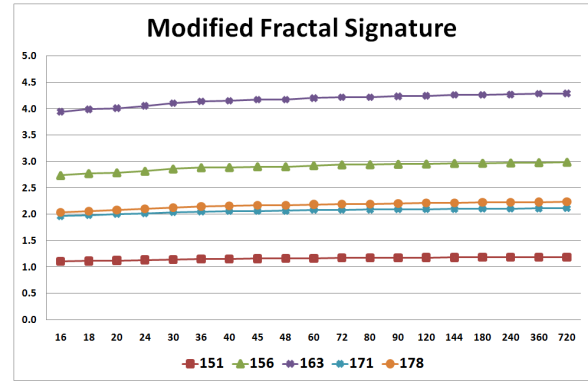


Figure 2. Fractal signatures for several types of connective tissue

3.2. Regny spectrum

3.2.1. Method description

Consider an irregular object embedded into Euclidean space and divide it into N boxes of sizes $l_i \leq l, i = 1, \dots, N$, where

$l < 1$ and the size of the whole object equals 1.

Let $\{\mu_i\}$ be a probability measure defined on the partition. Suppose that $\mu_i \sim l_i^\alpha$, where α is a scaling value that can take the values from some range with a probability density $\rho(\alpha)l^{-f(\alpha)}$, and so the probability to get α from an interval $(\alpha', \alpha' + d\alpha')$ is $d\alpha' \rho(\alpha')l^{-f(\alpha')}$, and a continuous function $f(\alpha')$ shows the fractal dimensions of the sets on which the singularities of strength α' may lie [4].

Now we consider the function $\chi(q) = \sum_{i=1}^N \mu_i^q$. It follows that $\chi(q) = \int d\alpha' \rho(\alpha') l^{-f(\alpha')} l^{q\alpha'}$.

When l is small enough $\chi(q)$ is maximal for $\alpha = \alpha(q)$ such that $q\alpha' - f(\alpha')$ is minimal (i.e. maximum of Regny entropy is achieved). It is known [3] that there is a unique finite nonzero function $\tau(q)$, such that

$$\chi(q) \sim l^{\tau(q)}, \tau(q) = \lim_{l \rightarrow 0} \frac{\ln \chi(q)}{\ln l}$$

and $\tau(q) = q\alpha - f(\alpha)$, $d\tau(q)/dq = \alpha$, i.e. $\tau(q)$ and $f(\alpha)$ are connected by Legendre transformation [3].

Regny spectrum $\{D_q\}$ is defined by the equation $\tau(q) = (q - 1)D_q$, where D_0, D_1, D_2 are Hausdorff, information and correlation dimensions respectively [2].

There are several methods to approximate D_q . We use the method of coarsening partitions developed in [7]. Consider K partitions of an image into boxes with sizes $r_k, k = 1, \dots, K$. Let μ_{ik} be a measure of the box i for k th partition. Let S_k be the number of the boxes in k th partition for which $\mu_{ik} > 0$. Then $\alpha(q)$ and $f(\alpha(q))$ may be calculated by the formulas:

$$\alpha(q) \approx \frac{A_k(q)}{\ln r_k}, \text{ where}$$

$$A_k(q) = \frac{\sum_i^{S_k} ((\mu_{ik})^q \cdot \ln(\mu_{ik}))}{\sum_i^{S_k} (\mu_{ik})^q},$$

$$f(\alpha(q)) \approx \frac{F_k(q)}{\ln r_k}, \text{ where}$$

$$F_k(q) = \frac{\sum_i^{S_k} \left((\mu_{ik})^q \cdot \ln \left(\frac{(\mu_{ik})^q}{\sum_i^{S_k} (\mu_{ik})^q} \right) \right)}{\sum_i^{S_k} (\mu_{ik})^q}.$$

For a fixed q values $A_k(q)$ and $F_k(q)$ are calculated for all K partitions. Hence in coordinate systems $(A_k(q), \ln r_k)$ and $(F_k(q), \ln r_k)$ there are K points that have to be approximated by a straight line. Using above formulas and least-squares method we obtain $\alpha(q), f(\alpha(q))$, then $\tau(q)$ and D_q .

3.2.2. Numerical experiments

Partitions into boxes are chosen depending on the size of the image. The box measure is defined as light level of the box concerning to the number of light pixels of the whole image.

For every image Regny spectrum was calculated for $q = 0, 1, 2, 3, 4, 5, 10, 20, 30, 40, 50$.

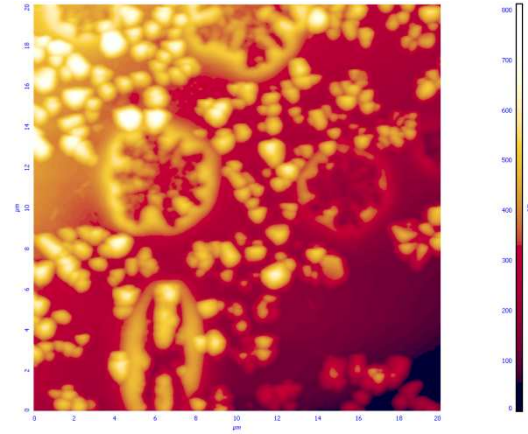


Figure 3. A compound with large dose of Ag

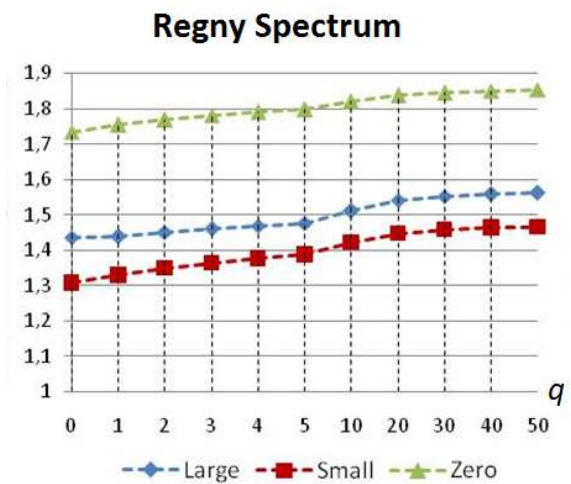


Figure 4. Regny spectrum for compounds with large, small and zero concentrations of Ag.

Conclusion

The results of numerical experiments performed for images of biomedical preparations of different classes shows that both methods are applicable to calculate special characteristic of images. They allow us to obtain numerical values that are invariant for some images transformations. We can classify images of ULD-containing preparations on accordance with the dose.

Both methods supplemented by texture and morphological analysis may be considered as a basis for image analysis.

References

- [1] Bak P. How nature works. The science of self-organized criticality. — Springer, Berlin, 1996.
- [2] Bashkirov A. G. Regny entropy as a statistical entropy for complex systems. *Theoretical and Math. Physics*, 149(2), 2006. (in Russian).
- [3] Falconer K. J. *Fractal Geometry. Mathematical Foundations and Applications*. — John Wiley & Sons, 1990.
- [4] Halsey T., Jensen M. Fractal measures and their singularities. — *Phys. Rev. A*, no. 33, 1986, pp. 1141-1151.
- [5] Rambidi N. *Structure and properties of nanoformations* Publ. House "Intellect", 2011. (in Russian).
- [6] Tang Y. Y., Hong Ma, Dihua Xi, Xiaogang Mao, C. Y. Suen. Modified Fractal Signature (MFS): A New Approach to Document Analysis for Automatic Knowledge Acquisition. — *IEEE Trans. Knowledge and Data Eng.*, vol.9. no. 5, 1997, pp. 742-762.
- [7] Vstovsky G. V. *Elements of information physics* — M.: MGIU, 2002.
- [8] Xu Y., Ji H., Fermüller C. Viewpoint Invariant Texture Description Using Fractal Analysis. — *International Journal of Computer Vision*, no. 83, 2009, pp. 85-100.

REAL TIME PROCESSING AND DATABASE OF MEDICAL THERMAL IMAGES

Alexander Bekiarski, Snejana Pleshkova-Bekiarska, Svetlin Antonov

*Technical University – Sofia, Bulgaria
Kliment Ohridski, 8
Tel.: +359 965 3300; E-mail: snegpl@tu-sofia.bg*

Abstract

Thermo vision systems are very popular in applications like military and police systems, systems for custom traffic control, industrial and medical systems etc. The information existent in thermal images of human bodies or human faces is very important because it can increase the right decision for final patient diagnostic and also can be used in thermo vision information system for customs control and combating terrorism. This information is usually presented as visualisation of thermal images in pseudo colours. From these images the diagnosis decision is made subjective usually after the doctor visual observation of the region of interest in thermal image. Therefore, the goal of this article is to develop real time algorithms in the medical thermal image systems for automatic medical thermal images processing and diagnostics. This will decrease or eliminate the subjective doctor errors in the diagnostic process. Also the proposed real time automatic processing algorithms will allow quick collection in the appropriate databases of the typical cases in diagnostic practices of frequently occurrence of the thermal images classes, which can be added and used in the global telemedicine information systems for diagnostics or used in thermo vision information system for customs control and combating terrorism.

1. Introduction

Medical thermal image systems consist mainly from thermal image sensors [1] or Thermo Camera (Fig. 1) for capturing thermal images of human body containing regions of interest for medical diagnostic.

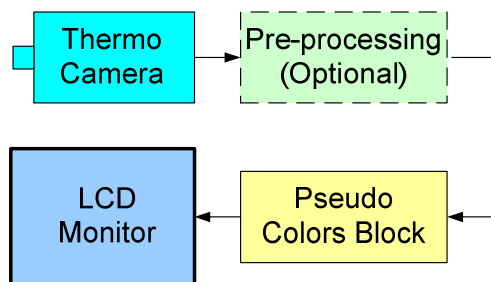


Fig. 1

The medical thermal or infrared medical images captured with Thermal Camera can pass optionally

through the Pre-processing Block for some simple and usual transformation and then through the Pseudo Colours Block for representation of each pixel temperature value as an appropriate and pre-defined pseudo colour for displaying on a standard video LCD monitor. The thermal images on the screen of the LCD video monitor usually are inspected and estimated from the doctors to decide whether or not the region of interest is connected with a disease (Fig. 2).



Fig. 2

To avoid subjective decisions or errors it is more convenient to apply automated methods and algorithms for thermal images processing to increase of contrast, resolution, general thermal images quality or to separate the regions of interest and finally to direct the doctors attention to the places of interest in thermal images. This is the goal of this article to propose the real time algorithms in the medical thermal image systems for automatic medical thermal images processing and diagnostics.

First it is necessary to outline the basic principles of human temperature representation in thermal images and the reasons of deviations from the ordinary values of a healthy person.

2. The basis principles of human temperature representation in thermal images

The human temperature in each moment can be described and is depending from many factors. There are the different ways a human loss or gain the heat from the environment. The body's core temperature remains constant on the condition that there is heat balance between the heat production and the heat loss [2]:

$$S = M \pm W \pm R \pm C \pm K - E - RES, \quad (1)$$

where:

S is heat storage;

M – metabolism influence value of human temperature;

W – external work influence value of human temperature;

R – heat exchange by radiation influence value of human temperature;

C – heat exchange by convection influence value of human temperature;

K – heat exchange by conduction influence value of human temperature;

E – heat loss by evaporation influence value of human temperature;

RES – heat exchange by respiration influence value of human temperature.

The above heat balance equation (1) is often used. However, when dealing with a person with clothing it is preferable to write the heat balance substituting $S = 0$ in equation (1):

$$M \pm W - E - RES = \pm K_{cl} = \pm R \pm C, \quad (2)$$

where:

K_{cl} is heat conduction through the clothing influence value of human temperature.

The equation (2) implies, that the metabolism (M) including the external work (W) minus the heat loss by evaporation (E) and respiration (RES) is equal to the heat loss conduction through the clothing (K_{cl}) and equal to the heat loss by radiation (R) and convection (C) from the other surface of the clothing. The sign indicates that the parameter may be negative or positive i.e. heat loss or heat gain. The equation (2) does not take into account the heat exchange by conduction, for example, when loading sacks or the contact between feet and

floor. This amount is normally insignificant influence on local heat exchange (warm fingers, cold toes). A person seated in an armchair, will exchange heat by conduction to the chair should be calculated as part of the clothing.

The influence of the metabolism M for the human temperature can be explained as energy released in the body by oxidation. This takes place at a rate which is equivalent to the amount of energy the body needs to function. The value of M may vary from a rest value of approximately $45W/m^2$ skin surface ($0,8\text{ met}$) to more than $500W/m^2$ ($\approx 9\text{ met}$) when running. The surface area of a normal person is approximately $1,8m^2$. The energy released is some times partly converted to external mechanical power W but is mainly converted into internal body heat. The metabolism is often given in the unit "met", where 1 met is equal to the metabolism for a seated, resting person ($1\text{ met} = 58,15W/m^2$).

The influence of the external work W can be either positive or negative, if a person cycles on an ergo meter with a heavy load, he must use a lot of energy to keep a constant velocity (r/min). This energy is split in two parts: W is the amount which is necessary to overcome the resistance from the load. In this case W is positive. The other part is the internal heat productions, which is necessary for the body to perform external work equal to W . This part of the energy is used to pump more blood around the increase the respiration. Man is however, a very poor machine. The efficiency is less than 20 % even for well-trained athletes. Thus if the load on the ergo meter is increased such that the corresponding W is increased by $10W/m^2$, then the metabolism will increased by $50W/m^2$. The extra $40W/m^2$ must then normally be lost by increased sweating to avoid increment of the internal temperature. If one walks down a steep hill and has to "brake" not to get too much speed, some of the potential energy will be transformed to heat in the muscles. The external work, W is in this case negative. The external work can be also lifting a tool, sack or case and they increase the potential energy for this object.

Heat Loss by Evaporation is partly from water vapour diffusion through the skin (E_d) and partly by evaporation of sweat on the skin surface the skin (E_{sw}). When evaporation takes place the water

uses heat from the skin. The amount of water diffusion through the skin and the corresponding evaporative heat loss (E_d) is a function of the difference between the saturated water vapour pressure at skin temperature (p_s) and the water vapour pressure in the ambient air (p_a):

$$E_d = 3,05 \cdot 10^{-3} (p_s - p_a), W/m^2, \quad (3)$$

where p_s and p_a are in Pa (Pascal).

The saturated water vapour pressure at the skin surface is a function of the skin temperature (t_s):

$$p_s = 256t_s - 3373, Pa. \quad (4)$$

Inserting (4) in (3) we obtain

$$E_d = 3,05 \cdot 10^{-3} (256t_s - 3373 - p_a), W/m^2 \quad (5)$$

Water diffusion through the skin will normally result in a heat loss equal to approximately $10 W/m^2$. A typical case is skin temperature $t_s = 33^\circ$ and a water vapour pressure $p_a = 1400 Pa$ in ambient air (50% relative humidity at $23^\circ C$ air temperature). This will result in a heat loss equal to $11,2 W/m^2$. The heat loss by water diffusion through the skin takes place all the time and is not controlled by the thermo-regulatory system.

Evaporation of sweat from the skin surface (E_{sw}) is one of the most effective ways by which the body can keep the internal temperature from increasing even during hard work. The amount of this evaporation may change a lot with activity (from $0 W/m^2$ at rest to maximum $400 W/m^2$ with very hard work) in a hot, dry environment. It is limited how much a person is sweat and there are great individual differences. Persons who are used to living and working in hot environments or performing hard work can improve the function of the sweat glands and obtain a better control of the body temperature. An acclimatised person is normally not able to sweat more than 1l per hour, and a total amount approximately 3,5l. If all this sweat is evaporated, it is equal to a heat loss of $675 W$ ($375 W/m^2$) and a total amount of $8505 kJ$. During hard work in hot environments it is important to drink water (plus salt) to be able to sweat enough. The estimation of the heat loss due to the evaporation of sweat is

rather complicated and not fully understood yet. By excessive sweating some of the produced sweat will drip and does not remove any heat from the body by evaporates at the skin surface that removes heat from the body.

3. The structure of the thermo vision system for thermal medical diagnostics and telemedicine

The detailed description and representation of the factors influencing the human bodies or faces temperature can be used in development of the structure of an automated thermo vision system with applying of real time processing algorithms for thermal diagnostics and application in telemedicine. The proposed structure is presented in Fig. 3.

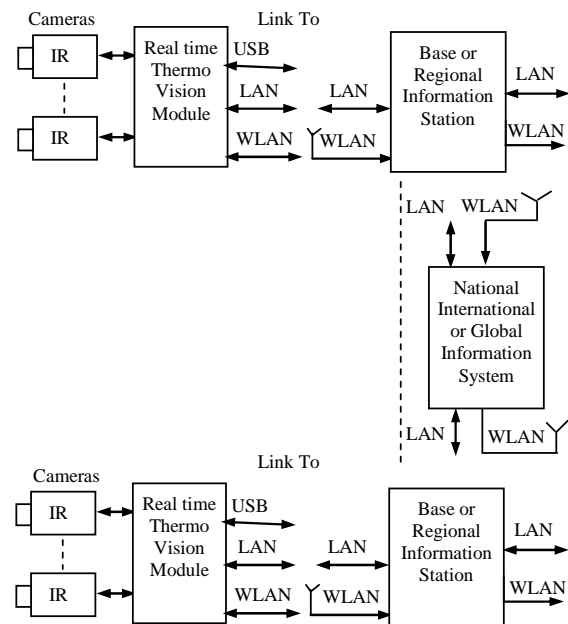


Fig. 3

The most important part of the proposed medical thermal vision system shown in Fig. 3 is the Real time Thermo Vision Module. The proposed internal structure of this module, in which are implemented the proposed and developed real time processing algorithms for thermal medical diagnostics, is shown on Fig. 4.

The main part of the infrared processing module is the embedded Digital Signal Processor (DSP), chosen to realize in real time most of the time consuming the developed medical infrared image processing algorithms. As a very popular possibility to extend the digital signal processor calculation capa-

bilities it is proposed and shown in Figure 1 a Field Programmable Gate Array (FPGA) [3], which can also take up some of the necessary and usually control and communication functions from digital signal processor to the telemedicine information systems.

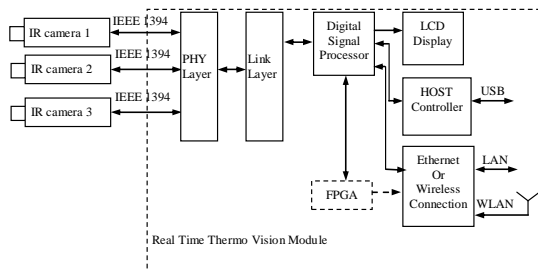


Fig. 4

The digital signal processor must have the possibility to drive a LCD Display for viewing input thermal images of human bodies or faces captured from each IR Camera or processed from digital signal processor medical thermal images. This can be done if digital signal processor is chosen from a set of special class signal processors known as Digital Media Processors [4]. These signals processors are also capable to interface with a specified host controller to the desktop or host computers. This guarantees the easy way to develop and test the algorithms for medical thermal images processing before their real time implementation in an embedded digital signal processor. Finally it is usually necessary to transmit the results from the medical thermal images processing or results from thermal diagnostics as important information for the medical telemedicine systems. The transmission can be accomplished by means of standard Local Area Networks (LAN) or Wireless Networks (WLAN).

The main advantages of the proposed internal structure of this module are:

- real time capturing of medial thermal images from standard thermo vision cameras;
- standard interfacing between digital signal processor and thermo vision camera in medical applications;
- visualization of input and processed medical thermal images;
- possibility to use desktop or host computer for development and testing application algorithms of automated thermal medical diagnostics using real time infrared image processing;

- collection of results of captured and processed medical thermal images and results from diagnostics in the in the appropriate databases of the typical cases in diagnostic practices of frequently occurrence of the thermal images classes;

- communication in wired or wireless LAN (Local Area Network) for transmission of results of captured and processed medical thermal images and results from diagnostics, which can be added and used in the global telemedicine information systems for diagnostics.

4. The algorithm of feature extraction using the proposed real time medical thermal images processing module in thermal medical diagnostics and telemedicine

To prove and demonstrate the real time processing abilities of thermo vision module it is proposed to apply and test this module in the applications of medical thermal images feature extraction. The testing is carried out with a Simulink model shown in Fig. 4. The extraction of features with real time medical thermal image processing is implemented in the block "General Real FIR" in Fig. 4.

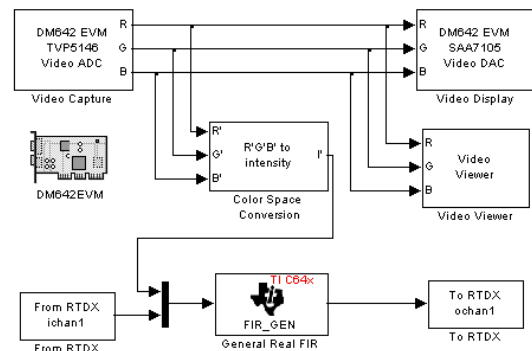


Fig. 4

This block is a part of embedded C64xDSP Library included in Matlab [5]. The main processing function of this block is to accomplish real time filtering of incoming data (in this case medical thermal image data) in the embedded digital signal processor module. The detailed representation of the block with name "General Real FIR" in Fig. 4 is presented in detail form on the Fig. 5.

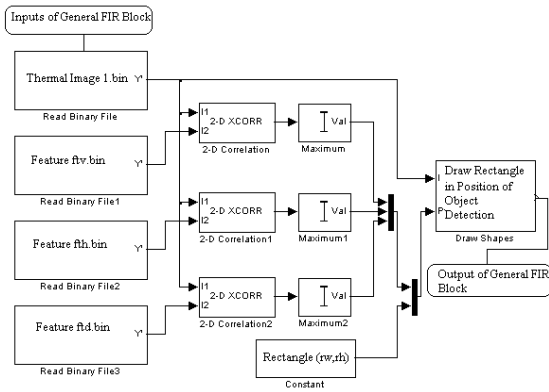


Fig. 5

The thermal image data are presented inside this block in form of binary image data format and are shown as first block “Read Binary File” in Fig. 5. In this article is proposed a modification of the algorithm for features extraction [6] in form medical thermal images. The features in form of rectangles are collected as templates and are also presented in Fig. 5 as “Read Binary File 1”, “Read Binary File 2” and “Read Binary File 3”, respectively for each of the chosen in [6] features: vertical (ftv.bin), horizontal (fth.bin) and diagonal (ftd.bin) in form of rectangles. In each of the “2-D Correlation” blocks is applied the following equation to calculate the two dimensional cross-correlation $C(i, j)$ between the matrix of the tested thermal image and each of the matrix of the features in form of rectangles “ftv”, “fth” and “ftv”:

$$C_k(i, j) = \sum_{m=0}^{N_y-1-N_x} \sum_{n=0}^{N_x-1-N_y} TI_m(m, n) \cdot FT_k(m+i, n+j) \quad (6)$$

for $0 \leq i < N_y + N_{f_k}^y - 1; 0 \leq j < N_x + N_{f_k}^x - 1; k = 1, 2, 3$,

where:

$N_x, N_y, N_{f_k}^x, N_{f_k}^y$ – horizontal and vertical dimensions of thermal image matrix TI_m and FT_k , respectively;

$k = 1, 2, 3$ – index of three features matrix FT_1, FT_2 and FT_3 for features “ftv”, “fth” and “ftd”, respectively.

From these three outputs of the blocks “2D Correlation” the values in matrices $C_k(i, j)$ are estimated in three Simulink blocks named “Maximum ...”, to calculate the maximal values ft_k^{\max} in each of three matrices $C_k(i, j), (k = 1, 2, 3)$:

$$ft_k^{\max} = \max[C_k(i, j)] \quad (7)$$

for $k = 1, 2, 3$.

The calculated in blocks “Maximum ...” maximal values ft_1^{\max}, ft_2^{\max} and ft_3^{\max} correspond to determination existence of features for vertical “ftv”, horizontal “fth” and diagonal “ftd” properties in tested “Thermal image 1”.

5. The experimental results and conclusion

The results of experimental test of extracted features in the some of the chosen medical thermal images are obtained with the proposed in the Fig. 4 blocks of Real time Thermo Vision Module. There are carried out tests with a collection in a specialized database of more than 600 medical test images of human bodies and faces. One of these test images is shown as an example in Fig. 6.



Fig. 6

The results of real time rectangle features extraction and regions of interest outlining are shown in Fig. 7 and Fig. 8, respectively, marked with the appropriate rectangles in the tested medical thermal image.

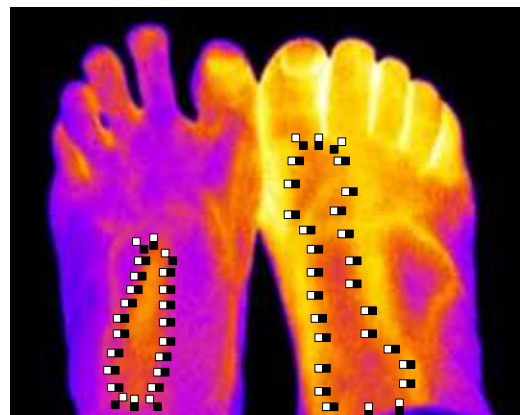


Fig. 7

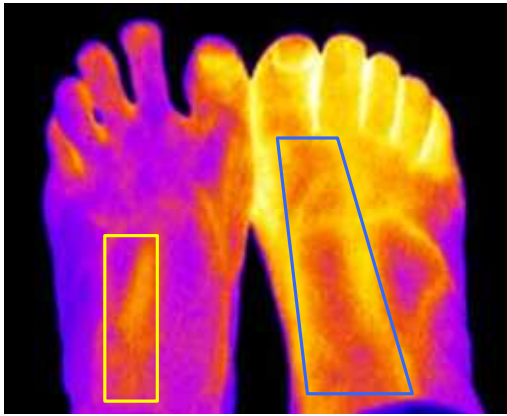


Fig. 8

6. Acknowledgments

This work was supported by National Ministry of Science and Education of Bulgaria under Contract DDVU 02/04/2011: "Thermo Vision Methods and Recourses in Information Systems for Customs Control and Combating Terrorism Aimed at Detecting and Tracking Objects and People".

References

- [1] Thermovision System (Infrared Thermal Imager/Camera for Medical Application), <http://www.made-in-china.com>
- [2] S. Uematsu, "Symmetry of skin temperature comparing one side of the body to the other", *Thermology*, vol. 1, pp. 4-7.
- [3] FPGA and CPLD Solutions from Xilinx. <http://www.xilinx.com>
- [4] Da Vinci Digital Media Processor. <http://www.ti.com>
<http://www.mathworks.com/products/matlab/>
- [5] Code Composer Users guide Texas Instruments. Literature number: SPRU296, February, 2009
- [6] Sn. Pleshkova, Al. Bekiarski. Algorithm of feature estimation for real time object detection in thermal images, The 4th International Congress on Image and Signal Processing, 15-17 October 2011, Donghua University, Shanghai, China (to be published).